An Investigation into the Manufacture and Mechanical Properties of an Al-Steel Hybrid MMC

A thesis submitted for the degree of Doctor of Philosophy

by

Rebecca A Davenport

BCAST

October 29, 2018

Abstract

One of the most significant challenges in the composite development field is to find a low-cost manufacturing route capable of producing large volumes of material. This thesis develops and characterises a potential avenue for addressing this, an induction furnace-based process.

This process produced a composite of A357 matrix and 10% wt Dramix 3D 80/30 SL steel fibres. The method was evaluated by microstructural analysis and optimum casting parameters were approximated.

The fibres were introduced to liquid A357 at 700°C and the composite was brought to a measured temperature of 650°C over not more than 120 seconds before being removed from the furnace and cooled. 10% wt was the ideal reinforcement ratio for this process.

Characterising the tensile and compressive strength of the composite material, it reached a peak stress 130% higher than A357 produced under the same conditions, though the peak stresses were still 20% of the literature values for T6 tempered A357. This suggests the need for development of a temper which does not degrade the properties of the composite. 3-point bending tests and some tensile specimens also showed post-failure strength.

Under dynamic loading, the composite showed a peak stress in excess of 100 MPa without reaching maximum compression under SHPB loading, and comparable performance to SiC-reinforced MMCs under ballistic testing.

The linear decrease in work-hardening with increasing distance from the impact site shows shock- and pressure-pulse dissipation properties, attributed to the difference in acoustic impedance between the matrix and the reinforcement.

Contents

List of Figures

List of Tables

Chapter 1

Introduction

The aims of this project were to produce and begin to characterise a hybrid metal matrix composite (HMMC). It was hoped that by using a process such as open-air or induction casting and commercially-produced steel fibres, a competitive material could be produced.

In the literature in the field of metal matrix composites (MMCs), a very current area of interest is in how to produce a composite with acceptable properties via an inexpensive and scalable manufacturing route. Chapter 2 deals with the state of the art in composite research and identifies promising areas of specific investigation for the project. This project has focused on methods for casting an HMMC and on the characterisation of the resulting product. Fewer casting methods were investigated in order to leave time for high-rate characterisation.

Composite manufacture via an induction furnace route is an area which merits significant further investigation and is an area of focus for this work. It is relatively easily scalable to industrial manufacture, and is not prohibitively expensive. Open-air gravity casting, which could have represented very substantial cost savings as a manufacturing route, was not found to be viable.

Chapter 3 lays out the manufacturing techniques attempted over the course of the project, including the selection of a suitable material for the matrix and a useful reinforcement fibre. The choice of matrix alloy was based on maximising fluidity and melting range, and so A357 was used. Of the commercially available fibres, the difference in performance between the Fibrex HT and the

Dramix 3D 80/30 fibres was not large, and so the more readily available Dramix 3D range was used in later work. The quality of the composites produced in a given test were assessed by sectioning and microstructural examination.

Characterisation of the composite material was principally carried out by quasi-static tensile and compressive tests, by dynamic compression using a Split-Hopkinson Pressure Bar (SHPB), by projectile impact testing with a gas gun, by microstructural examination, and by hardness testing.

Chapter 4 discusses tensile and compressive tests as well as 3-point bending tests and some imaging techniques. The compressive tests found a peak strength of 190 MPa and that while the presence of voids caused a deterioration in material strength, the quantity of voids did not have a very large effect. Tensile tests found that a fibre sitting approximately perpendicular to the loading axis would always nucleate failure at a very low stress, that fibres could provide some post-failure strength and confirmed that gravity-cast samples could not produce a useful composite material.

Chapter 5 covers the two high-strain-rate characterisation tests (the Split Hopkinson Pressure Bar and the gas gun). The SHPB demonstrated that the shear deformation which is characteristic of dynamic loading was accessible at relatively low strain rates and that the material showed strength even after deforming. It seems likely that the material was not tested to failure during these tests, and that stronger impacts or smaller specimens would be needed to achieve this.

In gas gun tests, the HMMC and a SiC-based MMC were penetrated by a projectile impact to similar distances for a giver firing pressure and both showed evidence of localising the damage caused by the shockwave. Microstructural examination and hardness testing confirmed that the material behaved in a manner consistent with the formation and relatively rapid dissipation of a shock.

In general, microstructural examination and hardness testing found that the composite had a relatively large grain size because rapid cooling was not possible, though smaller than that found in very slow-cooled aluminium alloys due to the crystal nucleation sites provided by the fibres.

In Chapter 6, it is concluded that the new manufacturing route, using an induction furnace, is a very promising avenue for further development., such as a refinement of the optimum reinforcement

fraction. In this work, a composite material was produced which was found to have good resistance to shock damage as described in Chapter 5 and measurable post-failure strength.

Chapter 2

Context and Background

2.1 Introduction

This chapter will present the current state of the art in composite design and manufacture, looking primarily at hybrid metal matrix composites (HMMCs). It will also discuss some of the theoretical background which underpins later work and motivates the choice of project goals, specifically to produce and characterise a composite material of high ballistic resistance.

Commposites, and metal matrix composites in particular, have been shown to have a specific strength as high as 244 kNm/kg and a specific stiffnes of 40MNm/kg [1] [2]. It is, in general, possible to mitigate a particular undesirable property, such as brittleness, at the cost of increased complexity and expense to manufacture and some other properties which are hopefully less critical to the desired application [3].

Metal matrix composites are usually divided into composites with a metallic matrix and ceramic reinforcement (referred to in this document as MMCs) and composites with a metallic matrix and metallic reinforcement (often referred to by their composition, eg “Al-steel composite” and referred to here as hybrid MMCs or HMMCs). “HMMCs” has also been used to describe a metallic matrix and both metallic and ceramic reinforcement.

This work is focused on HMMCs rather than MMCs because despite their highly desirable properties, MMCs are difficult to manufacture [4], expensive to machine [5] and very brittle [1]. Less work has been done on HMMCs, and it is hoped that a satisfactory product can be made with less difficulty.

MMCs are much more commonly used than HMMCs [6] [7] [8], meaning that the properties of MMCs are often used as a "benchmark" for HMMCs. Below, in Table 2.1 are some examples of MMC and HMMC properties, taken from a datasheet provided by Materion Corp. [1] and [6]. This is expanded on in Section 2.5.

It can be seen from these tables that the properties of the composite are in some cases substantially better than the Al matrix and in others worse. For example, the ductility becomes very poor, even at low volume fractions [1]. The properties of the composite are comparatively insensitive to the SiC bulk properties, as might be expected [6].

However, consistency between specimens is lower than for monolithic materials, which makes conclusions less reliable and poses challenges for experimental design [3].

MMCs have a high damage resilience: they will retain structural properties when compressed [9] and metal-reinforced ceramics have demonstrated a retention of strength after crack formation in tension [10]. This is a highly desirable property, and it is hoped that HMMCs will display this without the prohibitive manufacturing cost.

Composite properties show a strong dependence on temperature [6] and at least some dependence upon strain rate [11], showing higher flow stress at higher strain rate as might be expected [12] [11]. Strain rate sensitivity appears to be primarily based on the strain rate sensitivity of the matrix rather than the fibre reinforcement [13].

A composite will fail when both the matrix and the reinforcement have yielded. In practise, the reinforcement will disrupt both crack formation and plastic flow [6]. Details of the failure behaviour are discussed in Section 2.6 and Section 2.8.

The uptake and use of MMCs is limited by their lack of ductility [9]. It had been hoped that metallic fibre would mitigate this limitation.

When particulate- and fibre-reinforced MMC are compared, the fibre-reinforced composites shows substantially better wear resistance [5] [14] [15]. Reinforcement of 20% vol for fibre has almost the same wear resistance as 40% vol particle-reinforced composite. This is discussed in Section 2.5.

2.2 Metal Matrix Composites

"MMC" is used to mean a composite with metallic matrix, typically a light metal such as Al or Mg, with a ceramic reinforcement. There are three broad types: particulate-reinforced, rod-reinforced and continuously reinforced, shown in Figure 2.1 [3].

Continuously reinforced composites are the strongest but the least isotropic [3], with nearly all the reinforcement strength along the fibre direction (i.e. parallel to the fibres for tensile and compressive loading but perpendicular for shear or torsion loading). These are also the most expensive to manufacture, as the metal must be cast into the aligned fibres.

Rod-reinforced composites are much less expensive to manufacture than continuously reinforced composites, and are more isotropic but have a lower peak strength [3]. They must be manufactured either by stirring in the ceramic rods or by forcing the matrix material to infiltrate a preform.

Whiskers are defined as reinforcement rods with an extremely large aspect ratio. The whiskers themselves are very strong, but very expensive to manufacture, difficult to infiltrate past the surface tension of aluminium and are generally better in compression than in tension [3].

Particulate-reinforced composites are the most versatile in terms of machining and manufacture, as well as the most mechanically isotropic [3] [2]. They can be manufactured by in-situ reaction of the metal matrix as well as by direct mixing or hot isostatic pressing (HIP) citeDelannay1987 [17], depending on the relative desirability of net-shape manufacture and regular reinforcement particle size. They can be close to isotropic [3].

The manufacturing methods for these metallic composites are similar to those used in polymer- and resin-based composites [3] and to ceramic-metal based composites such as those for reinforced concrete. Some, such as Fibrestone (manufactured by Fibrestone Products Ltd), have some

	AA 2124	SiC	Composite Al/SiC	Pure Al	Steel	Composite Pure Al/steel
Density (g/cm^3)	2.78	3	2.88	2.71	7.00	–
Thermal Conductivity (W/mK)	152	30		234	–	–
Elastic Modulus (GPa)	73	—	115	69	200	–
0.2% Proof Stress (MPa)	440	304.7	440	24	–	45
$\%$ Elongation at Fracture	8%	—	4%	18 %	–	6.5%
Ultimate Tensile Strength (MPa)	485	304.7	610	39	–	72
Poisson's Ratio	0.33	0.13	0.3	0.34	–	–
Vickers Hardness	146	—	210 HV5	19	–	34
Fracture Strength (10^{-6} cycles)	125 MPa	4.28 MPa	375 MPa	50 MPa	–	–

Table 2.1: *Examples of the changes caused by the introduction of reinforcement to an Al matrix. AA2124 properties from the ASM Handbook [16]; SiC from azom.com, MMC composite from Materion datasheet, pure Al and HMMC composite from Mandal et al [7] or the ASM Handbook. The composite typically has properties between those of the matrix and of the reinforcement, but in the case of the UTS of the MMC it is higher than either.*

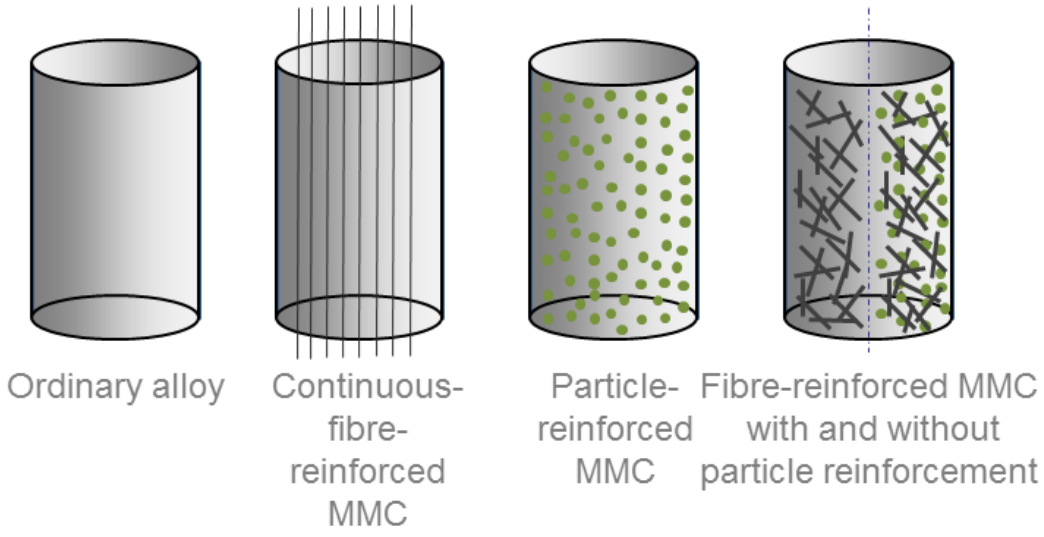

Figure 2.1: *Diagrammatic representation of three of the main types of composite: continuous fibre reinforced, particle reinforced and fibre- or rod-reinforced. Each type has its own advantages and disadvantages, for example continuous fibre-reinforced composites are typically strongest but the least mechanically isotropic [3].*

applicability to HMMC research [6], as described in Section 2.4.2. Their damage models and characterisation tests are useful in this context.

More current research is discussed in Section 2.8 and Section 2.4.

2.3 Benefits of the Hybrid MMC

HMMCs are expected to be more ductile than MMCs for a given reinforcement fraction, and to be easier and less expensive to manufacture, based on the very low ductility of MMCs and the Rule of Mixtures [1] [8].

The manufacture of MMCs has been a significant challenge in their development, partially because of the high surface tension of aluminium and its alloys [18] and because of the strong tendency of micro- or nanometre-scale particles to agglomerate.

Methods to overcome these problems include sustained mixing in the semi-solid state, with or without additional magnetic stirring [19] [20], hot or cold isostatic pressing of powdered Al and powdered reinforcement [21] and in-situ reactions [17]. All of these methods are difficult to adapt to commercial-scale production, and this has helped to limit the uptake of these very useful materials.

HMMCs can be manufactured from commercial Al ingots and commercial steel reinforcement materials, as supplied to the concrete industry. The very high demand for concrete reinforcement has reduced the cost to €1800 per tonne (as quoted to the author during this project by N.V. Bekaert S.A.), which is very competitive against SiC which is available from Goodfellow [22] for €294 for 500 g. Prices are reproduced as they were quoted, since price per unit mass is often dependent on order size.

In addition to its higher raw material costs, SiC powder is very hazardous to human health [23] both because of its small particle size and because of the risk of causing silicosis, a build-up of scar tissue in the lungs which damages lung function [24]. Steel fibres on the order of tenths of

a millimetre in diameter and tens of millimetres in length do not present these hazards, reducing both the cost and risk of manufacture.

Therefore, if an HMMC with acceptable properties can be manufactured in a scalable and cost-effective manner, it will be substantially less expensive alternative material when compared with MMCs. This has been the driving theme of this thesis.

The expected improvements in ductility arise from the fact that in a ceramic-reinforced composite, there is no scope for the ceramic to yield, which limits the total ductility of the material [25]. Doell et al found an inverse correlation with reinforcement particle size and elongation at failure, with a similar inverse correlation with UTS.

Steel reinforcement, in contrast, while less ductile than most Al alloys [26] is nevertheless expected to produce a more ductile composite than ceramic. It has also been shown that steel fibres reinforcing a ceramic matrix can provide significant strength after matrix fracture [6].

While the substantial increases in ductility that had been hoped for were not seen, the induction furnace manufacturing method discussed in Section 3.3, if scaled to industrial levels, is expected to be a safer and comparatively low-cost method of producing a material with promising ballistic resistance.

2.4 Composition and Manufacture of MMCs

Recent research into MMCs can be divided broadly into studies of the properties of novel composite compositions, producing better predictive models of composite behaviour, and developing new manufacture routes.

2.4.1 Materials Used for the Matrix or Reinforcement

Nanometer-Scale Reinforcement

If an MMC is reinforced with nanometre-scale particles (as opposed to the more common millimetre- or micrometrescale particles) a very high tensile strength can be [27]. This is in part due to the very high strength of bulk materials with nanometre-scale crystalline structure. However, these nano-crystalline materials were found by Zhang et al to have substantially lower toughness and ductility than micro-crystalline materials.

Creating a composite with a combination of micrometer-scale and nanometer-scale reinforcement has been shown [27] to be promising in terms of increasing strength and hardness, by impeding dislocation flow and increasing dislocation density. However, by doing so to a smaller extent than nanocrystalline grains, the strength is achieved without sacrificing ductility and toughness. Nanometer-scale crystals are also very expensive (100-1000 μm SiC costs €317 for 500 g [22]), and are very difficult to infiltrate past the surface tension of the matrix.

An attempt has been made [28] to produce a metal matrix composite reinforced with single-walled carbon nanotubes. The nanotubes were coated in Ni and dispersed among powdered Ti alloy, then heat-sintered and cooled in an induction furnace to prevent TiC formation. Microscopy confirmed that the nanotubes survived the manufacturing process, and characterisation tests found that the grain size had been reduced to 30% of the matrix alloy, suggesting improved strength, and the Vickers hardness value had increased to 288% of that in the matrix alloy.

Dasari et al [29] used graphene oxide as a reinforcement material in 99.9% pure Al using cold compaction and sintering. The microhardness was found to increase by 29% was observed with 0.2 %wt of reinforcement. Indentation to failure suggested that in some cases significant ductility was seen.

Other Reinforcement Materials

Jose et al [30] used lemon grass ash as a composite reinforcement material as a cost reduction measure, as this is a waste product from some power stations. Lemon grass was collected, dried and burned before being preheated to 250°C and introduced to semi-solid Al6061 at 610°C. Electrical stirring was then performed for 10 minutes in a procedure similar to that sed by Yang [19]. The composite was then re-melted and cast into an ingot.

Microstructural analysis showed strong bonding had occurred above 710°C, hardness measurements showed 155 HV, compared with 51 HV in matrix material similarly prepared. Tensile tests showed that the composite strength was 120% of the unreinforced matrix.

Matrix Materials Used

Both aluminium and magnesium have been explored as a matrix for HMMCs. Tungsten [31] and steel are the most used reinforcement materials, tungsten for its high hardness and strength and steel for its low cost and high availability.

When researching Mg/Fe MMCs [18], steel was found to be superior to carbon as a reinforcement material, producing a composite with superior rigidity and temperature stability. Heat treatments were found to improve the strength compared to as-cast samples.

Coating and Etching of Fibres

Composite strength was also improved by increasing the bond thickness between fibre and matrix. This was effected by either a Zn coating on ferritic fibres, which produced a 15 μm intermetallic phase, or by acid treatment of stainless steel fibres which produced a comparable interface and a good distribution of precipitates through the matrix.

Impact testing suggested that a composite made with as-received steel is weaker than the matrix alloy, tested as a reference. Using Zn-coated steel gave a composite significantly stronger than the

matrix alloy, and etched stainless steel fibres could withstand approximately twice as much impact pressure. The Zn coating improved wettability of the fibre surface and improved the interface formation. Stainless steel fibres etched for 20 minutes showed an approximate 400% increase in impact resistance versus the unreinforced alloy [18], thought to be because the etched wires have a much higher frictional resistance to pulling out and possibly to enhanced interfacial bonding. It was additionally observed that the bi-metallic surface was highly vulnerable to corrosion.

A copper coating has also been used [32] [33] to improve the bonding between matrix and interface. The squeeze casting method used by Chelladurai et al produced micro-voids at the surface of the uncoated steel mesh.

2.4.2 Manufacturing Processes

Infiltration with Agitation

Some work [13] suggests that vibration or ultrasonic agitation of the mould will promote wetting (and, to a limited extent, dispersion) of the fibres. It will also aid the escape of any trapped gases in the preform. [10]

In cases where the reinforcement is not made using a rigid preform, agglomeration of fibres or particulate additives can be prevented using ultrasound irradiation [13].

Composites with small ($> 100\mu$m) particulate reinforcement have been manufactured by high shear mixing in the semi-solid state [19]. This method has permitted reinforcement fractions in excess of 5 %wt to be successfully introduced, although the technique can introduce significant porosity into the ingot without degassing.

Stir casting [33] has been used to create an Al/steel fibre composite with up to 10 %wt reinforcement at a casting temperature of 738°C and a stirrer speed of 350-800 rpm. A specialist stir casting machine was used for this process. A micrograph of the composite produced is shown in Figure 2.6, showing the $> 100\mu$m voids present in the material.

Pressurized Infiltration

Squeeze casting is carried out by injecting superheated liquid metal into a mould and compressing it with around 100 MPa [34] [35] [32]. The mould cools the injected metal very quickly and typically produces a very fine grain structure.

Squeeze casting yields good infiltration and wetting as well as moderately tuneable infiltration parameters [18] [35] [36] [37]. Different sources of pressure used include gas pressure infiltration [18], high [36] or low [37] pressure and squeeze casting [35].

Thermodynamic calculations suggest that the pressurisation creates undercooling if applied near the eutectic temperature because the applied pressure increases properties such as melting and liquidus temperatures [34], and in Al-Si alloys shifts the eutectic point to the left, giving a higher Si content in solid solution as the undercooling prevents precipitation.

Large pieces of steel placed in the crucible did not form an appreciable intermetallic layer [35], suggesting that a larger fibre radius will produce a thinner interface. Using 12 μm diameter fibres gave an intermetallic layer thickness of approximately 10 μm, decreasing with casting temperature and contact time between fibres and liquid matrix. Defining the "solidification dwell time" as the time spent at elevated temperatures while the composite was entirely solidified, this did not have an appreciable impact on the interface thickness. Injecting the melt at several places simultaneously led to more isotropic behaviour in the final product. Hufenbach et al [18] use gas pressure infiltration for Mg/Fe composites. Kenningley et al [36] use high-pressure infiltration of Al/Si into sintered Fe/Cr/Si preforms. Low pressure infiltration can achieve good results in a Mg/ceramic system [37].

The manufacture of Mg/Fe HMMCs was carried out using pressurized infiltration of a fibre preform. It was a challenge because of the comparatively poor wettability of steel [2] [18]. Both Zn and Mn were trialled as trace additives to reduce the surface tension. The addition of between 0.2% and 0.9% zinc increased both the strength of the composite and its susceptibility to hot cracking. Using manganese as a replacement for zinc in the alloy improves strain at fracture, hardness

and corrosion resistance without increasing the hot cracking susceptibility compared with the basic magnesium-aluminium alloy. The aluminium concentration was limited to less than 10% to prevent large-scale formation of brittle Al-Mg intermetallic compounds.

Kenningley et al [36] used a steel-Al HMMC manufactured by squeeze casting to study its behaviour under heated fatigue loading. The squeeze casting process infiltrated molten Al-Si alloy at 750°C into a preform which had been heated to 300°C to produce a composite with 15% vol reinforcement. The die, which was cooled to maintain a temperature cooler than 200°C, was used to punch-press ("squeeze") the melt-preform mixture at 100 MPa for 3 min. It was found that visco-plastic flow was preferred in a direction transverse to the fibres and that under an applied stress, a higher strain would develop transverse to the fibres than parallel to them even without plastic flow.

Boland et al [38] produced composites by squeeze-casting into a sintered fibre mat reinforced with a random planar network. The compositions investigated were pure Al (LM0) matrix with 601 Inconel reinforcement, an Al-Si casting alloy (AS16) matrix with Inconel reinforcement, and AS13 with 316L stainless steel reinforcement. Both the Inconel and the stainless steel fibres were 12 m in diameter, and the authors did not find a clear temperature threshold for fibre dissolution into the matrix. The LM0 melt was heated to 850°C and the AS13 to 700°C to maximise its fluidity, the die and punch were used at room temperature and 350 g of liquid metal was introduced for each casting. Shrinkage voids were found at the die walls. When using AS13, the preform was wrapped in alumina felt to prevent temperature gradients appearing. When attempting to force infiltration of a preform with more than 35% vol reinforcement, the preform had to be heated until it was above the melting temperature of the matrix alloy.

With gas pressure infiltration [18], stainless steel wires are initially either zinc coated or etched with sulphuric acid for 20 minutes and then rinsed in acetone. The desired temperature and pressure can be produced in a laboratory autoclave. High pressures are essential for this method. Composites prepared in this way were able to absorb 21.1% strain before failure, as opposed to 3.48% in the parent alloy AZ91, with a density increased from 1.82 g/cm^3 to 2.99 g/cm^3.

Low pressure infiltration [37] used 0.25 MPa, exerted by argon gas, on a preform composed of SiC

fibres and commercial purity Al particles. The fibre density was 10% by volume. The preform and solid Al were induction heated in a tube, and when the melting temperature of the matrix alloy had been reached the gas pressure was applied. The authors found good isotropy and no change in thermal expansion behaviour when compared to traditional squeeze-casting methods.

HMMCs can be manufactured by squeeze-casting Al into a stainless steel preform. A pressure of 20 MPa [35] gives good infiltration. Casting at a higher temperature creates a more even inter-metallic layer of the same thickness, weakly suggesting that the layer thickness is more dependent on pressure than temperature.

With squeeze casting [35], casting at 950°C into a 250°C die and applying 20 MPa pressure yielded a central interface thickness of 6 μm. Casting at 20 MPa and 750°C into a room temperature die the, central interface thickness was 5 μm but varied between 0.5 μm and 10 μm across the height of the die. A good sample was also produced squeeze casting at 100 MPa, with the melt heated to 750°C, the die and punch to 300°C, and the preform to 300°C [36]. Colin et al found that ensuring an even solidification dwell time, improved by an even temperature or increased solidification temperature range in the casting alloy, gave a much smaller variation in interface thickness.

High-pressure diffusion bonding was also used to join commercial purity Al and stainless steel [39]. Using 70 MPa pressure, 15% reinforcement by volume, a temperature of 600°C and pressing times varying between 15 minutes and 32 hours. After 15 minutes, the interface thickness was approximately 25 μm. This suggests that 15 minutes is more than sufficient under these conditions, a statement supported by Bhagat [40], who used a hot isostatic press and found that in Al/stainless steel composites, the tensile strength was highest at 30% volume fraction, 800 K, 140 MPa and 1 minute.

Vacuum infiltration in general [41] is less expensive than other production methods, and does not promote interface formation, possibly because it is done at comparatively low temperatures. Pai et al [41] found that for stainless steel AISI 304 in pure Al, 450°C exposure for 100 hours was necessary before destructive intermetallic formation occurred. With nichrome fibres (80% Ni, 20% Cr), 350°C exposure was sufficient, and this temperature dropped further when using an Al-Mg matrix, but this suggests that vacuum infiltration is a promising technique.

Hot and Cold Isostatic Pressing

A hot isostatic press has been used to produce a HMMC of high strength and excellent infiltration [40] [6], as seen in Figure 2.2.

Plotting HIP temperature or pressure against maximum tensile strength produced an n-shaped curve with a clear optimum point for each HIP parameter. The measured strength of the composite seems to increase linearly with volume fraction and increasing the HIP time gives decreasing strength up to 30 min, after which little change is seen [40].

Using the data from Figure 2.3, it is possible to estimate the conditions which will produce a composite with optimum tensile properties. Increasing the pressure or heating time is detrimental, but time and temperature degrade the properties more rapidly. This is likely due to the relative growth rates of the fibre interface, though it is possible that the effects on the matrix microstructure are more significant. The maximum strength obtained in this case was in excess of that estimated by the rule of mixtures, probably due to the effects of the reinforcement on the deformation behaviour in the matrix.

A pure Al-W composite was produced by CIP at 345 MPa and sometimes by HIPing at 100 MPa and 450 degrees [42]. Tweaking the particle size in the input can produce a tailored microstructure.

Rolled Multi-Layered Composites

A multi-layered 1050 Al/IF steel composite was produced [43] by rolling a stack of sheets of steel and aluminium at 400°C to 50% height reduction, cut, re-rolled, partially annealed and rolled a final time. At 400°C the bonding seen was diffusion-driven rather than reaction-driven. After hot rolling the sheets were water-cooled to prevent further diffusion.

The resulting composite showed a very fine-grained structure, as would be expected of a rolled metallic material, in the Al, steel and interfacial layers. The layer chemistry showed an increasing concentration of Al with decreasing distance to the Al layer. the material is expected to be very anisotropic in its properties.

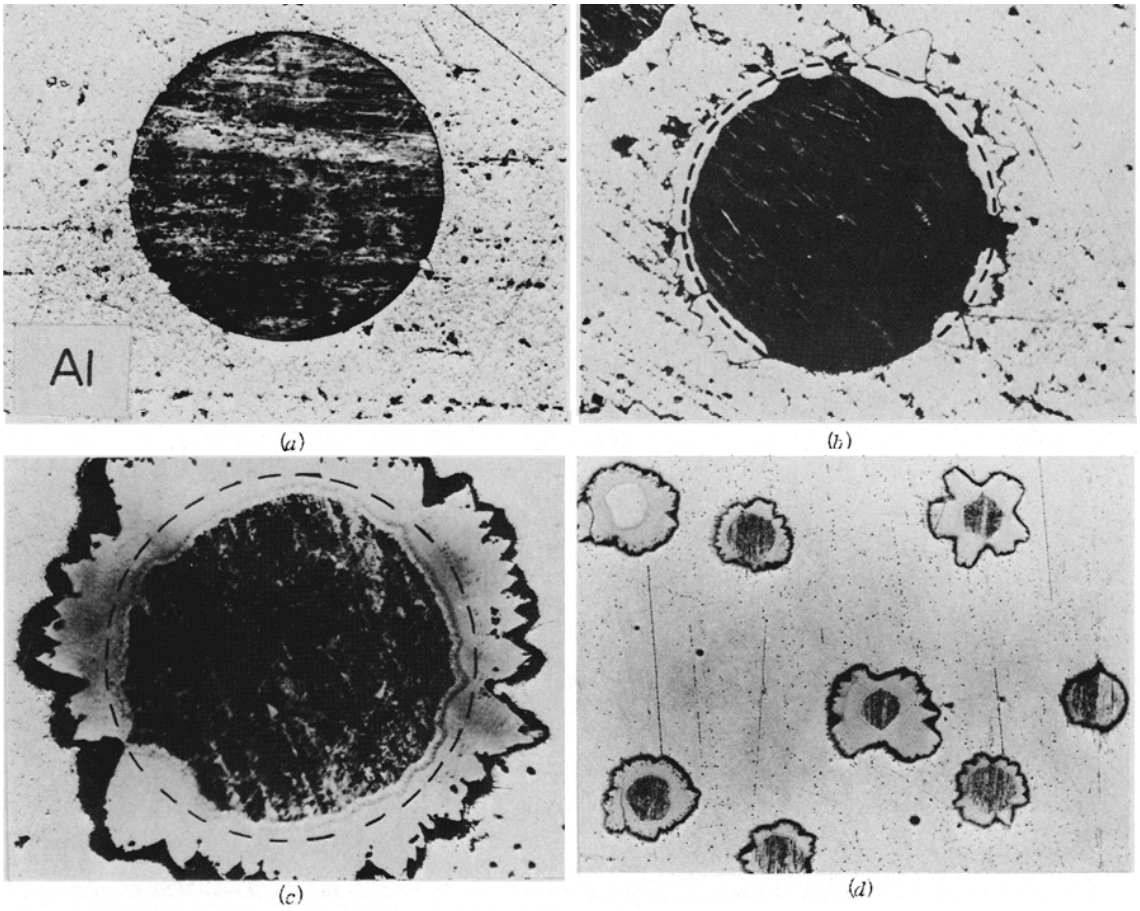

Figure 2.2: *Four micrographs of the fibre-matrix interface shown after (a) as pressed (at 510°C); x275 magnification; (b) heat treatment at 550°C, x275 mag; (c) heat treatment at 625°C, x325 mag; (d) heat treatment at 625°C, x50 mag [6]. The lack of reaction below 550°C is in agreement with other sources, as are the two phases of growth [39]. Care must be taken with HIP conditions if a regular interface is to be formed.*

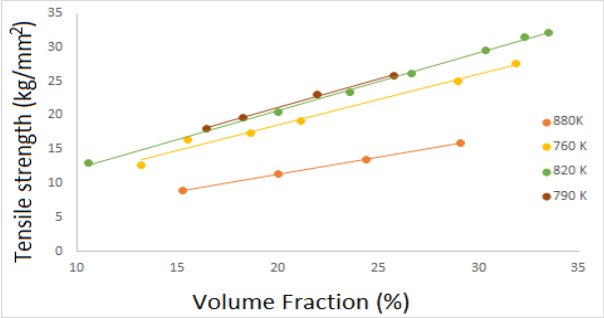

(a) *Tensile strength versus reinforcement volume fraction across a range of HIP temperatures*

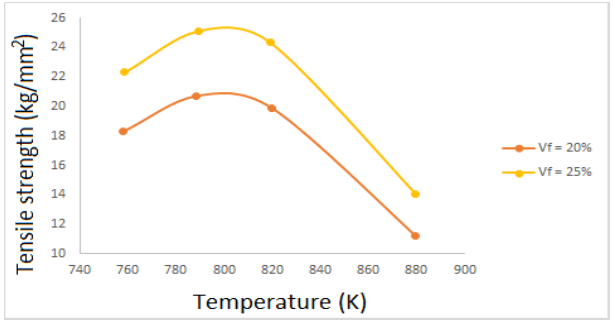

(b) *Tensile strength vs HIP temperature for 20% vol and 25% vol reinforcement fibres.*

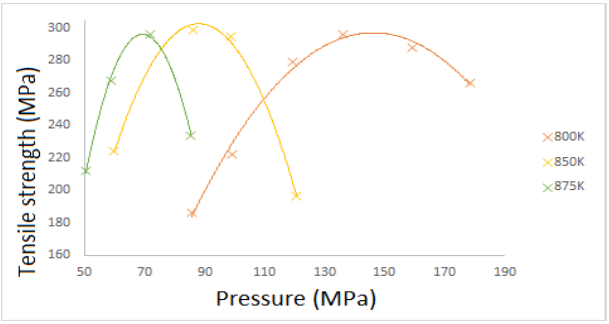

(c) *Tensile strength vs HIP pressure for three different HIP temperatures. The optimum pressure, within experimental error, the same independent of HIP temperature, though the effect is stronger at higher HIP temperatures.*

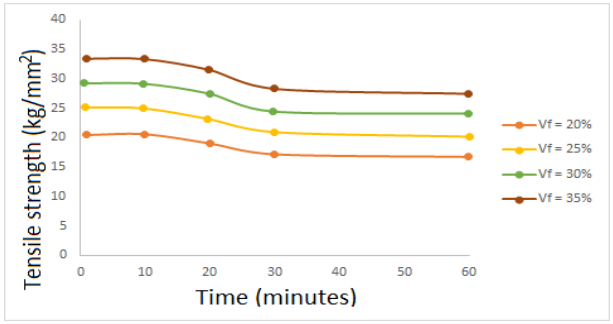

(d) *Tensile strength vs HIP dwell time for a range of volume fractions. After consolidation, strength degraded with HIP time towards an equilibrium reached at 30 minutes. The trends are the same shape for all reinforcement fractions.*

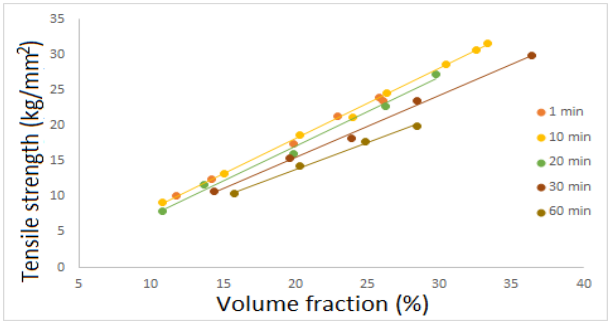

(e) *Tensile strength vs reinforcement volume fraction for a range of HIP dwell times. Both factors have a very strong effect on the final strength.*

Figure 2.3: *Curve-fits for the effects of time, temperature, reinforcement fraction and pressure when HIP processing an Al-stainless steel composite. The optimum temperature was 525°C; optimum pressure was 150 MN/m^2. Pressing time should be minimised, and the volume fraction did not reach detrimental levels. Data taken from Bhagat et al [40].*

Uses of an Induction Furnace in Composite Manufacture

Induction furnaces have been used in the manufacture of composite materials for their rapid heating and fast response rate as well as their stirring effects.

Induction furnaces have been used in MMC manufacture as a replacement for the hot isostatic press (HIP) [44] with good results. An iron-alumina composite was manufactured by milling and mixing powdered Fe2O3 and FeAl, which were then inserted into a graphite die and surrounded by an induction coil, then the coil was placed under vacuum and uniaxial pressure of 80 MPa was applied, followed by heating to 550°C. The resulting composite, of mixed Fe and Al_2O_3, reached 95% relative density and had grain sizes of 72 nm and 43 nm, respectively.

The magnetic stirring effect of the induction furnace has been used [45] to mix an alloy of Al 2024 and SiC during solidification. It was found that the grain structure was finest and most homogeneous if the mixture was cooled rapidly after reaching the semi-solid state, rather than being continuously magnetically stirred during crystal growth. It is suggested that the stirring effect is only beneficial at low and medium shear velocities.

Degnan et al and Kattamis et al [46] [47] combined the magnetic stirring effect of the induction furnace with a mechanical impeller mixer to produce Fe/TiC composites, with some success. A similar procedure, which has been used in this work and is described in Section 3.3 was developed by Dr Yang [19] for Al/SiC manufacture, and Jeon et al [48] preserved the dispersion of SiC reinforcement in composite ingots by slowly reheating in an induction furnace followed by brief stirring and casting.

Varin et al [49] used an induction furnace to melt and mix Al3Zr and Al3Ti such that when they had reacted and the melt solidified an intermetallic-hardened composite would be produced by precipitation at crystal grain boundaries.

Other Techniques

Foamed metallic materials are of interest because of their very good strength-to-weight ratio. Dunleavy et al [17] prepared a composite of Al and Al_2O_3 by taking a commercially avaliable porous network of pure Al and electrochemically oxidising its surface, creating a network of ceramic distributed through the Al foam. They found it possible to create composites of up to 90% ceramic. Song et al [50] produced an Al/AlN composite by introducing TiH_2 particles to a melt of Al and AlN, which caused the production of many hydrogen bubbles which remained present after the ingot had been cooled in room-temperature air. Both reactive composite formation and metal foaming were used by Linul et al [51] to produce an Al foam faced with stainless steel mesh.

Because of the intention to use entirely different materials for the matrix and reinforcement, it will not be possible to use many of the more promising methods of manufacture developed for ceramic/metal or metal/ceramic composites such as in-situ reaction formation [17].

Cold spark plasma sintering of aluminium 1056 and 99% pure vanadium carbide [52] at 300 MPa and 220°C produced a composite with no reaction products between the VC and the Al. The resulting composite had not lost the "scale-like" characteristis of the powders used to produce it but a relative density in excess of 90% was observed and a bending strength of 330 MPa.

Spark plasma sintering has also been used [53] to produce a continuous-fibre-reinforced composite with no voids shown and little fibre damage when sintered for 10 minutes at 550°C after exposure to 500°C and 50 MPa in a press. Fewer aluminium carbides were found than would be expected from a liquid infiltration route.

2.5 Bulk Properties of MMCs and HMMCs

When a composite is placed under stress, its load response can be divided into three areas: the matrix, the reinforcement and the interface between the two. It is this last which is thought to form the "critical weakness" of the system [7], though damage localisation may be a more significant factor in practise [36].

The strain response of a material is substantially affected by the types of hardening it may undergo. The two most significant mechanisms of hardening are ageing and work hardening. Age hardening, or precipitation hardening, involves careful control of the thermal history of a composite to precipitate alloyants at the grain boundaries [26].

These precipitates impede dislocation motion, increasing the local stiffness of the metal. Whether a material is strengthened by thermal ageing will depend upon its chemistry. For example, Dong et al [54] found that in a short-fibrereinforced MMC, heat treatment increased the UTS but decreased the elastic modulus.

The detrimental effect of a very thick matrix-fibre interface on composite properties [6] means that it is impractical to age-harden a composite material, because the temperatures needed to do so in aluminium alloys are above the fibre/matrix reaction threshold. If an age-hardened matrix alloy is required, or if age-hardening is strongly desired, it may be possible to produce "pre-hardened" materials by sintering or HIPing.

Work hardening occurs when the increasing lattice mismatches (dislocations) introduced by plastic flow begin to impede the creation of new dislocations and the 'flow' of existing ones [26]. Whether a material can be usefully work-hardened will depend on whether useful dislocations or detrimental fatigue micro-cracks are introduced by light deformation. Evidence that HMMCs can be work-hardened is presented in Section 5.3.2.

Strengthening models are typically treated as additive [26] rather than as interfering with one another, though this is not necessarily true in edge cases such as damage localisation.

Fibre-reinforced composites typically exhibit high strength and specific strength, low ductility, poor corrosion resistance and poor toughness [8]. Usually, any given property of a composite (such as its tensile strength) will be somewhere between that of the matrix and that of the reinforcement [40]. This relationship will sit between one of the two bounds defined by the Rule of Mixtures, Equations 2.3 and 2.4. Properties of some specific composites are presented in Figure 2.1.

The ductility of the composite will decrease very substantially relative to its matrix even at low volume fractions of reinforcement [55] but does not appear to be strongly dependent on the volume

fraction. This suggests that the introduction of reinforcing fibre severely disrupts long-range stress relaxation mechanisms in the matrix. 45% vol is a maximum volume fraction for useful properties in a particulate metal-ceramic composite [3].

The composite can be visualised as a porous network (fibrous reinforcement) surrounded by a medium with strength (the matrix and interface). In a porous material, the supported stresses increase with density [56]. By itself, this suggests that the optimum volume fraction (v_f) for maximum strength is as high as the desired density will permit. However, that has not proved the case [55] [37].

In metal-ceramic composites, the maximum volume fraction was found to be 45%, and in metal-metal composites the wear resistance did not increase appreciably between 20% reinforcement and 40%. This is thought to be due to the lower strength of fibre junctions compared to the fibre-matrix interface: fibre junctions contain two or more fibres "resting" together, with very little bonding occurring between them to provide strength. It also decreases the ability of the matrix to transmit stresses. In HMMCs, there is a suggestion [40] [6] that the optimal reinforcement fraction is between 6.5% and 20%.

Metal-ceramic composite materials are usually of very low ductility [55]. This can be improved by decreasing the strength of the bond between matrix and reinforcement [55]. However, this substantially increases the amount of work hardening the composite will undergo.

Composite behaviour is markedly more sensitive to strain rate than the matrix alloy [11]. There has not yet been a definitive explanation for this, but possibilities include the resistance of reinforcement to crystal dislocation motion and a change in dislocation density due to the mismatched strains in reinforcement and matrix [57].

Other explanations [11] involve the strain rate sensitivity of the reinforcement and the strong strain-localising effects of the fibre network. The density difference between the matrix and the reinforcement means that the stresses will be transmitted at different rates [26], which could also have an effect.

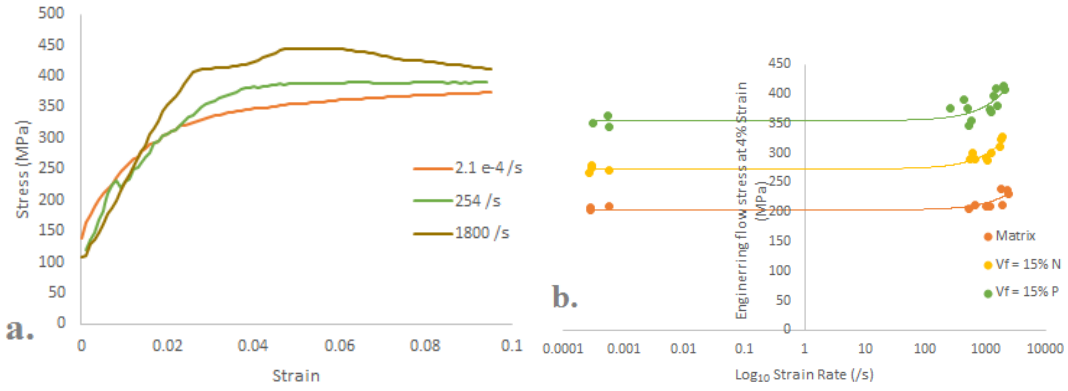

Figure 2.4: *Guden et al [11] created a composite using Al with 1.2% wt Cu and polycrystalline alumina at various volume fractions. (a) stress-strain graphs at three strain rates. (b) flow stress against* $\log_{(}10)$ *strain rate. Data are shown for the matrix and for the composite loaded parallel to the fibre plane (P) and normal to it (N). Distinct changes in strength and slope of stress-strain graphs are visible at different strain rates, which suggests that different deformation mechanisms coming into play. This is particularly apparent at the highest strain rate.*

At higher strain rates, microscopic examination showed that the MMC had failed in shear even under purely compressive loading [11].

Fibre-reinforced composite materials can exhibit highly anisotropic behaviour. Any aligned-fibre composite will be very substantially stronger along the axis of fibre alignment [8] than the axes perpendicular to it. This can be mitigated by layering reinforcements in a ply structure [8], and it is possible to produce near-anisotropic samples with a sufficiently 3D-dispersed fibre arrangement [37].

Generally, fibre-reinforced MMCs fabricated by high-pressure infiltration process have a significantly non-random fibre orientation, which leads to anisotropy in physical and mechanical properties [37]. The orientation is not random because during pressurized infiltration, there is significant fibre flow.

Some examples of the strength and ductility available from a composite made with pure aluminium and stainless steel are shown in Table 2.2.

Source	Composite	Reinforcement vol.%	UTS (MPa)	Strain at Failure
Bhagat [40]	Aluminium and stainless steel (304)	25%	245	–
Bhagat [40]	Aluminium and stainless steel (304)	20%	196	–
Pattnaik [6]	High-purity Al and stainless steel (NS-355)	6.5%	220	2.4%
Pattnaik [6]	High-purity Al and stainless steel (NS-355)	19.6%	600	2.1%
Mandal [7]	LM0 and stainless steel	5%	72	6.5%
Mandal [7]	LM0 and stainless steel with 2μm Cu coating	5%	125	11%

Table 2.2: *Sample properties of HMMC materials produced by HIP (Bhagat et al [40] and Pattnaik et al [6]) and an open-cast method (Mandal et al [7]).*

The physical shape of the reinforcement can play a substantial role in addition to its chemical composition, and thus the interfacial products. Zhang et al [27] found that rod-shaped nanoparticles produced composites of higher strength than spherical ones, and the dependence of strain distribution on loading direction relative to fibre orientation found by Kenningley et al [36] and discussed above would not have applied with spherical reinforcement.

2.5.1 Interface Formation

Mitzumoto et al [37] used thin rod reinforced specimens of SiC reinforcement and AZ91, Al-Si or Al-Cu alloys. They found that there was preferential $Mg_{17}Al_{12}$ at the fibre-matrix interface surrounded by a layer of Mg-α.

Typical compounds found at the interface between steel fibres and an aluminium matrix include FeAl, Fe_2Al_5, Fe_2Al_7 [40]. The ratio between these compounds is influenced by solidification rate and pressure [39].

Iron-aluminium intermetallic compounds are often quite brittle. As such, the formation of an intermetallic layer at the interface of steel fibres and an aluminium matrix, typically FeAl, $FeAl_3$, Fe_2Al_5, Fe_2Al_7 and Fe_3Al_5, will substantially decrease the strength of the final composite [7] [40].

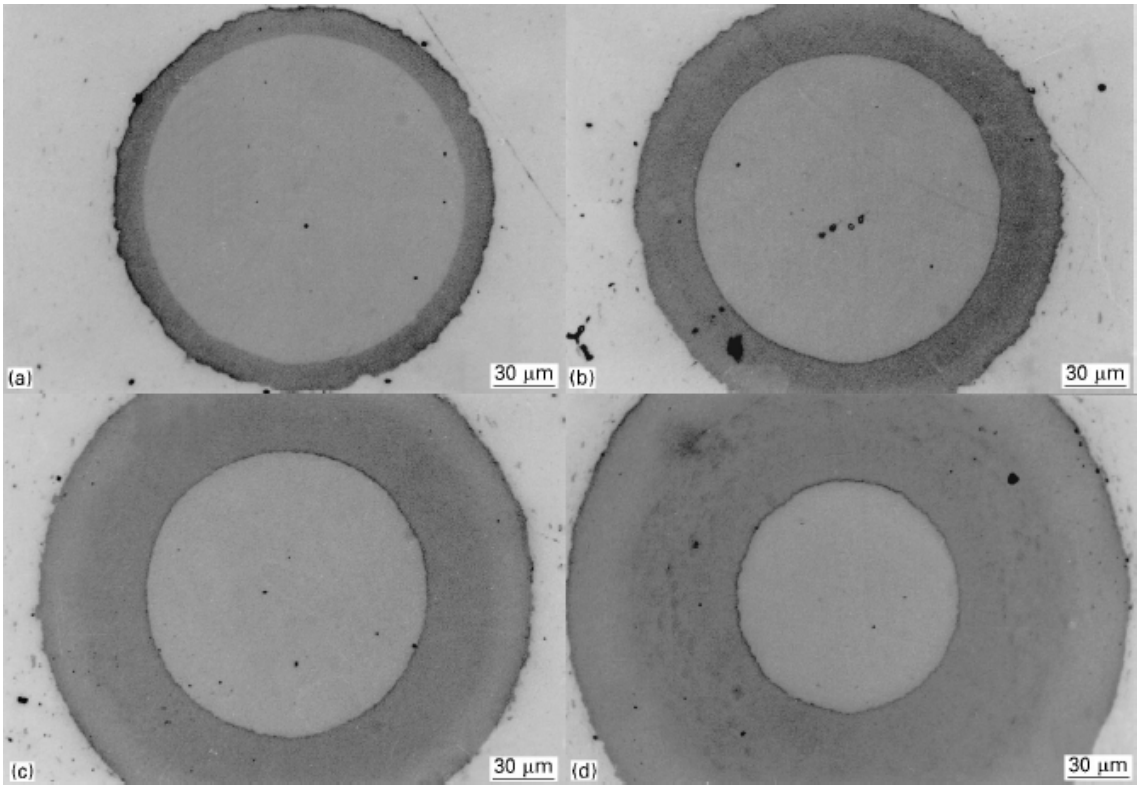

Figure 2.5: *Micrographs of the composites from Hwang et al [39], showing hot pressing at 70 MPa and 600°C for (a)15 min (b) 1 hr (c) 4 hr (d) 16 hr. The thickness of the interface is clearly strongly dependent on HIP time.*

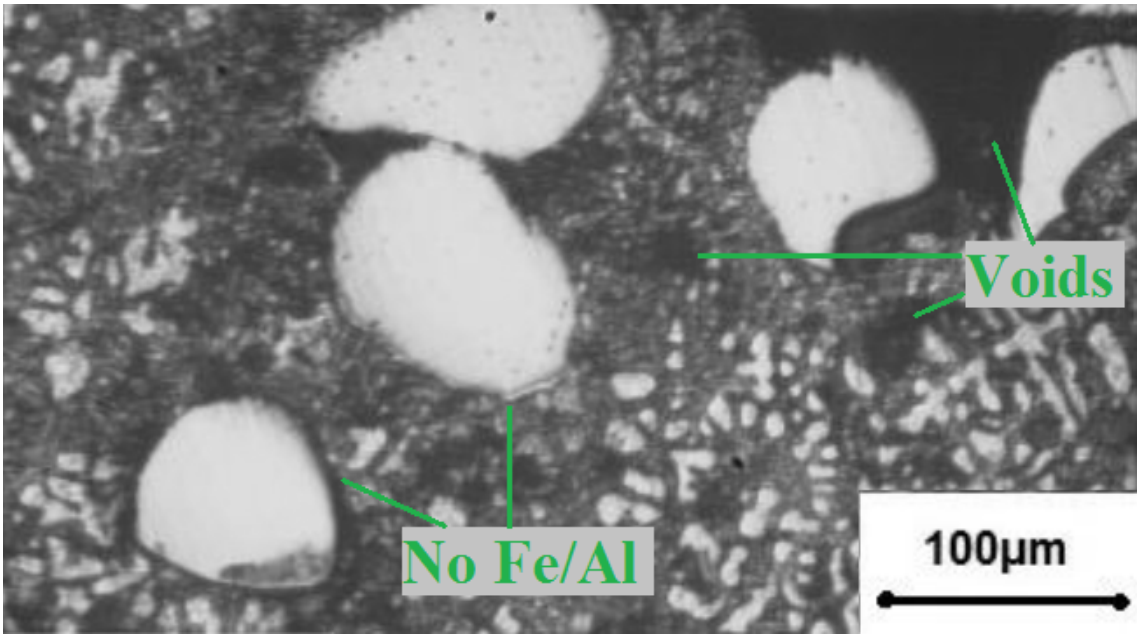

Figure 2.6: *Micrograph of an LM13/steel HMMC in which the steel fibres were coated with Cu and the reinforcement fraction was 5.5 %wt. There does not appear to be any break in the Cu coating which suggests that the interface is composed of Cu/Al compounds rather than Fe/Al. Casting was by a stirring process; image taken from Chelladurai et al [33].*

Fe(Cr, Ni)Al_2, Fe(Cr, Ni)Al_3 and (Fe, Cr, Ni)$_2Al_7$ were also found when using a stainless steel and commercial Al foil.

Adding a thin layer of Cu on the fibre surface acts as a barrier separating the iron and aluminium and prevents the formation of these compounds and significantly increases the strength of the resulting composite but also substantially increases the cost of the fibres [7] [33]. A microstructural image of such a composite is presented in Figure 2.6, who used a copper coating, which shows a thin and uniform interfacial region with no apparent breaks in the Cu coating which suggests that it is an effective barrier.

Intermetallic layer formation can also be decreased by choice of matrix alloy (for example, Al 5075 has a substantial Fe content and so will tend not to form Fe intermetallic compounds below around 600°C); and by ensuring that the casting temperature is as low as possible, although this will discourage wetting [4].

The chemistry at the fibre-matrix interface is not straightforward [40], influenced by the different solidification temperatures of matrix and reinforcement and by the diffusion which can occur after solidification but before any quenching. It has been extensively studied [40] [37] [36], and there are some models which describe the solidification in the zone of interest [39].

During the initial solidification process, the degree of eutectic composition in the main interface zone suggests that most of the fibre-matrix reaction occurs when the matrix is still liquid [35], and that solid diffusion is less of an issue. Larger fibres were found to produce a thinner intermetallic layer, probably because the larger radius leaves a smaller solid angle for diffusion to occur across, with thicknesses of around 10 μm.

Using stainless steel rather than carbon steels does not decrease the extent of the iron-aluminium reaction because the CrO at the surface will react to form Fe-Cr-Al and Cr-Al compounds [58], although this suggests that any Ni present was not reacting with the matrix. Later experimentation also found no Ni-Al intermetallic compounds, and while Cr did react it was primarily confined to the Fe-Al intermetallic inclusions, rather than forming Cr-Al compounds and diffusing into the matrix. This is described in Section 3.3.2.

The conditions used to machine the composite must also be carefully considered. It was found [36] that when an HMMC was prepared for fatigue loading in a heated die, the Si particles from the matrix alloy were finer and better distributed in the bottom of the punch, away from the die (heated to half the melting point of the matrix alloy).

It was found that [39] a very uniform interface growth could be achieved by hot pressing under vacuum or under pressures in excess of 70 MPa. An activation energy for the growth of the matrix-fibre interface of 152 KJ/mol was found, 8% lower than that found in other work [59]. This difference is attributed to the increased pressure used when pressing the composite. This translated to a temperature in excess of 550 $^\circ$ C.

Two distinct regions of interface growth were seen [39], the first growing into the fibre and the second growing outwards. The inner zone is harder and has a higher iron concentration. In general, there will be a tendency for more Fe-rich intermetallics to form closer to the fibre and for the more Al-rich compounds to occur further into the matrix.

The morphology of interface growth has a very strong determining effect on the strength and failure modes seen in the composite material[41]. When the interface grows into the matrix (which can be determined from radius measurements on the microscopy) as in the case of stainless steel in pure Al, the UTS of the composite decrease slowly. When the interface grows into the fibres, as with NiCr in pure Al, the UTS decreases sharply. This suggests that while an intermetallic layer damages the fibre/matrix bond, the embrittlement of fibres is a far more significant effect.

2.6 Failure Behaviour

In both HMMCs and MMCs, failure can begin in the matrix, the reinforcement or at the interface between the two. It is therefore very important to be able to describe the mechanisms of failure and their appearance in recovered specimens to be able to assess the damage in a particular recovered sample.

In tension or shear loading, typically the matrix will form small cracks, each bridged by one or more fibres [10] before the onset of necking in the matrix. The nature of these bridged cracks will therefore be critical to an understanding of failure behaviour in the composite.

In as-cast composites, under low strain rate tensile loading, wires will neck to failure and show "cup-and-cone" fracture surfaces [6]. This is shown in Figure 2.7a. Debonding of the wires from the matrix can also be seen. This can occur during failure, caused by differences in the expansion-contraction curves of the matrix and reinforcement [37], though delamination is caused by and exaggerated during polishing [6]. (pull-out from the change in CTE is already there)

Outside the interface zone, the matrix initially behaves as if it were annealed unreinforced alloy [6]. When the matrix begins to deform, dislocation cells on the order of 3 m form, almost independent of the proximity of the cells to fibre reinforcement.

At low strain rates ($10^1/s$ or less), the most energy-absorbing failure mode is complete fibre pull-out, followed by matrix fracture and fibre fracture [13]. Promotion of fibre delamination and pull-out in preference to fracture will thus increase the tensile strength of the composite. If fibre

pull-out is rendered more energy-absorbing, by methods such as the use of non-cylindrical fibres, this is also expected to increase the energy of failure and thus the tensile (or shear) strength.

Any change which increased the obstacles to fibre pull-out increased the ultimate tensile strength. This was seen in both the simulations of Dong et al [54] and the experimental results of Pemberton et al [10] and Banthia et al [13]. Fibre pull-out can be reduced very effectively by using imperfectly cylindrical fibres. The non-cylindrical shape can be in the overall fibre shape i.e. using crimped or end-hooked fibres or non-circular fibre cross-section. In both cases, the non-cylindrical fibre is better anchored to its surrounding matrix.

Under compressive loading, fibre fracture is not immediately catastrophic. The fractured fibres are simply re-loaded as multiple, shorter fibres and will continue to strengthen the matrix [11]. At low strain rates, the primary damage mechanism remains matrix flow but at higher strain rates fibre damage and its consequences begin to dominate. The fracture of a fibre creates a strong stress-localising effect, which also sensitises the matrix to strain rate far more than it otherwise would have been.

The presence of fibres in the composite tends to have a stress-localising effect even when they remain intact [36] [3] because of their shape. However, the widespread micro-yielding seen by several authors [11] [55] [60], while it complicates measurements of the elastic modulus, do not lead to yield in the composite as a whole as such damage would be expected to in a monolithic material.

One mechanism proposed for failure at a fibre-bridged crack is that as the composite is strained (in tension), the reinforcement will pull out of the matrix and cause void formation [55]. At 100% void density (i.e. when all of the reinforcement is fully detached from the matrix) composite fracture will occur. This mechanism agrees with Banthia et al [13], who found that when fibres were only weakly bonded to the matrix, the bond strength governed the composite strength, and Zhao et al [61] who found that the presence of micro-voids degraded the yield strength (0.2%).

Voids tend to form as hemispheres at the ends of a cylindrical fibre reinforcement, and were found [55] to have diameters on the order of the inter-fibre spacing and that they formed along the principal stress axis. The threshold for void formation was found to be 5% of the composite failure

strain. During composite formation, when active diffusion is occurring between fibre and matrix, the Kirkendall effect will lead to void formation [62] [6], making void-nucleated failure a significant prospect.

In ceramic-matrix composites under tension [10] a significant proportion of the fibres in a failed sample had fractured, suggesting that this a significant factor in understanding composite failure. When it occurs, fibre fracture takes a large amount of energy, preventing damage to the matrix in the vicinity.

Shear loading, as opposed to frictional or tensile components, is the primary cause of fibre pull-out [13]. This is supported by the increase in strength when fibre are loaded along their axis [8]. When one fibre fractures or fully detaches from the surrounding matrix, the relaxation caused by this sends out a shear pulse [63] which will in turn provoke delamination and/or fracture in adjacent fibres.

The transfer of strain between the matrix and the fibres can create a stress pulse perpendicular to the loading axis, or interfacial shear pulse [63]. This can lead to catastrophic local relaxation and corresponding stress increases [11], and creates a tendency in all composites to fail in a brittle fashion, even when both matrix and reinforcement are ductile.

The different failure modes seen in compression and tension [11] suggest that the failure modes strongly depend on the loading type seen. It also suggests that multiple simultaneous strain directions should be considered, which is supported by the model presented in [7] and by the observation that the high pressures present in compressive loading suppressed the formation of voids in MMCs [11].

The fracture performance of MMCs is poor in comparison to ceramic-metal composites, which show a fracture toughness on the order of 20kJ [10].

High temperature exposure can have a very significant effect on subsequent behaviour [6]. The inherent chemical imbalances which exist in a composite material permit diffusion and reaction at high temperatures. Examples of composites shown to be detrimened by high-temperature exposure include Cu/W, Ni/C, Ti/Al_2O_3, and Al/Stainless steel.

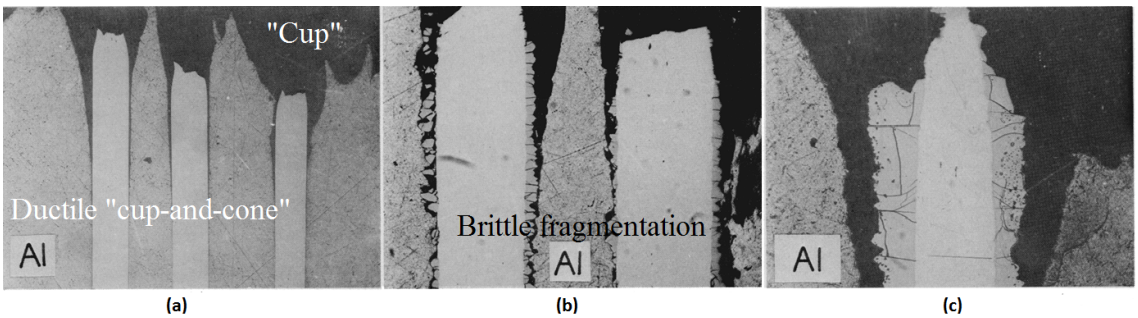

Figure 2.7: *Micrographs of the damage seen in a pule Al-stainless steel composite produced by vacuum hot pressing at 510°C for 4 hours. It was then heat treated and tested to failure in tension. (a) As pressed; shows delamination and ductile failure. (b) Treated at 550°C for 24 hrs, shows some delamination, brittle interface, ultimately ductile failure. (c) Treated at 625°C for 24 hrs, shows extensive cracking and brittle failure [6]. This is an example of the embrittlement of the composite due to the Fe-Al reaction products discussed.*

v_f	Condition	E (stage 1) (GPa)	Stress S1/S2 (MPa)	Stress S2/S3 (MPa)	UTS (MPa)	Strain at Failure %
6.5%	As-Pressed	74.5	12.1	131	220	2.4
6.5%	550°C	74.9	15.5	103	193	2.6
6.5%	625°C	77.8	22.4	83	100	1.3
19.6%	As-Pressed	93.0	33.8	379	607	2.1
19.6%	550°C	94.3	44.8	228	476	2.1
19.6%	625°C	98.0	62.1	124	234	1.3

Table 2.3: *An example of the effects of heat treatment on composite properties. The tensile strength and stress at failure both degrade with increasing ageing time, but the strain at failure improves or remains the same after treatment at 550°C, which is close to the activation energy of the fibre-matrix reaction. Data are from [6]*

The difference in the coefficients of thermal expansion between the fibres and the matrix will also cause the fibres to pull away from the matrix after high-temperature exposure [7]. This effect is exaggerated when a sample is prepared for microscopy.

Differing thermal expansions between matrix and reinforcement also lead to visco-plasticity and creep [36]. When testing a composite for thermal fatigue, the majority of the plastic strain was accumulated in the first heating/cooling cycle. Samples were tested either as-cast or over-aged at 350°C for 200 hrs. Thermal fatigue testing was performed over 3 triangular wave cycles of 350°C, 400°C, 450°C, 2 K/min. (Based on the typical, rated, and overload temperatures for a diesel piston).

Subsequent cycles saw significant creep and some release of strain accumulated in previous cycles. The alleviation of strain by creep and matrix flow may explain the better strain recovery seen at higher temperatures [36].

A proposed mechanism for the reduction of strength in an aluminium/steel composite seen with increasing heat treatment is a decrease in load-bearing capacity in the matrix/interface, specifically cracking in the reaction zone which notches the fibre and induces brittle failure. Boron-reinforced titanium and carbon-reinforced nickel also showed a degradation of tensile strength after elevated temperature exposure [6].

Baker et al, as reported by Pattnaik [6], saw an increase in fracture toughness at the formation of a reaction zone, which began to decrease after the zone reached a certain thickness. In addition, extracted wires from the 625°C composite displayed a bimodal strength distribution, similar to that found in boron or glass. The average strength is therefore a weighted average of these two strengths. In all cases, the results are within 5% of those predicted by the rule of mixtures [26]

After 550°C exposure [6], results remained within 12% of their as-cast values, assuming the increased v_f from the reaction zone. Two major zones exist in terms of composition: an inner, larger 57Fe-39Al-4Cr zone and an outer zone with less Cr. The outer zone, while observed, peeled away sufficiently during the polishing process that it was not analysed in detail.

Some deterioration of the wire properties, particularly a decrease in its strength, is expected when

compared with as-received wire. This is because the thermal cycle of composite production will degrade any heat treatment used. In particular, solute precipitation at grain boundaries has been observed [6].

2.7 High Strain Rates - Behaviour and Techniques

2.7.1 Behaviour

When a material is subjected to strain rates above 10^3/s, they undergo different failure mechanisms than quasi-statically, which are examined in Chapter 5.

An Al-W cold isostatic pressed (CIPed) composite has been tested under explosive loading [42]. Al/W is expected to provide very tiny fragments due to the great differences in shock impedence, which is related to density [31]. 20 μm is the maximum combustible diameter for fragments. [42]

Loading an Al-W composite which is 24% wt tungsten and 69% vol Al with a porosity of 8% to 15% in a ballistic ring produces fragments with an average size of 10 μm ranging from 1-100. [42]. Global explosion response is insensitive to the grain size in microstructure.

Lee et al [64] found that very high SiC volume fractions, in excess of 55%, made for strong but brittle materials. More ductile under dynamic loading. Both QS and dynamic tests showed shear banding and cracks at 45° to the loading plane. In a related work [65] on AA 7075 with 56 %wt of SiC particulates also found both strain rate hardening and shear cracks at 45°.

AA 5083 reinforced with 40 nm B_4C at 5%vol was found to soften under high rate loading [66]. Because the test can be assumed to be adiabatic rather than isothermal, this is thought to be due to local thermal softening of the material. This composite was also found to exhibit substantial shear banding, thought to be suppressed by micrometer-scale reinforcement particles.

Heat treatment improved the strength but reduced the ductility, as would be expected in A356 [64]. The peak strength found, of 636 MPa, was an improvement over 524 MPa in the as-cast material. The rule of mixtures was used by the authors to reach an approximation of the properties.

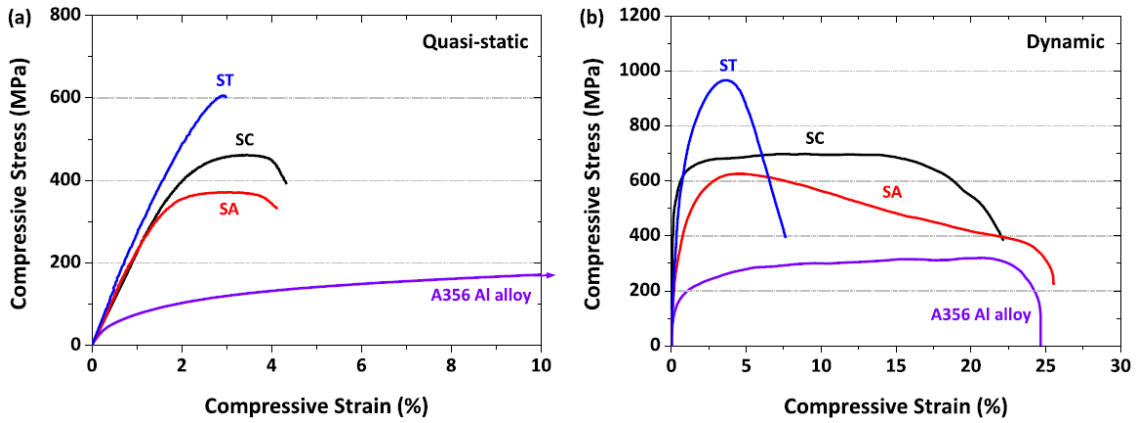

Figure 2.8: *Quasi-static (a) versus dynamic (b) compression curves for an A356 composite. ST, SC and SA describe specimens with 54.6 %vol, 56.3 %vol and 58.1 %vol SiC respectively.*

Energy absorption was hypothesized to be primarily by spot-melting of Al and deformation bands [67] [68]. In the latter work, only one of the three specimens was found to exhibit strain hardening according the the measured stress/strain curves. The peak strains supported were found [69] to double under dynamic loading.

2.7.2 The Split-Hopkinson Pressure Bar

The Split-Hopkinson Pressure Bar (SHPB), or Kolsky bar, is a high strain, high-strain-rate, non-shock technique. Developed by Kolsky [70], it takes advantage of the fact that the pressure-response characteristics of a material can be reconstructed from the amplitudes of waves transmitted and reflected across it. This permits the analysis of sample behaviour by indirect measurement.

The SHPB is used to deliver hundreds of kilopascals to a sample over a few microseconds, typically in compression and as a flat load, although torsional, tension and stepped-load versions exist.

Stepped loading was delivered by means of a compound striker bar, composed either of two materials with dissimilar impedances or of a single bar which had been partially hollowed out. The placement of the lower-impedance section determined whether a “step-up” or a “step-down” loading pulse was delivered to the sample.

A fundamental assumption of the SHPB is that the sample has reached stress equilibrium before the pressure wave has been transmitted entirely through the sample, such that the deformation which occurs is a straightforward function of the incident and transmitted pressure waves. While there is a period during which the sample is not in equilibrium, known as "ringing up", it is assumed that the sample is not significantly damaged during this period so that it is still responding elastically and it can be ignored in the analysis.

As the measurement is indirect, there are no strain gauges placed inside the sample, and so they will not affect its behaviour. This in turn enables far smaller samples to be considered representative of the bulk properties of a material, and so it can undergo large deformations with forces which can be readily reached in the laboratory. The stress-strain analysis assumes that the sample is deforming homogeneously and uniaxially, and that it is in stress equilibrium. The most common source of error in SHPB analysis [71] is that the data cover a period in which the specimen is not in force equilibrium. Whether this is the case can be determined by comparison of the incident and transmitted signals: if the specimen is not in equilibrium, the forces on the two faces of the sample will not be equal.

The principal sources of error come from noise in the system and from Pochammer-Chree oscillations ("ringing"). Methods for reducing and correcting for these have been well-researched [71]. Methods include using Fourier transforms to remove specific noise sources and pulse shaping devices to correct for ringing. A single, sharp spike in the oscilloscope data may be seen [72], which can be a result of the delaying effect of radial inertia in the test specimen.

Brittle materials such as rock, concrete or ceramic also pose a challenge to the SHPB system, as they become damaged after strains of approximately 1% [71]. After this occurs, the stress-strain data becomes useful only as a qualitative gauge of events.

Drodge et al [73] modified the SHPB apparatus to enable the measurement of the high-strain-rate elastic modulus of polymers. As discussed earlier, polymer properties are strongly dependant on strain rate and polymer samples do not equilibrate quickly on the timescale of SHPB tests. The authors compared pulse shaping and frequency-domain analysis intended to permit the calculation of sample properties before equilibrium is reached.

Neither pulse shaping nor frequency-domain analysis was without problems, and the agreement between model and experiment was not better than order-of-magnitude. The frequency-domain analysis also requires a modification of the standard SHPB, with input and output bars two to four times longer than the 500mm seen in the Imperial College system [73]. As yet, this method is not sufficient to obtain reliable data for the high strain rate elastic modulus of polymers, and is therefore not useful here.

Metal deformations on the size and time scales relevant to this work, i.e. millimeters and microseconds, are governed primarily by dislocations and by phase transitions [26] as discussed in Chapter 2. In this regime, the expected phase transitions would be between different atomic structures, such as the body-centered-cubic to face-centered-cubic transition in steel at around 1000K [8].

When measuring the behaviour of a material at high strain rates, it is highly important to ensure that the sample is in stress equilibrium. If a sample is not in equilibrium then an area of stress concentration can begin to deform or crack, giving incorrect values of flow stress or damage threshold for the material as a whole. Stress concentrations of this type are very difficult to measure, and if at all possible should be avoided. This makes the measurement of low-strain behaviour at high strain rates very challenging, and creates the need for a compromise on sample size, as larger samples are more representative of the bulk properties of the material but take longer to reach equilibrium and are more subject to inertial effects [74].

"Bulk behaviour" means that the internal matter should have a much greater contribution to sample behaviour than the surface matter; a commonly-accepted "rule of thumb" is that the minimum sample size for crystalline materials is 1,000 crystal grains [75]. For polymers, the minimum representative volume is both larger and less well-defined [76] and for a composite material it is not known. However, it is hoped that samples with a volume on the order of mm^3 should be sufficient. For these reasons, whether these specimens were truly representative of bulk behaviour may be questioned, however analysis has been attempted regardless.

It is very important to consider the effects of specimen dimensions on its loading response [75] [77]. If a specimen is too thin in comparison to its diameter, radial inertia and interfacial friction

with the bars will dominate its behaviour. This friction will play a highly detrimental role, causing barrelling in the specimen which will in turn exacerbate the effects of any sample anisotropy. The following equation has been presented for the ideal length-to-diameter ratio:

$$\frac{l}{d} = \sqrt{\frac{3\nu_s}{4}} \tag{2.1}$$

The above equation was derived by choosing the ratio of specimen length to diameter such as to cancel the inertial term when considering radial, axial and inertial forces [78]. However, non-isotropic and easily damaged samples, such as polymers or composites, have a less clear optimum aspect ratio [79] [72]. In this case, the aspect ratio chosen was based on the minimum size thought to be machinable.

A standard SHPB system is comprised of four bars, a gas gun and a small cylindrical sample, arranged as shown in Figure 2.10. The SHPB system described in this work belonged to the Institute of Shock Physics at Imperial College London.

Kolsky [70] showed that as the striker bar impacts the input bar, a symmetrical compression wave will be generated in the input and striker bar, travelling away from the site of impact. The compression wave in the incident bar will then be transmitted through the sample and into the output bar, while the compression wave in the striker bar reflects from its rear surface as a rarefaction wave. This will then be transmitted through the striker and incident bars into the sample, which will unload it as shown in Figure 2.9. Further reflections through the system will reload the sample and can be seen in the raw oscilloscope data, but this subsequent loading is not usually considered when analysing the sample response.

To ensure that the compression and rarefaction waves propagate through the system as shown, it is necessary to ensure that the striker bar is of the same material as the input and output bars, and that the sample is of lower impedance than the bars [71] [70]. However, if the impedance mismatch between the sample and the bars is too great, poor transmission of the initial compression wave will be seen, and so this should be avoided. This is typically a problem for soft polymers rather than metals, and so it is not expected to present a problem for the composite material.

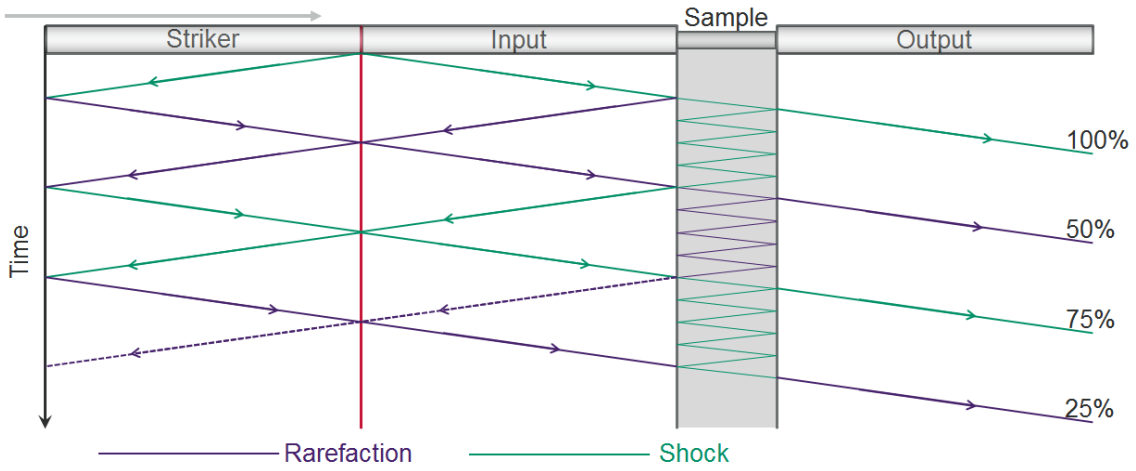

Figure 2.9: *Schematic diagram of the loading in an SHPB system. The impact of the striker bar will generate a symmetrical compression wave which will propagate forwards through the incident bar and into the sample and backwards through the striker bar and reflect from the rear of the bar as a rarefaction wave. This rarefaction wave will then travel forwards into the input bar and through the sample, largely unloading it. The diagram shown is somewhat simplified as it does not include reflections from the input bar/sample interface.*

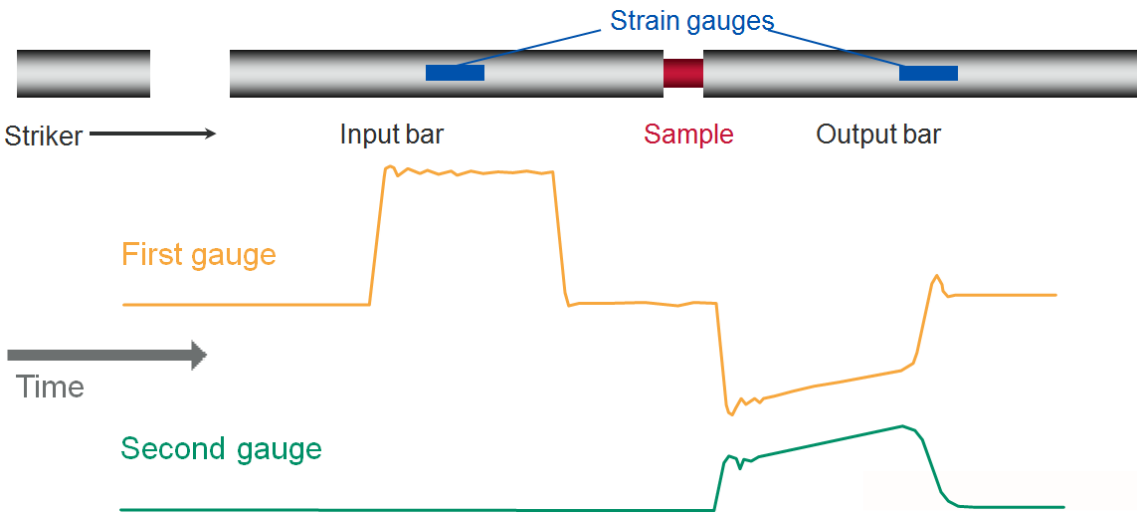

Figure 2.10: *Schematic diagram of the SHPB system, showing the striker bar (typically accelerated by a pulse of compressed air) incident from the left. It will impact the input bar, generating a compression pulse which will travel through the input bar, sample and output bar and be recorded by the strain gauges.*

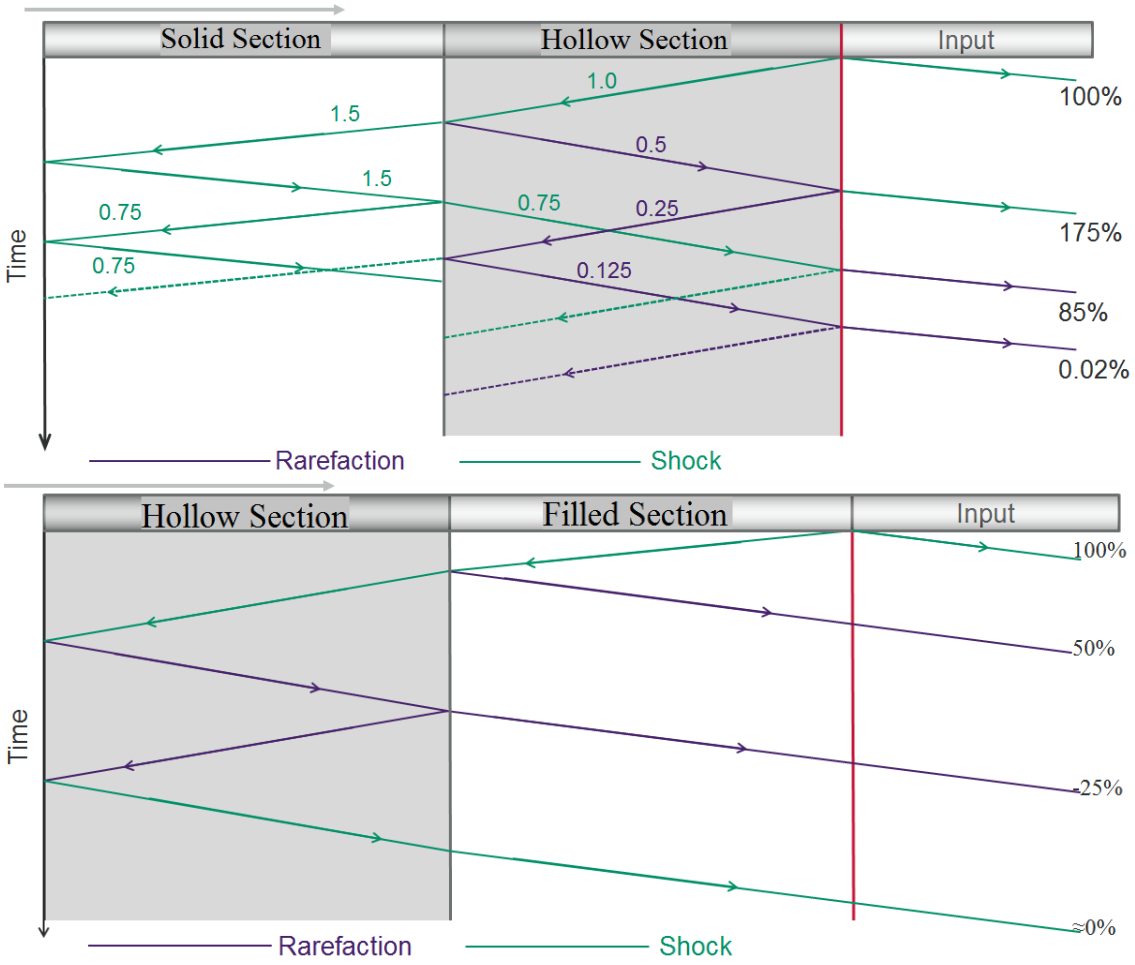

Figure 2.11: *Schematic diagrams showing the effects of a compound striker bar. If the lower-impedance bar was placed on the left, the loading pulse produced will step down; if it was placed on the right, it will step up. Diagrams are based on those in Williamson* et al*[75].*

Figure 2.12: *Schematic diagram of the partially-hollow striker bar system. The bar should be placed with the hollow end towards the striker bar for step up loading and with the hollow end away from the striker bar for step down loading.*

As shown in Figure 2.11, a stepped load in the SHPB can be effected by creating a sharp change in the acoustic impedance of the striker bar. This can be achieved by taking two shorter striker bars and sending them together through the system or by using a single-material bar and partially hollowing it, as shown in Figure 2.12.

The partially hollowed bar circumvents the experimental challenges of a bar composed of two materials but is modelling the compression wave in it is difficult. The compression wave propagates though a hollow cylinder as opposed to a solid one, and wave transmission and reflection at the solid/hollow interfaces is far from straightforward.

Comparing the wave profile which would be expected if the hollow portion of the striker bar were a metal cylinder with an effective density given by

$$\rho_{eff} = \frac{m}{\pi r_o l} \tag{2.2}$$

(in which ρ_{eff} is the effective density, m is the mass of that section of bar, l is the bar length and r_o is its outer radius) gave good agreement with experimental tests [80].

Tests showed [80] that while a partially hollow bar imparted momentum as if the two sections were solids with different densities, pressure waves propagated at the sound speed of the alloy.

2.7.3 Simulations

Simulations of the two striker systems considered in this project were performed using the ANSYS package before any designs were finalised. These were intended to provide first-order validation of the working assumptions used in designing the striker bars. The SHPB setup as shown in Figure 2.10 was modelled as shown in Figure 2.13 and run once in order to confirm that the system was an approximately valid model of the SHPB. The model was then modified to incorporate a partially-hollow striker bar as in Figure2.12, arranged to show step up loading.

The model used the ANSYS Explicit Dynamics simulation package in ANSYS Workbench, to take advantage of the user interface and CAD package. The materials used in the simulation were the best match for the real system available in the inbuilt libraries: nickel alloy (to model Inconel), structural steel, Al-6061-T6 and polycarbonate. Whilst using these materials decreased the realism of the model, it was decided that it would sufficiently reflect the real SHPB system, particularly considering the difficulty of obtaining reliable material properties.

The timespan of the simulation was chosen in order to observe compression of the sample while maintaining a simple and verifiably realistic setup. This corresponded to the period from just before the initial impact of the striker bar to the end of the compression wave passing through the sample. This also removed the need for a momentum bar, as reflections from the end of the output bar would not have reached the sample during the simulation.

The outer sample bar was given an initial velocity of 15 m/s and no other forces were acting on the system. The absences of gravity and friction are a fair model of the barrel, supports and lubrication in the real system, and again this contributes to a simple model. The simulation measured stress and strain on the sample, and results bar are shown below.

The model of the partially-hollow bar had to be somewhat modified in order to obey the constraints of the ANSYS system. The hollow and solid sections of the bar were modelled separated by a very small distance. The setup was almost identical to that of a compound bar, with lengths for the hollow and solid striker sections taken from the calculations described above. Figures 2.14 and 2.15 show the simulated stress in an Al specimen from impacts with the stepped-loading striker

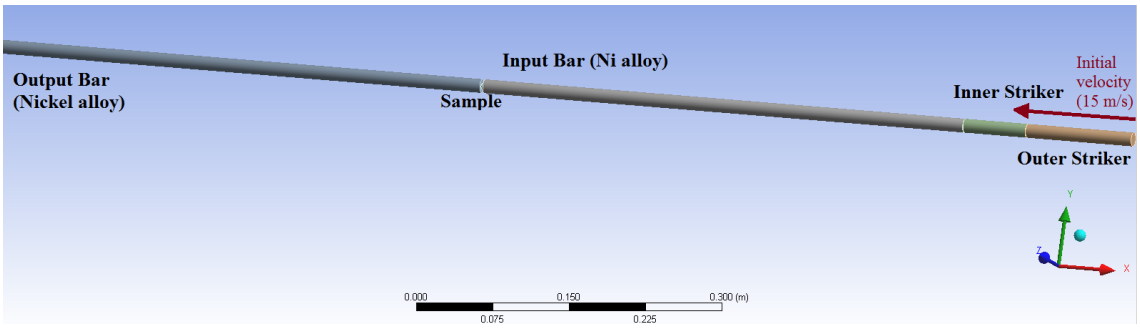

Figure 2.13: *The initial setup of the bars for simulation. Each bar sits slightly apart from its neighbour, and the inner striker bar segment is either structural steel or hollow aluminium, for the two simulations. The outer bar segment has an incident velocity of 15 m/s and the sample was pure aluminium.*

bar before and after the step has reached the specimen. The simulations agree that the step in stress will be transmitted into the sample. These simulations are used to validate the choice of stepped loads to demonstrate whether the composite material is able to mitigate a sharp change in the applied load.

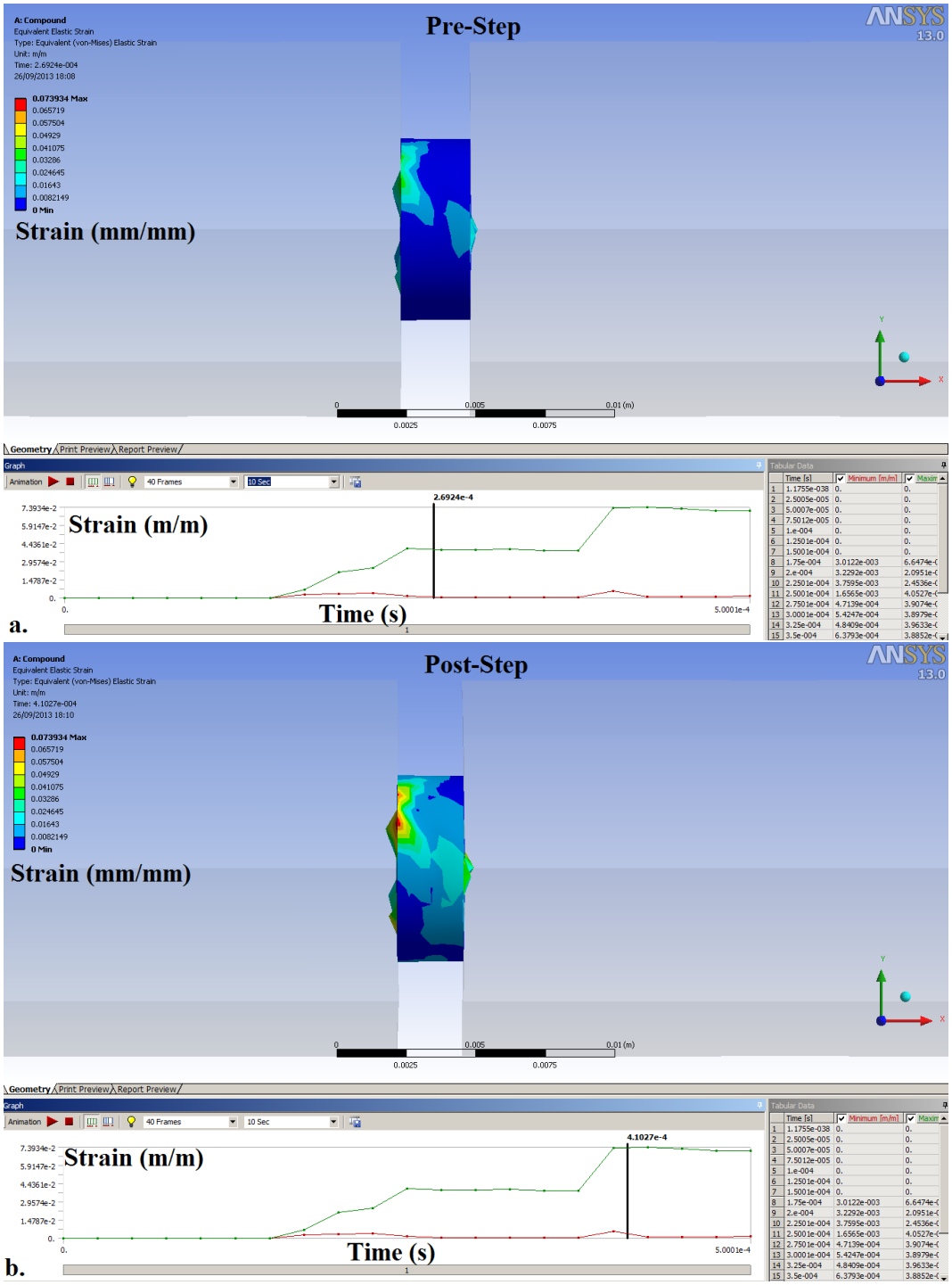

Figure 2.14: *Snapshots of the simulation results showing step-up loading for the compound bar. As can be seen in the graph at the base of the pictures, strain in the sample sharply increases approximately half-way through the loading pulse. The main section of the pictures show the strain in the sample immediately after loading and reloading, coloured according to the visible scale. Units for the simulation were mm, μs and g.*

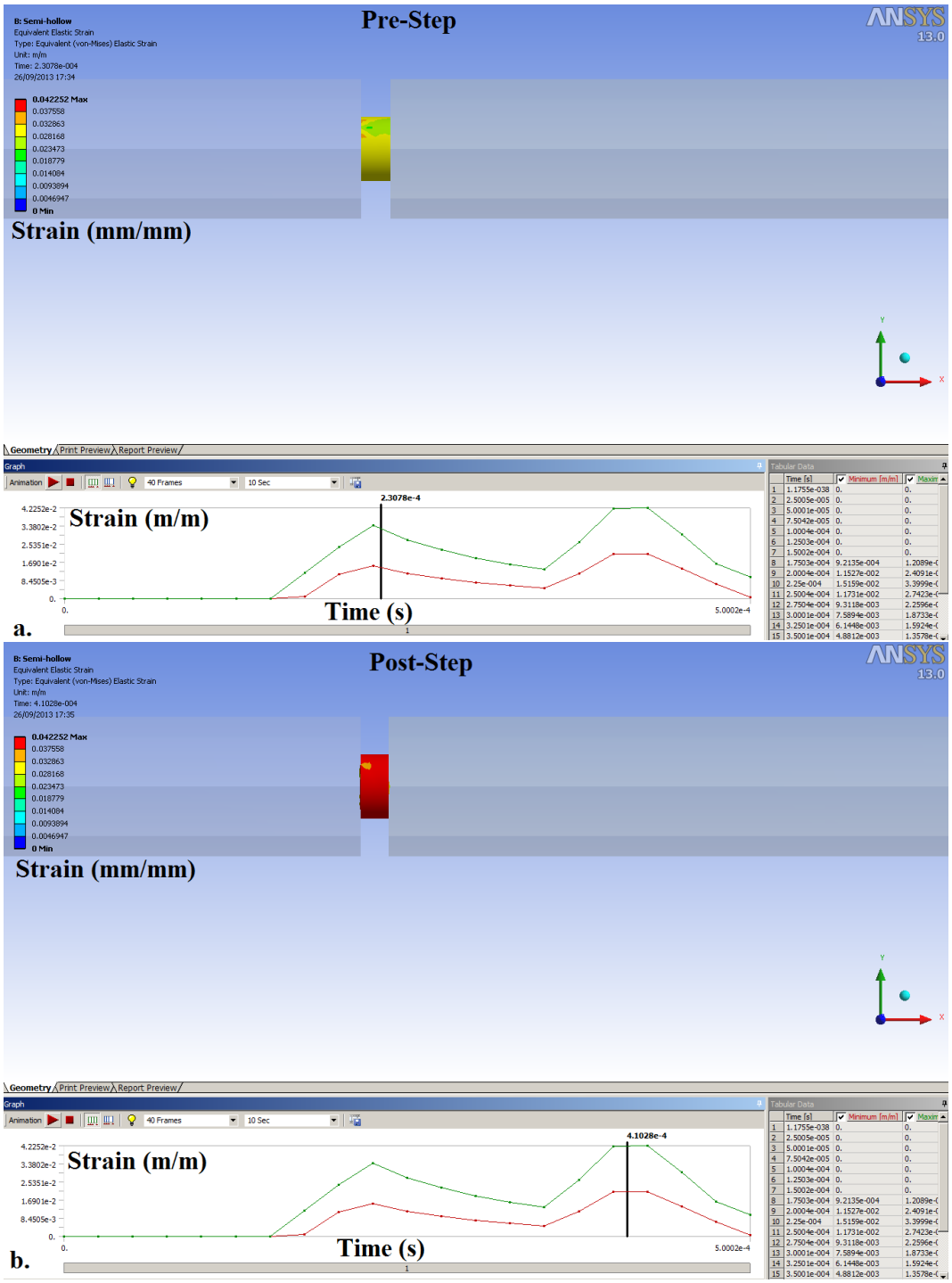

Figure 2.15: *Snapshots of the simulation results showing step-up loading for the partially-hollow bar. While the strain in the sample appears to decrease between the initial loading pulse and before the second load, this was attributed to simulation inaccuracies. The main section of the pictures show the strain in the sample immediately after loading and reloading, coloured according to the visible scale. Units for the simulation were mm, μs and g.*

2.8 Modelling

Several mechanisms for composite failure have been proposed. Several of them are complementary, but none forms a complete picture.

The rule of mixtures can be used to predict the final properties of a composite, and is an excellent first-order approximation.

It has upper and lower bounds given by

$$\sigma_u = v_f\sigma_f + (1 - v_f)\,\sigma_m \tag{2.3}$$

$$\sigma_l = \frac{\sigma_m\sigma_f}{v_f\sigma_f + (1 - v_f)\,\sigma_m} \tag{2.4}$$

in which σ_u and σ_l are the upper and lower bounds for composite strength, v_f is the fraction of the composite volume filled with reinforcement, and σ_f and σ_m are the strengths of the fibre and the matrix.

The rule should be used with caution, however, as it has been found [40] to underestimate the maximum achievable strength in composites prepared using the HIP and takes no account of the very significant effects of thermal history [6].

For a composite with a random fibre alignment [8], an "efficiency factor" is introduced to the matrix strength to account for the random orientation of the fibres: it is deemed that in three dimensions, this is the summed contributions of partially-aligned fibres to the overall strength [10]. There is some debate about the size of this efficiency factor, as Guden et al [11] quote 0.125, Ashby et al [8] quote 0.25, and Callister et al[81] quote between 0.1 and 0.6.

Similarly, first-order predictions of the elastic modulus of a composite are given, assuming a non-zero interface thickness by [56]

$$E_c = \frac{hE_fE_m}{h_fE_m + h_mE_f} \tag{2.5}$$

in which E_c is the elastic modulus of the composite, h is the total interface thickness, h_f and h_m are the radius of the fibre and length of matrix in the volume cell under consideration, and E_f and E_m are the elastic moduli of the fibre and matrix.

It has been found [81] that for fibre reinforcement to be effective, fibres must exceed a certain minimum length, given

It has been found [81] that for fibre reinforcement to be effective, fibres must exceed a certain minimum length, given by

$$l_c = \frac{\sigma_f d_f}{2\tau_c} \tag{2.6}$$

in which σ_f is the UTS of the fibre and τ_c is the greater of the matrix shear strength and the matrix-fibre bond strength. l_c is the minimum length of fibre at which the stress in the fibre will reach the UTS of its material, and for longer fibres more of the fibre will reach this strength before failing, making this desirable.

Commercial FEA such as ANSYS or Solidworks has shown close agreement with experimental results when simulating post-yield behaviour [9] [56], although it can tend to overestimate strength and stiffness because it assumes perfect rigidity at internal boundaries [82]. It has recently become possible to import the structure of a real composite, as measured by x-ray tomography, into modelling software [83], which improves the accuracy of any FEA models used.

Boundary conditions in a finite element model are extremely important, as simplifications can result in un-physical behaviour from the model as a whole [56], and internal symmetry axes can be used to reduce modelling complexity [3].

A recent model has also attempted to incorporate the effects of plastic strain and failure on the discrete reinfocement within different types of composite [31], with promising results. When modelling plastic strain at rates in excess of 1/s, it is also necessary to incorporate adiabatic local heating [84].

Looking at the effects of the scale of structural features in composite materials, the effects of meso-scale structural features are under investigation, by both experiment and modelling [42]. Chiu et al found that the mesostructural features of granular composites tested under explosive loading significantly affected the fragmentation pattern. Specifically, the presence of high-density rods in an Al matrix caused very different shock behaviour to an equivalent-density monolithic solid. The composite developed force chains, in which when stresses are transmitted between granules they cause them to behave as though linked together, which improved the distribution of the shear loading in the material and localising the damage.

"Slab models" in which the object being modeled is treated as a single-material, single-piece whole are simple and relatively easy to implement, but they cannot be used for any composite material because they assume that the material is continuous [3].

One possible approach to modelling composite behaviour is to treat the fibre network as if it were a porous network, as Hwang et al [56] did with biological "composite" structures such as bone, although a correction factor would be needed to account for the strength of the matrix.

The p-alpha and p-lambda models, among others, describe porous materials under compressive loading [85][86]. The p-alpha model treats the material as if it had the same specific mechanical properties as it would if fully compact, but has a density defined by the density of the porous material and the instantaneous pressure. The p-lambda model is a modification of the p-alpha model which contains an additional term to describe the material in its fully compacted state. However, these models assume negligible shear strength in the material, which makes it unsuitable for use on composites.

In a porous composite tested under quasi-static and dynamic 3-point bending loads [51] the orientation of the pores to the loading axis was found to determine whether the composite failed on the tensile edge or by pore shear within the thickness. The quasi-static loading was performed at 1.67×10^{-4} m/s and the dynamic tests at 2 m/s.

Any computational model would be able to produce better results if it were able to use a fibre network which was representative of that found in a composite. To this end, work has been done [83] to create a digital model of the fibre network in a composite from X-ray CT scans.

The technique used standard image reconstruction tools followed by a segmentation algorithm called "kriging" [83] on each individual CT image, 3D reconstruction and thinning to the medial axis if each "fibre". This network could be modelled directly or imported into other modelling software.

Various mathematical models have been developed which aim to predict the failure behaviour of composites. One such model states that as the composite is strained, the reinforcement will pull out of the matrix, leading to void formation [55]. This model suggests that failure will occur at 100% void density (i.e. when all of the reinforcement is fully detached from the matrix). This is supported by Banthia et al [13], who found that when fibres were only weakly bonded to the matrix, the bond strength governed the composite strength.

Shear lag type models have been shown to be useful in predicting composite behaviour [3]. This approach posits that bonded regions (fibre-fibre, fibre-matrix) facilitate stress transfer, and that shear stresses will transfer primarily at such points, creating a delay in the propagation of stresses.

Pemberton et al [10] detail a model of this type for fracture strength of a ceramic-metal composite. It uses the single-fibre work of deformation, fibre failure strain and interfacial friction/fibre bond strength, and estimates of the proportion of fibres undergoing pull-out as opposed to rupture.

While the number of parameters to be "adjusted" to fit experimental data means that in this case its predictive power is relatively limited, it can give a useful estimate of those parameters which are difficult to measure, such as the ratio of fibre pull-out to fibre fracture.

The fracture strength model [10] in terms of fibre radius and shear stress is given by

$$\tau_i = \frac{r\sigma_f}{2\left(\omega_0 - \omega\right)} \tag{2.7}$$

In which τ is shear stress; σ_f is the applied stress at pull-out point; r is the effective radius (defined below); ω and ω_0 are instantaneous and initial fibre displacement.

The effective cross-sectional area and effective radius of a non-cylindrical fibre, in which d_1 is the larger diameter and d_2 is the smaller diameter [10],

$$A = d_1^2 \frac{\pi - 2}{8} + \frac{d_1 d_2}{2} \tag{2.8}$$

$$r = d_1 \sqrt{\frac{\pi - 2}{8\pi} + \frac{d_2}{d_1} \frac{1}{2\pi}} \tag{2.9}$$

It was hoped that this model could be tested against experimental data, however (as discussed in Section 4.2.1) the stress at pull-out of a single fibre could not be measured and so the attempt was abandoned.

In addition, the efficacy of this model has been questioned [83] both intrinsically and in terms of it applicability to fibre networks, as it considers all deformation other than that along the tested axis to be negligible.

Fibre networks will a low volume fraction and a high aspect ratio can be simulated [83] using an affine model. This assumes that fibre bending is perfectly elastic and symmetrical about the centre point of the free fibre, and that load distribution is homogeneous.

Log stress-strain rate can be modelled

$$\sigma(\dot{\epsilon}) = \sigma_0 + n\dot{\epsilon} \tag{2.10}$$

in which $\sigma(\dot{\epsilon})$ is the flow stress as a function of strain rate ($dot\epsilon$), σ_0 is the flow stress at a reference strain rate, typically quasi-static, and n is the strain rate sensitivity, measured in MPa/s, defined as

$$n = \frac{\sigma_{dynamic} - \sigma_{QS}}{\sigma_{QS}} \tag{2.11}$$

in which $\sigma_{dynamic}$ and σ_{QS} are the dynamic and quasi-static flow stresses. n was found to range from 0.12 to 0.35 for MMCs [11].

When modelling dislocation behaviour, it is preferable to use the dislocation cell size, defined as the mean free path a dislocation will travel before it meets another and is removed, rather than

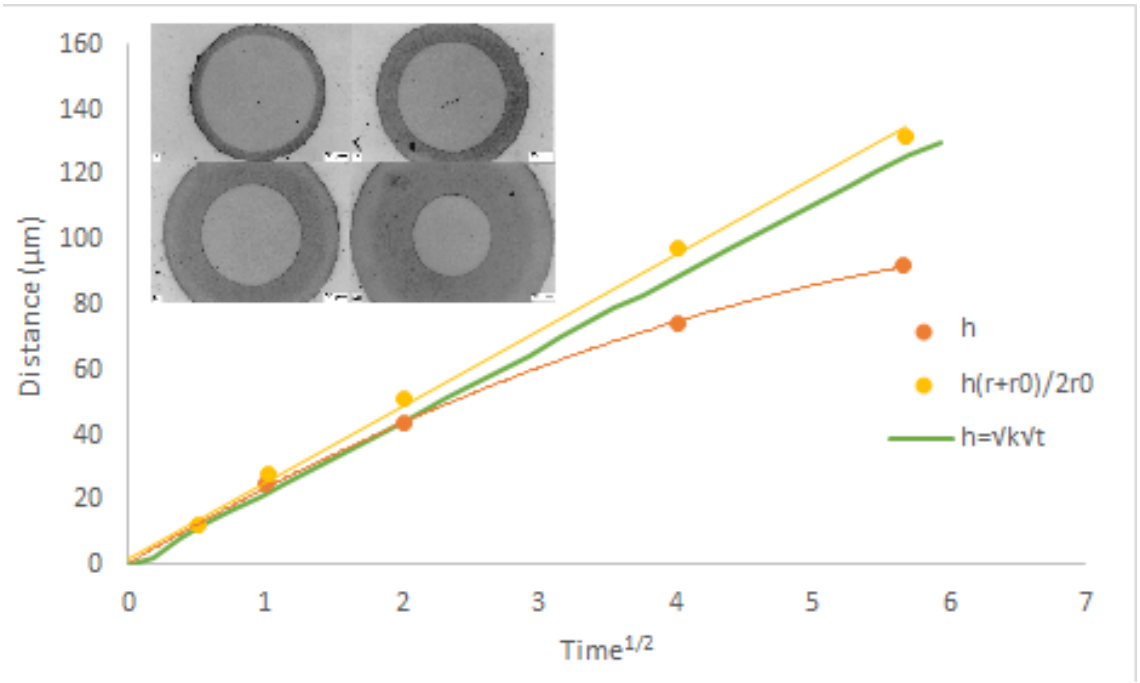

Figure 2.16: *A graph demonstrating the reasoning behind describing the growth rate of the interface in Figure 2.5 [39] as a function of* $\sqrt{time}$ *rather than of* $time$.

dislocation density [6]. In most models, the matrix is assumed to respond to stress as if it were the only phase present, which impairs their accuracy when describing composite behaviour.

It has been shown [27] that the yield strength of MMCs is governed by the size and volume fraction of nanoparticles, the difference in the coefficients of thermal expansion between the matrix and nanoparticles, and the temperature change after processing. The present model indicates that 100 nm is a critical size of nanoparticles to improve the yield strength of MMCs, below which the yield strength increases very strongly with decreasing article size.

Hwang et al [39] proposed a model for the growth of a fibre/matrix interface in a HIP as a function of $\sqrt{time}$.

The growth rate was modelled [39] as $h^2 = kt$ where h = interface thickness. Under the experimental conditions used, $k = 1.4 \times 10^{-13}\text{m}^2\text{s}^{-1}$ at 550°C. The rate constant appeared to be linearly dependent on pressure, based on experimental data, but this was not factored explicitly into the model. Incorporating both radial and planar diffusion gives an expression

$$h\frac{(r+r_0)}{2r_0} = \sqrt{k't} \quad (2.12)$$

$$\text{Since } h = r - r_0, (r - r_0) = (2r_0 + h) \text{ and therefore} \quad (2.13)$$

$$h\frac{2r_0 + h}{2r_0} = \sqrt{k't} \quad (2.14)$$

In which h is interface thickness, r is the instantaneous fibre thickness, r_0 is the initial fibre thickness, t is the elapsed time and k' is the growth rate constant.

These equations are only valid between 15 min and 32 hours of elevated temperatures. After this point, the assumption of an infinite diffusion source also begins to fail, and inward diffusion is significant. The modified parabolic rate constant for the modified equation is $1.7 \times 10^{-13}\text{m}^2\text{s}^{-1}$.

The growth of the interface appeared [39] to slow substantially after reaching 20 μm thickness, but no mechanism for this was proposed. It is plausible that the model loses validity when the assumption of free diffusion becomes less valid, and a thick interfacial layer would cause this. we do not know why.

The residual stresses in a composite can significantly affect the properties of a composite material, particularly in tension. Residual stresses can be calculated using the following formula [6]

$$\sigma_c^P = \left[V_m + V_f\left(\frac{E_f}{E_m}\right)\right]\left(\sigma_m^P \pm \sigma_m^R\right) \quad (2.15)$$

In which σ_m^R is the longitudinal residual stress in the matrix; V_m and V_f are the volume fractions of matrix and fibre and E_m and E_f are the elastic moduli; σ_m^P is the elastic limit of the matrix (in the presence of reinforcement; in tension this is assumed to be the same as for unreinforced matrix); σ_c^P is the elastic limit of the composite.

Homogeneous FEA models do not model shock deformation or damage well [31], and so a "unit cell" was chosen by Olney et al to represent the behaviour of the entire sample. An Eulerian multi-material hydrocode was used to simulate the formation of any force chains, the particle sizes of components, and the morphology and bonding in a composite material. The composite was found both to undergo shear hardening and to experience significant strain localisation.

This suggests [31] that composites, when compared with monolithic material, will experience significant disruption of long-scale relaxation mechanisms, tending to decrease their strength and ductility. They will also disrupt shock fronts because of their variable shock impedances, tending to increase resilience to damage. Which of these will be more significant in a given circumstance must be determined by experiment.

Modelling of a carbon-fibre-reinforced foam sandwich composite [87], with the deformation axis parallel to the aligned fibres, was attempted using a modified form of the Euler buckling equation, which gave agreement to within a factor of two in both quasi-static and slower dynamic strain rates. There was some suggestion [69] that the deformation behaviour under high strain rates might have been governed by dislocation density.

2.8.1 Wetting

Whether a composite manufacturing method is successful will depend on whether the liquid metal will wet the reinforcement. Wetting behaviour is based on the surface energy of the (liquid) melt and (solid) fibres: if producing an interface from these two surfaces is exothermic, wetting will occur, barring a prohibitive activation energy [2].

Looking a the underlying equations of wetting can suggest useful experimental approaches to improving it in practise. Using Young's equation for the contact angle (θ) , and defining the work of adhesion as the energy required to separate the two phases [2]

$$\gamma_{solid/gas} = \gamma_{liquid/gas} \cos(\theta) + \gamma_{solid/liquid} \tag{2.16}$$

$$W_{adhesion} = \gamma_{liquid/gas} (1 + \cos(\theta)) \tag{2.17}$$

in which γ is the surface energy at the solid/gas, liquid/gas and liquid/solid interfaces.

Wetting is achieved when $\theta < 90^\circ$ or when the driving force for wetting exceeds the liquid interfacial energy. The strength of the driving energy depends on the surface tension of the liquid and

the strength of the liquid-solid interface, which in turn are influenced by surface characteristics, interfacial reactions, heat of formation, valence electron concentration, temperature and time.

Some approaches used to implement these principles in practice are detailed below. Increasing surface energy at the solid can be achieved by careful choice of matrix and reinforcement alloys to promote reaction; by increasing the temperature or pressure at the interface; by increasing the time available for wetting to occur; or by increasing the available surface area.

Raising the temperature of the melt improves wetting but also promotes chemical reactions between the matrix and the reinforcement, which can ultimately be detrimental as discussed above.

Applying external pressure by squeeze casting [11] or by using a 'plug' of liquid Al above the compositing region [37] have both been effective approaches. Squeeze casting is more common but is more expensive, particularly at higher pressures.

Increasing the surface area at the interface has most usually been accomplised by acid etching [18]. Improving the surface chemistry has also been accomplished by coating the fibres [4].

The presence of iron or aluminium oxides is detrimental both to wetting and to the resulting interfacial region [2] [4]. Oxide formation can be reduced through surface coatings or by casting in vacuum.

Since liquid Al has a surface tension of around 0.76 N/m, a common problem of manufacture is its failure to infiltrate smaller spaces between fibres. Mechanical agitation of the fibre/liquid mixture can help both to alleviate this problem [13] and to promote the escape of air previously trapped between fibres [10]. both subsonic and ultrasonic agitation have been used.

Decreasing the surface tension of liquid Al has been achieved by the addition of 3% wt Mg, which decreased the surface tension by around 18% to 0.62 N/m [2]. If an alloyant decreases surface tension, it will be drawn to the surface and will act as a pseudo-coating [4]. Adding Zn instead of Mg did improve wetting but also increased the susceptibility of the composite to hot cracking [18], perhaps because the Al-Zn intermetallic compounds freeze at a higher temperature than Al-Mg compounds, or have a less well matched thermal expansion coefficient, increasing the susceptibility of the compound as a whole to thermal expansion mismatches.

2.9 Imaging Methods

2.9.1 Theory of the SEM

Optical microscopy is limited in resolution to around 200nm for practical purposes [88]. For smaller features, an electron microscope is needed. Because electrons have such a short wavelength, their diffraction limit is very small and thus the maximum resolution is very high.

Electrons are absorbed, transmitted or scattered by the atomic nuclei in the specimen surface, in a manner analogous with photons in an optical microscope. Unlike an optical system, in which the full spectral range of visible light is used, the electrons are of very similar wavelengths in order to facilitate analysis of the transmitted and/or scattered electrons, which are captured in separate detectors (as shown in Figure 2.18).

There are two categories of electron microscope: scanning (SEM) and transmission (TEM). The SEM is better at surfaces and the TEM better at internal chemistry and very fine resolution. This project used an SEM because surface features were more interesting than volumetric chemistry.

The SEM uses a system which is fundamentally analogous to an optical system: the electron gun emits electrons, which are collimated into a beam by the Wehnelt cap (together called the anode). Apertures then further narrow the beam into a column, and large EM coils act as lenses and focus the beam onto the sample surface. In practise this is done in two stages, with an adjustable aperture between them, in order to fine-tune the energy of the electron beam as it hits the sample surface. A schematic of the entire system, including detectors, specimen stage and a visible or infra-red camera used for checking that everything is correctly set-up, is shown in Figure 2.17.

These electrons then interact with the electron clouds in the surface atoms on the sample, and are scattered. This interaction produces seven detectable outputs: transmitted electrons, which are not typically measured in an SEM; elastically scattered electrons; inelastically scattered electrons; Auger electrons; x-rays characteristic of the electron structure; Bremsstrahlung radiation; and visible photons. A schematic of this is shown in Figure 2.18.

Auger electrons are a result of the Auger process, in which an incoming electron removes an inner-shell electron from an atom and an outer-shell electron replaces it. This process results in two low-energy electrons (one scattered and one 'knocked off' the nucleus) and an x-ray photon characteristic of the energy gap (from the energy released when the outer shell electron replaces the lost inner electron).

Bremsstrahlung radiation is produced when an atomic nucleus attracts a passing electron but does not capture it. The passing electron is deflected and slowed, and the energy lost in this process is emitted as a photon.

Photons in the visible spectrum are emitted by a combination of the photoelectric effect and some heating of the sample, causing black-body emissions.

Inelastic scattering (secondary electrons) produces low-energy electrons, called secondary electrons, which can be focused onto a detector by adjusting the EM field near it. These electrons are primarily affected by the sample surface, rather than internal features, have a high spatial resolution and a low penetration depth and typically resolve to between 1 nm and 10 nm. They can, however, be "shadowed" by prominent surface features.

Elastic scattering (backscattering) produces higher-energy electrons, is primarily governed by the size (and therefore charge) of the atomic nucleus rather than the electronic structure of the molecule, and is much more likely to have come from atomic layers below the surface. These electrons are more indicative of the chemistry of the sample than its surface shape.

Secondary electrons are detected by placing detectors approximately in line with the centre of the electron beam. These detectors are initially given a positive charge of about +400 V to attract the electron beam, and then contain a scintillator or phosphor screen with a charge of +2000 V. The high positive charge of the scintillator means that electrons will impactwith sufficient energy to cause a bright flash at the impact site. These flashes are then passed through a photomultiplier onto either a video camera or a CCD chip and then to a computer.

Backscattered electrons are detected in a ring around the incident beam, as they are not produced in sufficient quantity to use a single detector. the detector uses either the charged-scintillator system

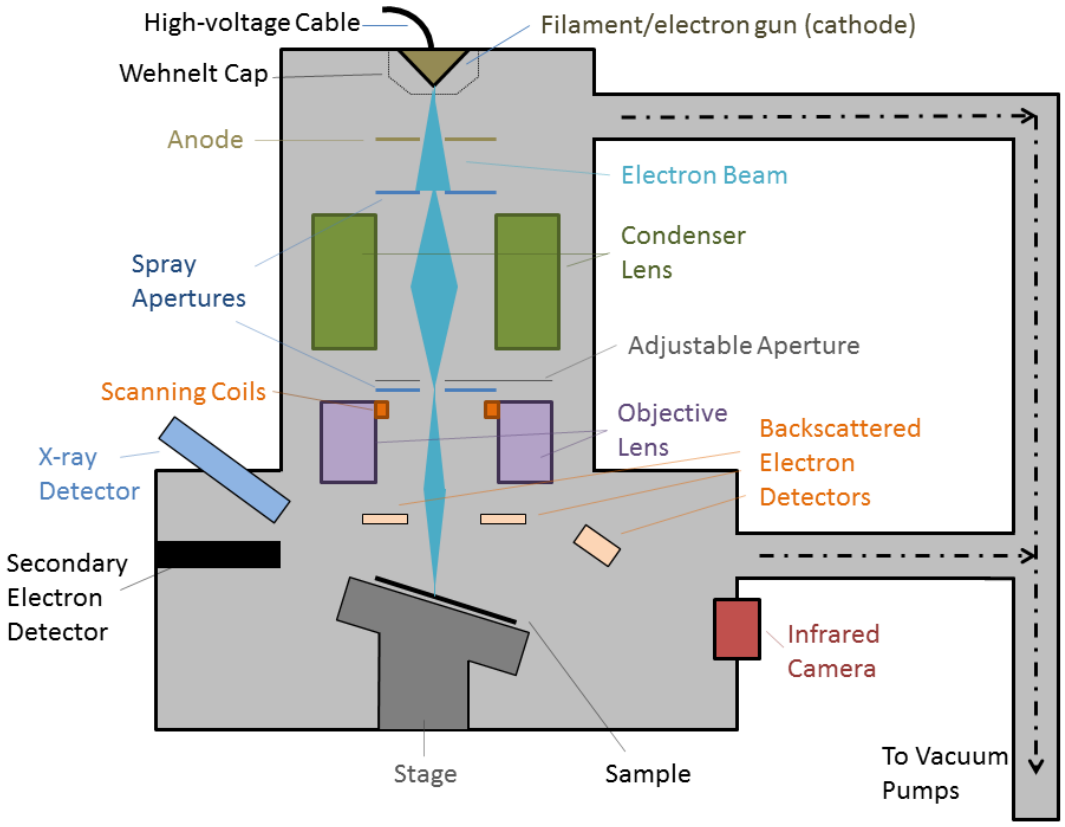

Figure 2.17: *Schematic diagram of a scanning electron microscope, showing the electron gun, focusing system, aperture(s), specimen stage and detectors. The entire column is mounted on a vibration-reducing system, usually consisting of dampeners. When in operation, the system is held under high vacuum. Diagram based on that in [89].*

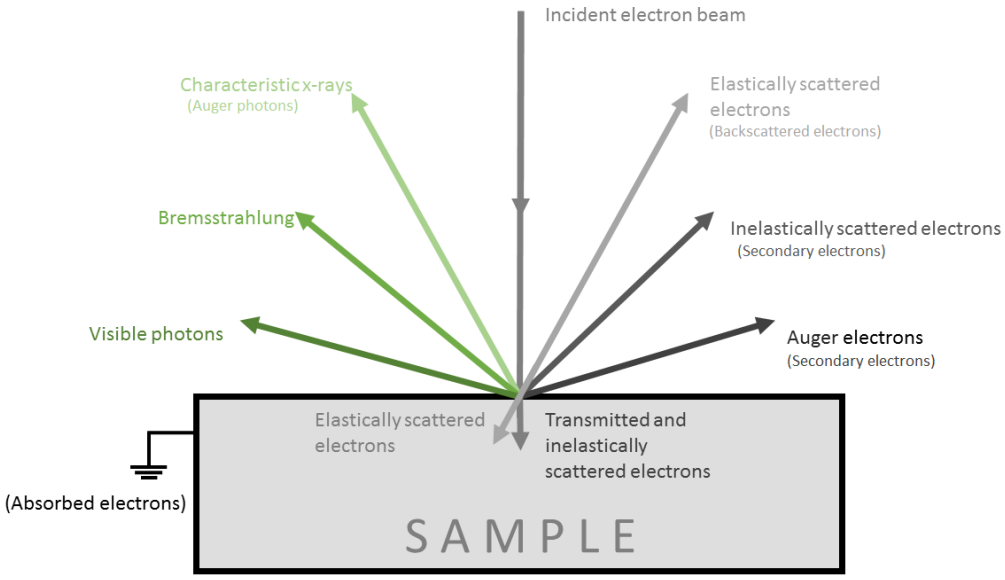

Figure 2.18: *A representation of the electrons and photons detectable in an SEM, with an indication of the interactions which give rise to them. On the right are shown scattered electrons, on the left emitted photons. The angles in the diagram are broadly representative of the angles at which the photons or electrons are expected to emerge, but are not exact. From Zeiss SMT.*

described above or a semiconductor plate designed to produce an electrical signal when impacted by an electron. Because the angle of scatter for this type of electron-nucleus interaction is so strongly dependent upon the size of the atomic nucleus, the number and angle of the electron impacts is indicative of the atomic nuclei encountered by the beam.

Electron backscatter diffraction (EBSD) requires a specialist detector, and gives very detailed information about the crystallographic structure of the sample. If the sample sits at a very high angle (as close as possible to the Bragg angle) to the detector, such that any electrons which react the detector will have been diffracted. The appearance of the bright bands caused by this diffraction will give very precise information about the exact angles of individual crystal grains on the sample surface. Use of EBSD requires an extremely flat and smooth surface, or the noise created by surface roughness will entirely obscure this information.

X-rays and other photons are detected by a simple photo-detector designed for the appropriate wavelength.

The sample stage is typically slightly tilted because this shifts the direction in which scattered electrons tend to be emitted away from the incident beam, making detection significantly easier.

As each point on the sample surface creates a volume of scattered electrons and photons, the detector systems only function for singular points. An image of an area on the surface is created by scanning the electron beam along a small grid, and atomic composition information can be obtained either in a grid or along a single line.

While the secondary electron detector directly creates an image of the sample surface in light, interpretation of backscattered or backscatter-diffracted information requires calculation or comparison with lookup tables. In the SEM system at Brunel, the EDAX Team software does this automatically.

2.9.2 X-Ray Tomography and Quadrat Analysis

Internal imaging of a sample is sometimes possible using X-ray scanning [36]. The transmission of x-rays by a material depends on a combination of nuclear mass and electron density. More massive nuclei will tend to scatter the x-ray photons, and denser electronic clouds present a greater opportunity for absorption. It is therefore possible to determine what material an x-ray beam has passed through based on the detected photons.

It is possible to create a detailed image of an area by using a thin-beam emitter and a ring of detectors around an object and illuminating it [90]. This permits an analysis of the absorption and scattering in that area. If the beam is then revolved around the object in a spiral, a detailed map of the entire object can be reconstructed.

Reconstruction uses a process called filtered back-projection [90]. This converts the photon-rate data into an image. The CT scan data is then presented as a series of vertical "slices", usually (but not always) with the same thickness and horizontal resolution. These 2-D slices are then reassembled into a full 3-D image, which can be visualised either as a skeleton overlay or as artificially constructed slices in another plane. In this project, the image reconstruction was performed using an open-source program called Fiji [91] [92].

In principle, it is possible to make detailed absorption calculations to determine the exact material present, but in most applications the chemical composition is well-known and constituent materials are labelled based on apparent brightness.

In order to assess the fibre distribution within the composite, a procedure called quadrat analysis was performed. Quadrat analysis [93] is a statistical method designed to assess the spatial arrangement of point locations in a defined region.

First, divide the region of interest into a grid and count the number of occurrences of a particular feature in each sector of the grid. If it is assumed that the distribution of points of interest in a plane (such as bright points representing fibres) is random then their incidence will follow a Poisson distribution. One of the features of a Poisson distribution is that its mean value will be the same as the variance (standard deviation squared). Calculating the mean and variance of the occurrence counts per cell and dividing the variance by the mean, it is then possible to say that if the variance/mean is low, then the features are well-dispersed (the ideal value being 1).

It is important to choose the correct grid size for the region under examination: an overly small grid size (with 0 or 1 occurrences per grid sector) will suggest randomness which is not present and an overly large grid size can fail to account for clusters by including an entire cluster in a single grid sector.

2.10 Motivations for HMMC Development

While there has been substantial research into the various routes available for the manufacture of metal matrix composites, there has not been research into the feasibility of using induction heating to manufacture Al-matrix HMMCs. This has been described in Chapter 3.

Similarly, while there has been extensive characterisation of the tensile properties of HMMCs. Some work in this area is described in Chapter 5.

While many models for composite behaviour have been proposed, and there are some candidates

which have been validated against experiment under specific conditions, there is not a satisfactory overall model for the mechanisms by which composites deform and fail.

Chapter 3

Manufacturing

3.1 Design Considerations

The biggest priority in designing a novel manufacturing route for a steel-reinforced HMMC was to reduce the cost of manufacture. To minimise the expense of the anufacturing route whilst ensuring a good-quality material is produced, it is necessary to consider the conditions which must be met for successful composite production: wetting, interface control and physical infiltration of the matrix amongst the fibres.

Both physical infiltration and wetting are more effective at higher temperatures [2]. The fluidity of the matrix alloy will increase as its temperature is raised [18], but sufficiently slowly that it has been considered high fluidity is one of the most important considerations governing the choice of matrix alloy. The final choice of matrix material was made based on the overviews in Table 3.1 and Table 3.2.

While infiltration and wetting are best achieved at high temperatures, if the matrix/fibre combination becomes too hot, reaction occurs as discussed in Section 2.5.1. The longer a composite is left before quenching, the more developed the intermetallic layer will become [40]. The poor properties of Al-Fe composites create a brittle zone in the composite material.

When considering the best method for achieving wetting, many infiltration options for particulates have been discussed. These include [2] the addition of particulates into the liquid stream as the melt is poured into the mould; the addition of particulates into the melt via a vortex introduced by mechanical agitation; the addition of small compressed bricks of reinforcement to the melt, followed by stirring (these bricks are made from cold-pressed mixed aggregates of the base alloy powder and the solid particulates); the forcible dispersion of particulates into the melt by using centrifugal acceleration; physically pushing of the particulates in the melt using rods; and the injection of particulates in the melt while the melt is being bathed with ultrasonic vibration.

Residual stresses will be left in the composite material by the difference in thermal expansion between the matrix and the reinforcement. Careful thermal history management can mitigate these stresses they cannot be eliminated. While they can cause problems, residual compressive stresses have been used to pre-load brittle areas in compression and protect against tensile damage [9].

The manufacturing methods were evaluated by taking several cross-sections of the composite and examining them for macroscopic defects, then polishing them and examining the microstructures produced. A clearly visible interface and no visible voids were the most desirable features.

3.1.1 Matrix Selection

The main selection criteria for the matrix material of a composite are strength, chemistry, density and cost [8]. In the case of an aluminium-matrix composite, surface tension is an important secondary consideration, as this tends to be high for Al alloys [2]. It is also important to consider what impact the reaction between matrix and reinforcement will have on the recyclability of the Al.

An overview of the different classes of alloy in the Aluminium Association (AA) classification standard is given in Table 3.1 and Table 3.1. The wrought alloys discussed provide a wide array of useful properties, but were not chosen because they did not possess the necessary fluidity. Commercially pure aluminium, a 1xxx series material, was used as a comparison material in some of work. The majority of the composite manufacture used A357, comprised of aluminium with 6.5-7.5 %wt Si, 0.45-0.6 %wt Mg, 0.15 %wt Fe, 0.2 %wt Ti and less than 0.1 %wt other elements

Alloy Series	Alloy	Temper	Principal alloyants	Ultimate Tensile Stress (UTS) (MPa)	Yield Strength (MPa)	Elongation at Yield (%)	Hardness (HBW)	Hardening Type
1xxx			$\leq$ 1% other					Work
	1050 A	O	99% Al, $\leq$ 0.5% other	$65 \leq$ UTS ≤ 95	20	20	20	
		H16		$120 \leq$ UTS ≤ 160	100	2	39	
	1080 A	O	99% Al, $\leq$ 0.8% other	$60 \leq$ UTS ≤ 90	15	26	18	
		H16		$110 \leq$ UTS ≤ 150	90	2	36	
2xxx			Cu					Age
	2014	O	4% Cu, Si, Mg	220	140	13	55	
		T6		440	390	7	133	
	2024	O	4% Cu, 1% Mg	220	140	13	55	
		T62		460	400	6	138	
3xxx			Mn, Mg					Work
	3003	O	1% Mn, Cu	$95 \leq$ UTS ≤ 135	35	17	28	
		H16		$170 \leq$ UTS ≤ 210	150	2	54	
	3105	O	0.5% Mn, 0.5% Mg	$100 \leq$ UTS ≤ 155	40	14	29	
		H16		$175 \leq$ UTS ≤ 225	160	2	56	
4xxx			Si					Work
	4007	O	1.5% Si, Mn	$110 \leq$ UTS ≤ 150	45	16	32	
		H12		$140 \leq$ UTS ≤ 180	110	4	44	
	4115	O	2% Si, Mn, Mg, Cu	$100 \leq$ UTS ≤ 145	35	10	$30 \leq H \leq 45$	
		H16		$180 \leq$ UTS ≤ 220	140	1	$55 \leq H \leq 70$	
5xxx			Mg					Work
	5050	O	1.5% Mg, Cu	$130 \leq$ UTS ≤ 170	45	17	36	
		H16		$195 \leq$ UTS ≤ 235	170	2	61	
	5754	O		$190 \leq$ UTS ≤ 240	80	14	52	
				$265 \leq$ UTS ≤ 305	220	3	80	
6xxx			Mg, Si					Age
	6061	O	1% Mg, Si, Cu	150	85	14	40	
		T6		290	240	6	88	
	6082	O	1% Si, Mg, Mn	150	85	14	40	
		T6		310	260	6	94	
7xxx			Zn					Age
	7022	O	5% Zn, 3% Mg, Cu	450	370	8	133	
		T651		450	370	8	133	
	7075	O	5% Zn, 5% Mg, Cu	275	145	10	55	
		T6		525	460	6	160	
8xxx			Others					Both
	8011A	O	Fe, Si (A)	$85 \leq$ UTS ≤ 130	30	21	25	
		H16		$145 \leq U \leq 185$	130	2	47	
LM24/A357		T0	Silicon	300	200	20	90	Age

Table 3.1: *Table outlining the differences in properties between various classes of aluminium alloy. Data taken from a lecture given by the TSC [94] and the relevant international standards [95] [16]. Where properties are quoted as thickness dependent, the thickness used is 0.5-1.5 mm.*

1xxx series	These alloys are typically used for packaging, conducting, lithography and thin barrier films. They possess low strength and high electrical conductivity, are not corrosive and are easy to fabricate.
2xxx series	These are typically used in aerospace, rivets and machine plates. They possess high tensile strength and toughness, and can be machined and welded but are easily corroded and have low ductility.
3xxx series	These are typically used in beverage cans, brazing, building decoration and some cookware. This is primarily due to their extremely good corrosion resistance. They are also easy to draw and has a moderately good tensile strength. However, they are a poor fit with modern processing methods and is being phased out in some applications in favour of 1xxx series.
4xxx series	Typically used as welding filler rods and cladding for a brazing sheet because of their low melting point and high fluidity. These alloys are unsuitable in many cases because of their relatively low tensile strength and poor corrosion resistance.
5xxx series	Typically used as the flat ends of beverage cans, in land and sea vehicles and for structural members. This is due to their excellent corrosion resistance, high impact toughness and good weldability. Their uses are limited by the difficulty in rolling. The Mg concentration is limited by the fact that higher Mg concentrations increase the susceptibility to corrosion, although this can sometimes be overcome by alloy design or temper.
6xxx series	These alloys are used in the frames for windows and doors, ships and automotive closure panels. Their very high fluidity makes them generally useful in applications requiring complex shapes. These alloys also possess good corrosion resistance, good weldability, moderate strength which decreases with temperature and good toughness.
7xxx series	These alloys are used in aerospace, armour and machine plating, principally because of their very high strength and toughness. They also possess some ductility but have very poor corrosion resistance and so are typically coated or painted. Dilute alloys such as AA 7072 are not heat treatable and are typically used as sacrificial protection.
8xxx series	These alloys are very varied in composition and properties, however Al 8006 is used for foils and some aluminium-lithium alloys are used in aerospace.
LM24/A357	This is a cast alloy, valued for its high fluidity and large melting range. It is extensively used in MMC manufacture because its high silicon content prevents damage to the SiC reinforcement particles.

Table 3.2: *Details on the typical uses of Al alloy series, based on their physical properties and approximate cost. Information from [16] and [94].*

[96]. It was chosen for its very high fluidity and large melting range, and its high Si content made it attractive as it could also be used in principle to manufacture SiC-reinforced MMCs for direct comparison.

3.1.2 Fibre Selection and Orientation

A metal matrix composite can be reinforced either with fibres or with particulates. In traditional MMCs [3] [2], particulate ceramics are used and a "large" particle is considered to be anything in excess of 20μm. It would not be possible to manufacture a particulate-reinforced HMMC by any liquid-metal infiltration process with metal particles of this size because there would be a very strong tendency for them to dissolve into the matrix rather than disperse as macroscopic reinforcement.

In general, the solutions to particle agglomeration all promote dissolution of the reinforcement. Adding the significantly higher availability of steel fibres over steel spheroids of similar diameter, therefore, metal fibre reinforcement has been chosen for this work.

SiC particulate reinforcement can be introduced by using an impeller to stir SiC powder into semi-solid aluminium. Stirring into semi-solid Al is preferable because the powder will infiltrate past the high surface tension of molten Al when re-melted if it is sufficiently intermixed with the slush.

SiC reinforcement will stiffen the matrix very significantly but dramatically reduces its fluidity [19]. If both ceramic and metallic reinforcement are desired, the ceramic must be introduced first because it is impossible to mix the powder when metal fibres are present, but it will be more difficult to produce a final composite free of voids.

In MMCs, it was found that the optimum volume fraction for short-fibre reinforcement was around 20% [11]. Fibre preforms can be produced set into wax, which will preserve their orientation [11]. However, these wax preforms require a specialist die which allows the wax to exfiltrate, and increases the difficulty of infiltration.

In general, any deviation of the reinforcement fibre from a regular cylinder will increase the strength of the resulting composite [13] [10]. In addition to an irregular cross-sectional shape, hooked-end or crimped fibres are common.

There are two broad types of steel fibres commonly manufactured for reinforcement of concrete: melt-extracted and crystalline. Amorphous fibres show a higher pull-out load than either type of crystalline fibre, but weaker bonding with the surrounding matrix [63].

Melt-extraction is a process in which molten metal is spun in a perforated crucible held within a water-cooled container. Centrifugal force will push drops of molten metal through the perforations in the crucible, which will solidify in a rough rod-shape on impact with the cool outer container. This causes very rapid cooling, and this creates a near-amorphous microstructure. Melt-extracted fibres both have higher strength than extruded fibres and are more economical to manufacture than the truly amorphous [10].

A random fibre arrangement is likely to lead to the most isotropic properties for the final composite. It is also the easiest to manufacture. While attempts at aligned or planar reinforcement were made (see below) these were not successful.

For smaller, lighter fibres the solidification front was found to push the fibres forward [97]. Sectioned samples were examined for evidence of this, to determine if preforms would be required, but it was not seen when using this method.

An attempt was made to use steel shavings produced as a by-product of machining work, as these would produce a significantly more isotropic composite but were unlikely to entirely dissolve. However, in an experimental trial, the shavings immediately settled to the bottom of the mould and no infiltration into the aluminium was observed.

The choice of fibres for this project was based largely on commercial availability. Available for purchase at the time of writing were the Fibrex HT 25 mm fibres, manufactured by melt extraction, the Dramix 3D 80/30SL, Dramix 3D 80/30BP and Dramix 5D 65/60BG, all manufactured by extrusion and crimping, with basic properties from their respective manufacturers datasheets laid

Fibre Name	Length (mm)	Diameter (mm)	Metal	UTS (MPa)	Elastic Modulus (GPa)
Fibrex HT	25	0.60	Stainless steel	740	95
Dramix 3D 80/30SL	30	0.38	Stainless steel	2000	200
Dramix 3D 80/30BP	30	0.38	High-carbon steel	3070	210
Dramix 5D 65/60BG	60	0.90	Steel	2300	200

Table 3.3: *Table of basic material properties for the fibres used in this project; data taken from datasheets provided by Dynamic-Materials Group Ltd for the Fibretech fibres and N.V. Bekaert S.A. for the Dramix fibres. All aspect ratios are well in excess of the critical value from Equation 3.2*

out in Table 3.3. Both were tested to see whether there was a strong benefit to using one type or the other, which was not found.

In order to successfully reinforce a matrix, fibres must be longer than a critical length governed by [81]

$$l_c = \frac{\sigma_f d}{2\tau_c} \tag{3.1}$$

in which d is the fibre diameter, σ_f is the tensile strength of the fibre and τ_c is the yield strength of the matrix. Substituting in approximate values for the strength of steel and aluminium, we get an aspect ratio of

$$\frac{l_c}{d} = \frac{750}{2\times 150} = 2.5 \tag{3.2}$$

Some of the Dramix 3D fibres and all of the Dramix 5D fibres were supplied glued into small groups. This glue proved to be soluble in water but not in ethanol or acetone, and so fibres were put into a beaker of water and agitated in an ultrasound bath.

Initial experimentation showed that the water would become saturated with glue after approximately two minutes during early removal, and four minutes when the fibres were near clean. Thus

the procedure used was to change the water for fresh every two minutes until four minutes' agitation was needed to cause the water to become cloudy, then to drain the fibres into a sieve, clean them and engage in some mechanical separation, then clean the remaining residue off by repeating the water-and-ultrasound process. The fibres were then dried with an air dryer to prevent corrosion and placed into a sealed plastic bag until needed.

3.2 Gravity Casting

The highest priority for initial sample manufacture was speed of production, with a strong secondary emphasis on simplicity of manufacture. To this end, some time was devoted to developing a gravity-pressured infiltration into a fibre "preform" supported only by the mould walls. This limited the mould diameter to the fibre length (26 mm or 29 mm depending upon the fibre). The "preform" was designed to leave 20 mm at the top of the mould in order to leave a plug of Al, the weight of which would help to force infiltration as described by Mitzumoto et al [37]. A summary of the casting attempts in the 20 mm mould is in Table 3.4.

Initial tests used a 32 mm diameter mould of 70 mm height with a short taper at the base. It was determined that the mould required preheating to 550°C to obtain a sample which was tolerably free of voids. A second mould with 20 mm diameter and 110 mm height without a tapered base was trialled, and was found to produce better specimens, and so it was used for most of the later work.

In practise, a preheat temperature of 560°C was typically used to prevent irregularities in the thermostat from causing any problems. The casting temperature of the matrix alloy was 760°C for LM0, 660°C for A357 and 980°C for the Fe-Al alloy. These melt temperatures were chosen to be well above the liquidus temperature of the alloy.

The mould and fibres were preheated in a free-standing heater unit, and the melt was then poured into the fibres without removing the mould from the heater unit. This was done because removing the mould and setting it in the open air was found to cause the fibres to settle towards the bottom of

Number of Trials	Melt Temperature (°C)	Preform/mould Temperature (°C)	Outcome	Notes
20	760	560	Success	
1	660	500	Failure	
1	700	500	Failure	
1	700	550	Failure	
3	760	560	Failure	Aligned (uncrushed)
3	760	560	Partial Failure	Aligned (crushed preform)
1	760	660	Failure	Melt flowed out
N/A	760	560	Success	Single-Fibre Embedding

Table 3.4: *Specification of the casting trials performed with the induction furnace with laboratory conditions*

the mould. During pouring, the heater was deactivated in order to prevent damage to the element should any splashing of the melt occur.

Infiltrating the melt into the fibres at such a high temperature whilst inside a heating unit caused initial solidification to be comparatively slow. This slow solidification, while generally undesirable due to its promotion of large crystal structures and thick alloy-matrix interface zone, was necessary in order to permit interface-surface formation between the matrix and the reinforcement. This formation was primarily restricted by the high surface tension of liquid Al alloys, which prevented the matrix from flowing into small voids between fibres, and somewhat impeded by its freeze-shrinkage.

The solidification time was limited to minutes by cold-water quenching of the composite as quickly as possible after the aluminium had solidified. This was done to maximise the consistency between specimens.

In addition to the near-isotropic fibre arrangement described above, composites were produced with partially- and fully-aligned fibres. The composite with partially-aligned fibres was produced by using a mould with a diameter slightly shorter than the length of the fibres, such that they could not sit fully horizontally. Otherwise, production followed the procedure detailed above.

Composites with fully-aligned fibres were produced by creating a full, robust preform which could be inserted into the mould prior to preheating. This preform was produced by manually aligning the fibres on a doubled-over sheet of 5 μm Al foil, affixing them to the foil with spray-adhesive and rolling the foil to create a cylindrical preform. This cylinder was manually compressed to remove as much air as possible before insertion into the mould. It was expected that the adhesive would be entirely decomposed by pre-heating, as the decomposition temperature of a similar organic resin was 250°C [82]. The breakdown was confirmed when in later trials any residual organic adhesive smoked or flamed on contact with molten Al.

This procedure was unsuccessful. After the first attempt, using four layers of foil between each fibre to keep them separate, showed that air was trapped in significant quantities around the fibres, mechanical squeezing of the preform was performed and the foil thickness was reduced to two layers. Attempted infiltration of the squeezed preforms showed that when the foil layers had been preheated to 560°C, liquid Al introduced at 660°C did not penetrate past the outer layers of the foil. However, at this temperature the foil had already softened noticeably and so it would not be able to remain a useful preform at higher preheat temperatures. It is hypothesised that squeeze casting would be necessary to produce a viable composite using this method. Sections of failed attempts are shown in Figure 3.1.

Production of non-cylindrical samples was attempted by several unsuccessful means. A book mould was found to have an aperture which was too narrow to permit infiltration: the liquid A357 flowed over the fibres instead of into them.

A heated preform of fibres encased in foil was placed into a large, open rectangular "boat" mould, and A357 at 650°C was poured onto it. The preform, which began to float due to the volume of trapped air, was then physically pushed under the surface of the A357, but by this point the A357 had cooled significantly and lost fluidity. Stirring the mixture was not possible as it would have destroyed the fibre arrangement in the preform and caused the fibres to settle at the bottom of the mould as had been observed in the tool steel experiment.

Squeeze casting was also considered as an alternative process in order to overcome the problems with voids which were being encountered. While a machine capable of performing squeeze casts

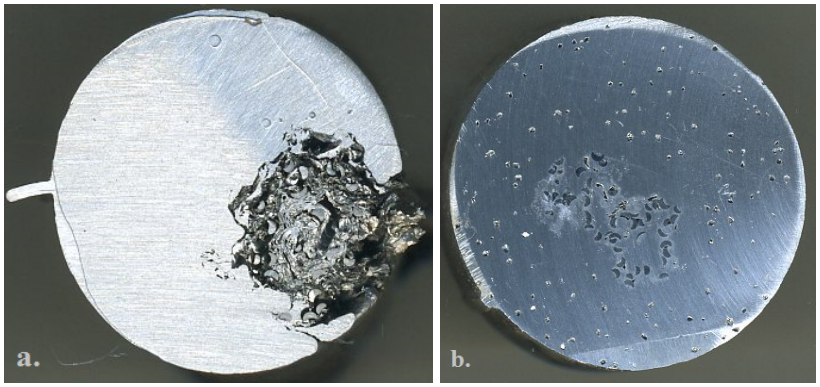

Figure 3.1: *Sections of the attempts at producing a composite with vertically aligned fibres in the 20 mm mould. a. shows the first attempt, with thicker foil layers and no squeezing. b. shows the second, with thinner foil layers and excess air removed. This sample has significantly irregular fibre distribution caused by the squeezing method and still has poor infiltration of A357 among the fibres.*

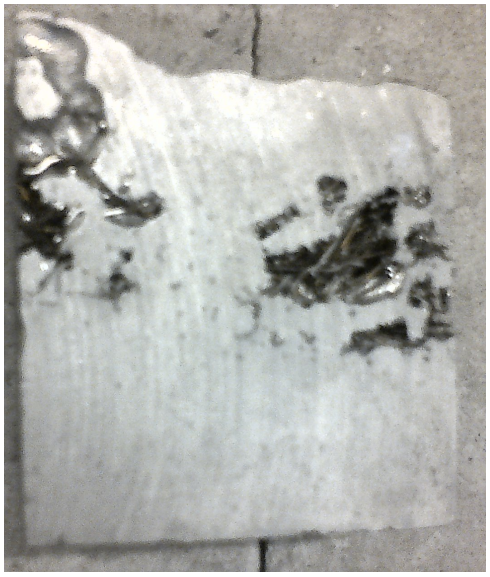

Figure 3.2: *An attempt at producing a cuboidal specimen by pouring 650°C liquid A357 onto a heated fibre preform in a large, open mould with a rectangular cross-section. Very large voids are visible in the cross-section, which are the result of trapped air which caused the preform to float and required it to be manually held under the surface of the Al. The method was not pursued.*

was found, it required a specific heating unit and could only apply uniaxial pressure, and is not a cost-effective manufacturing process. None of these methods were further pursued as the initial induction furnace trials were very successful.

3.2.1 Imaging and Analysis

Sample Preparation

In order to study the microstrctures of the cast samples, it was first necessary to polish them. Initial polishing was done on a ATM Saphir 520 polishing machine with Rubin 500 automatic polishing heads, using SiC abrasive papers and lubricant. The finest grades of paper were hand-polished on the same machine to prevent damage to the surface.

Water was used to lubricate the SiC papers were from grades of P120 (coarsest), P320, P800, and P1200. Ethanol was used for grades P2500 and P4000. Final polishing used OPS (Oxide Polishing Suspension) non-dry colloidal silica suspension on the same machine and a Streuers MD Nap polishing cloth. The machine was run at 140 rpm throughout.

For samples with LM0 as the base alloy, P4000 paper could not be used as the very fine SiC particles became embedded in the metal surface. In this case, that polishing step was omitted. Similarly, if the sample showed signs of SiC damage then the polishing speed was decreased to 90 rpm. The duration of polishing was varied between 20 seconds and 2 minutes, until the surface appeared to be free from defects introduced in previous polishing stages.

Selected samples were then electropolished in order to show the crystal grains very clearly and study them. Of the available etchant chemicals, dilute Marble's reagent (a mixture of $CuSO_4$ and HCl) etches the fibres and preserves the interface and reaction zone; 0.5% HF etches the matrix but attacks the interface [18]; and Barker's reagent (HBF4) is a standard etchant for aluminium alloys [3], though it will strongly attack any ferrous phases present. Barker's reagent was chosen because the interface could be viewed sufficiently well with the SEM system, it was readily available and it is significantly safer than HF.

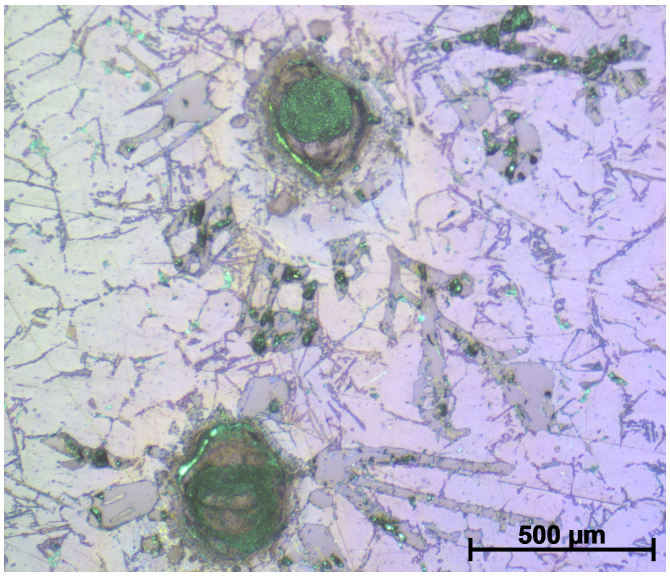

Figure 3.3: *A trial of a very brief anodisation was made, in which a sample was anodised for only 5 seconds in an attempt to preserve the iron features in the matrix. The iron-rich features were more strongly preserved, but the aluminium was not sufficiently anodised and no new features were revealed.*

Samples were connected to the negative terminal of a power supply set to 20 V and then immersed in a metal container ontaining the Barker's reagent and connected to the positive terminal. The power supply was current-limited to 3 V.

Samples were immersed in the acid for 15-25 seconds and then removed and placed immediately into distilled water to neutralise any ongoing reaction, then dried and examined. Samples which showed insufficient reaction were re-immersed for a further 10 seconds.

Samples treated in this way had any iron inclusions entirely corroded by the acid. One sample was immersed for only 5 seconds in order to attempt to see both Al crystals and the steel areas. The result, shown in Figure3.3, was to preserve some of the features of the iron but no grain structure information was visible. This confirmed that electropolishing did not reveal any interfacial features not seen on the microscope and SEM images.

In order to polish samples which were very small, and to permit the use of an automatic polishing head, some samples were mounted in resin using a ATM OPAL 410 press at 280 bar, preheated to

180°C and held at this temperature for one minute before being allowed to cool to room temperature over three minutes.

Some very small samples were mounted and then sectioned and re-mounted, in order to enable a good grip in the cutting machine to expose a specific location of interest, such as the fracture surface of a tensile bar.

3.2.2 Microscopy and Visualisation

It is apparent from the microstructural pictures that the very large dendrites typically seen in slowly-cooled Al are not present in the composite samples. This is thought to be because the fibres act as crystal nucleation sites, at a far higher density than the nucleation sites seen in unreinforced alloy. Figures 3.5 to 3.11 are a series of microscope and electron microscope images of sectioned gravity-cast samples showing porosity, shrinkage cracks, dendrite growth, intermetallic phases and the fibre-matrix interface.

Early gravity-cast samples in LM0 were not well-produced. Microscope images showed that they contained voids of at least 600 μm, and very little intermetallic interfacemore than one fibre showed no detectable interface on most or all of the interfacial surface. Where intermetallic formation had occurred, it covered around 200 μm of circumference and extended approximately 100 μm from the fibre edge.

Later samples, produced with A357 and which had undergone tensile testing, showed more consistent interface formation, around most or all of the fibre circumference where it formed, as seen in figure3.6, but still of very small thickness. They also show more shrinkage damage at the fibre edges.

The images in Figure 3.7 and Figure 3.8 are of a post-test tensile sample. The fact that in Figure 3.8 the “open” end of the dendrites is toward the matrix and the fibre edge remains distinct shows that dendritic growth was primarily radially outward into the matrix, rather than inward into the fibre. The crack running along the outside of the dendrite region is also in agreement with Mandal et al.

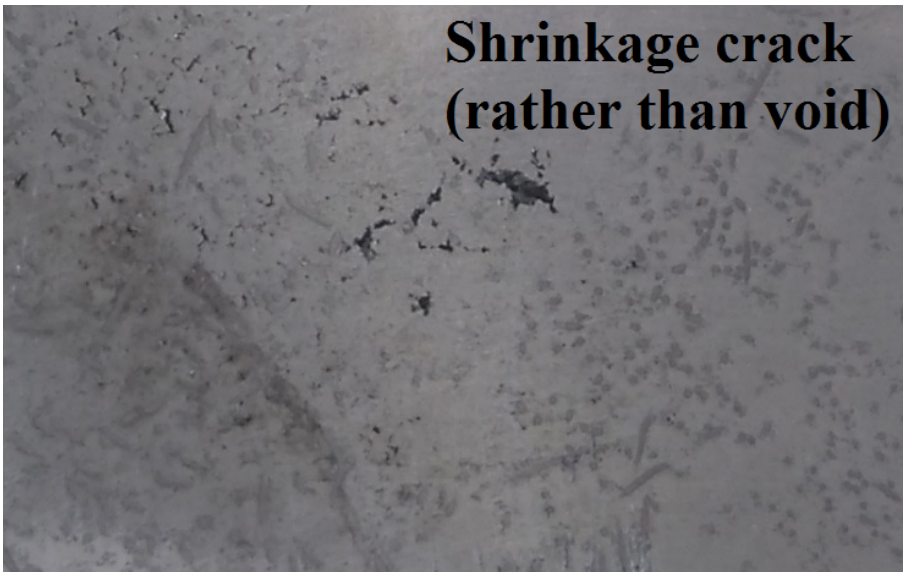

Figure 3.4: *Shrinkage cracks were often present in the top third and centre of the crucible after it had been removed from the induction furnace. The slow cooling of the samples could not be prevented, but cooling time was minimised by removing the crucible to a cool area after casting rather than permitting it to remain in the furnace.*

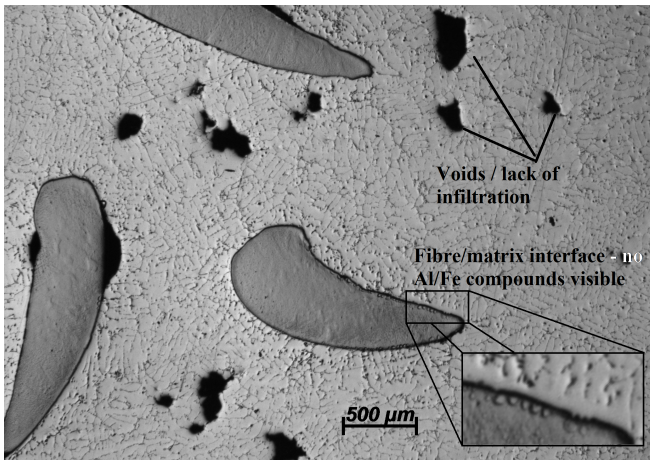

Figure 3.5: *Image of the composite as prepared, showing the many voids and lack of reaction between the fibres and the matrix.*

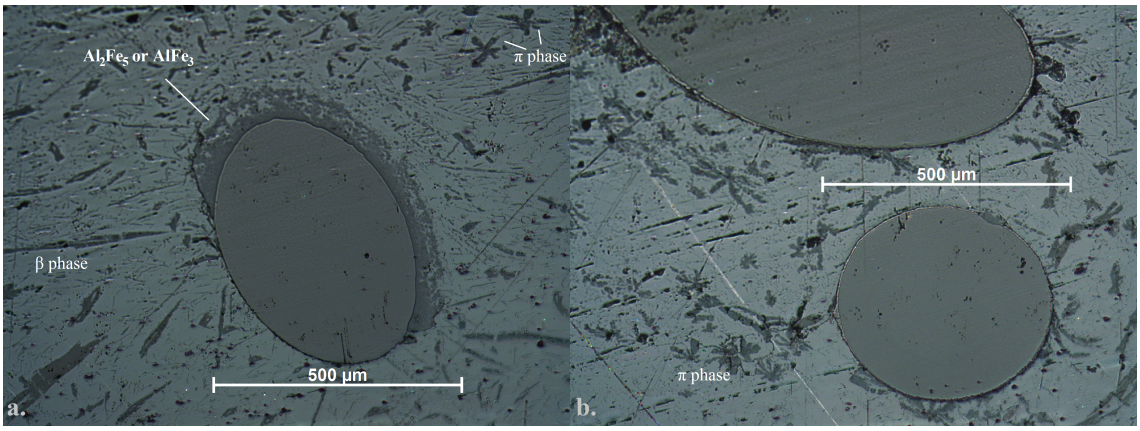

Figure 3.6: *Images of a typical gravity-cast sample. The interfacial layer between fibre and matrix is small or absent, and intermetallic compounds are primarily star-shaped π-phase or more commonly β-phase needle-shaped inclusions, which are deleterious to the properties of the final composite.*

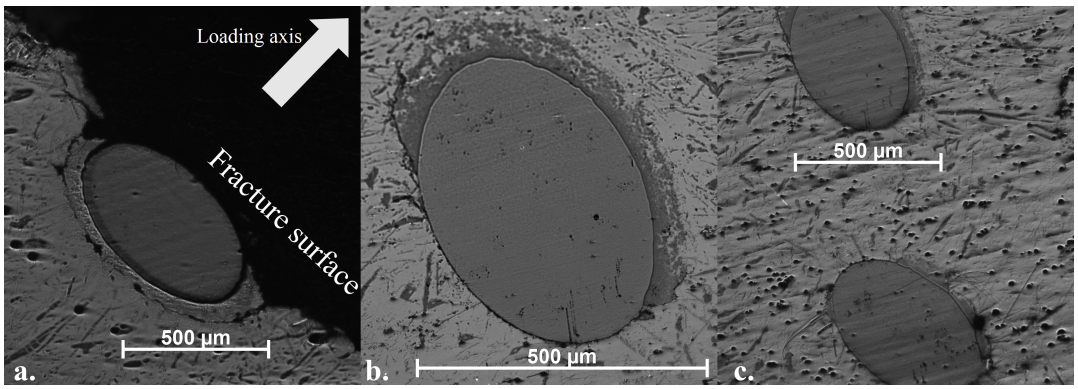

Figure 3.7: *Micrograph images of the composite from Figure 3.6 showing fibres and interfacial regions at (a), close to (b) and more than 10 mm away from (c) the fracture surface. There is no visible damage to or deformation of the interfacial region at any of the three sites, and the crack in (a) is entirely outside the visible interface.*

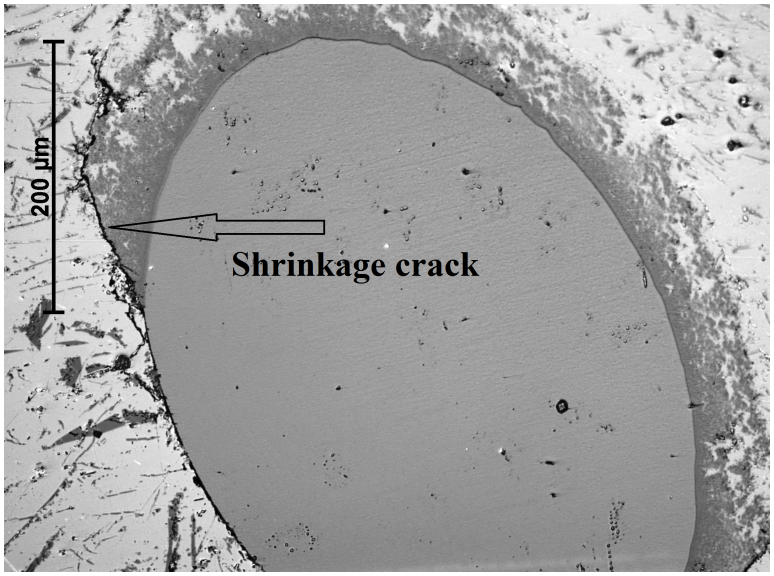

Figure 3.8: *Detailed picture of the dendrite formation from Figure 3.6 at some distance from the fracture surface, showing a crack running around the outside of the dendrite region.*

[7], who suggested that the fibre-matrix interface region is brittle, though it also suggests that the bond strength along the inside of this region is a stronger factor than the brittleness.

Figure 3.7, which shows the same specimen at different distances from the fracture surface, shows the variability of interfacial growth at different regions in the composite. Figure 4.12a and Figure 4.12b both show intermetallic compounds which have formed around much of the fibre circumference and Figure 3.7c shows fibres with no visible interfacial region. Given the shape of the crack in Figure 3.7b, it is suspected to have occurred during cooling rather than during tensile loading.

The variation in fibre state through the body of deformed samples means that damage was entirely localised at the point of failure. This is in agreement with the hypothesis that the fibre-matrix interface presents a point of critical and catastrophic weakness in the gravity-cast samples.

In Figure 3.8, it can be seen that the fibre surface is a nucleation zone, since dendrites can be seen radiating outward from them. This is probably because of the significant surface roughness, and possibly also because the reaction products will tend to have a higher melting temperature than the Al alloy. That the dendrites are relatively long (hundreds of micrometers) suggests that the cooling rate was slow, as expected from the literature.

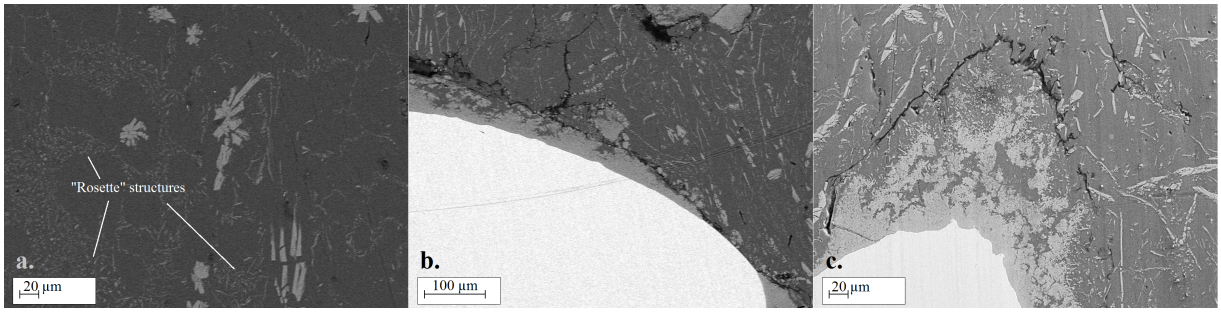

Figure 3.9: *Pictures showing a sample of composite both close to and far from the fibre inclusion. The dendrite growth around the fibre can be seen, as can what appear to be iron inclusions. In the matrix body (left), the 'rosette' structure also found by [45] can be found suggesting that the matrix has experienced shear during the onset of solidification.*

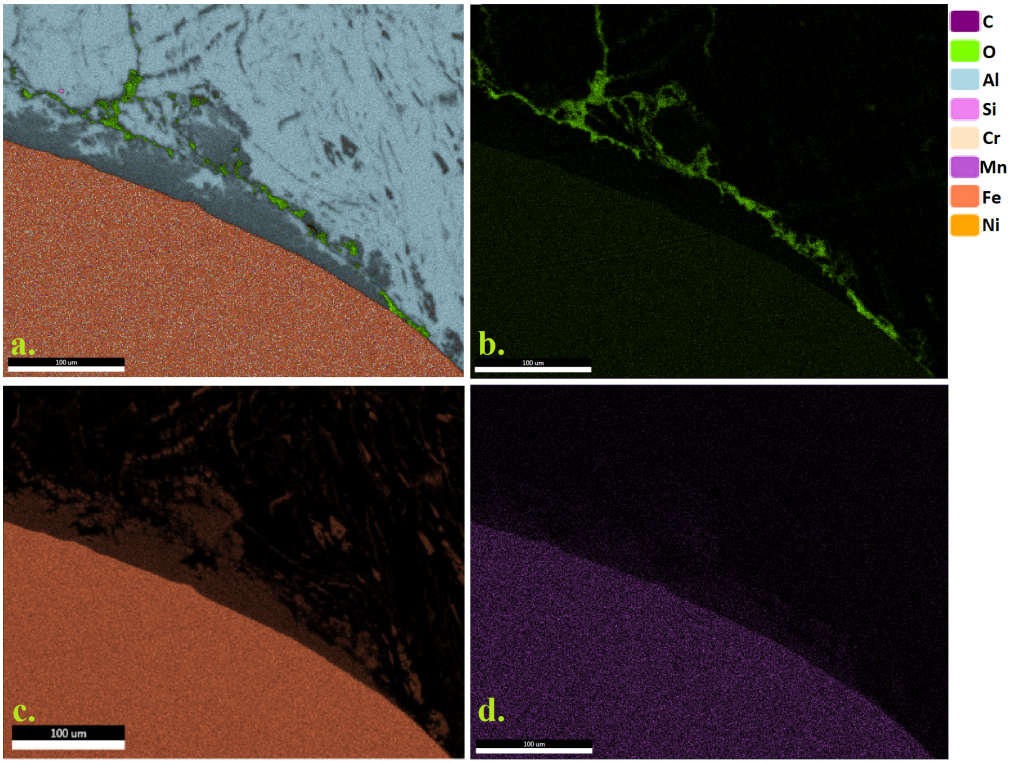

Figure 3.10: *The different phases of intermetallic compounds formed at the fibre-matrix interface can be seen. Grey shows aluminium, green is oxygen, orange is iron and purple is manganese. This is the E2P setting in the TEAM software. The SEM was set at 700 kV, 12 frames, 200µs/frame, 512x400 pixels. The oxide layer is thought to have originated in the melt.*

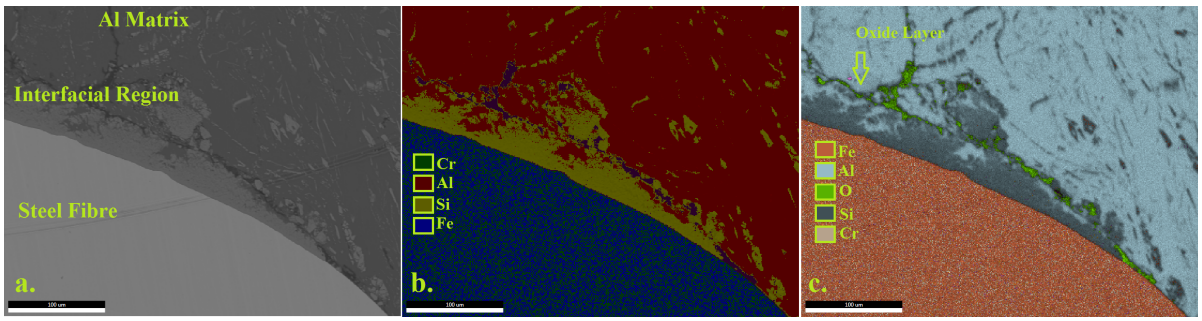

Figure 3.11: *Demonstration of the types of data output available from the EDAX software. (a) a simple picture, showing surface detail. Centre is the phase-to-element plot, in which colours denote specific elements (potential elements are chosen by the user). (b) the element-to-phase plot, in which colours denote different molecular structures, usually phases or compounds such as austenitic/ferritic steel and Al2Fe5 or* $AlFe_3$

The theory of the scanning electron microscope is described in Section 2.9.1 above. At a significant distance (more than 200 μm) from any fibre, Fe-Al and Fe-Al-Si intermetallic compounds can be found, primarily either as π-phase inclusions or segregated to the grain boundaries. The EDAX (Energy Dispersive Analysis X-ray) estimate is 4% iron by elemental composition, including the $FeAl_3$. This suggested that there might not be a significant difference in performance between composites made with factory A357 and recycled A357 with a significant iron content, which was investigated in Section 4.2.

At the fibre edge, there is evidence that the fibre surface reacted to cause an interface to grow outwards into the matrix. The oxide layer shown in green in Figure 3.10 sits outside the intermetallic layer in the matrix, not at or inside the fibre surface. The oxide layer is thought to originate from oxide layer which forms on the molten matrix before and during pouring. The Cr, Mn and Ni present in the fibre alloy do not appear to have reacted with the matrix.

While the oxide layer on the fibres may have inhibited wetting [2], it did not prevent it. The voids present in the composite are likely caused by the high surface tension of molten Al rather than a lack of wetting at the fibre itself.

Quantitative analysis suggests that two phases are being formed between fibres and matrix, with

the more common phase containing Al and Fe at a 6:1 ratio and the other having Al and Fe at a 3:1 ratio. Given that the ratios found are an average across around 50 micrometers' depth, this suggests FeAl3 and $FeAl_3Si$ for the whiskers.

3.3 Induction Furnace Manufacturing

Initial experimentation with using a MelTech medium-frequency induction furnace to ensure infiltration of Al into a fibre network showed good infiltration, some shrinkage porosity and low gas porosity but moderate dissolution of fibres into the matrix.

A357 was heated in the induction crucible at 2.4 kHz, between 18 and 25 kW and between 1000 and 1125 V. The current was carefully controlled to ensure that the metal did not become dangerously heated or "spit". 10% weight of Dramix fibres were then added to the melt at $700\circ$ C under minimum current and the mix was mechanically stirred using a steel rod coated with boron nitride lubricating paint. This cooled the mixture, often to a semi-solid state. The current in the induction furnace was then briefly increased and the mixture brought up to $650\circ$ C over approximately two minutes before the furnace was switched off and the composite was allowed to cool over several hours in the crucible. An attempt to pour the mixture into a mould confirmed that the fibres remained stuck in the crucible.

A cylindrical crucible was used in order to ensure that the composite could be easily removed after solidification. 10% weight was chosen because at that density of fibre the matrix volume was reasonably well-infiltrated but not over-packed. When tests were made at 5% weight, large sections of matrix were not reinforced. When tests were made as 12% weight, voids were found which were similar in character to those from the gravity cast samples. A comparison of these is shown in Figure 3.12. Specifics of the trials performed are detailed in TableCastDeets-IF.

Casting times were initially chosen to be as short as possible as dissolution of the fibres into the matrix was not desirable. After initial trials showed promise, the ideal casting time was investigated. After immersion and brief mechanical stirring, the induction current was re-activated and a timer was started. When the temperature in the crucible reached 655°C, the current was dropped

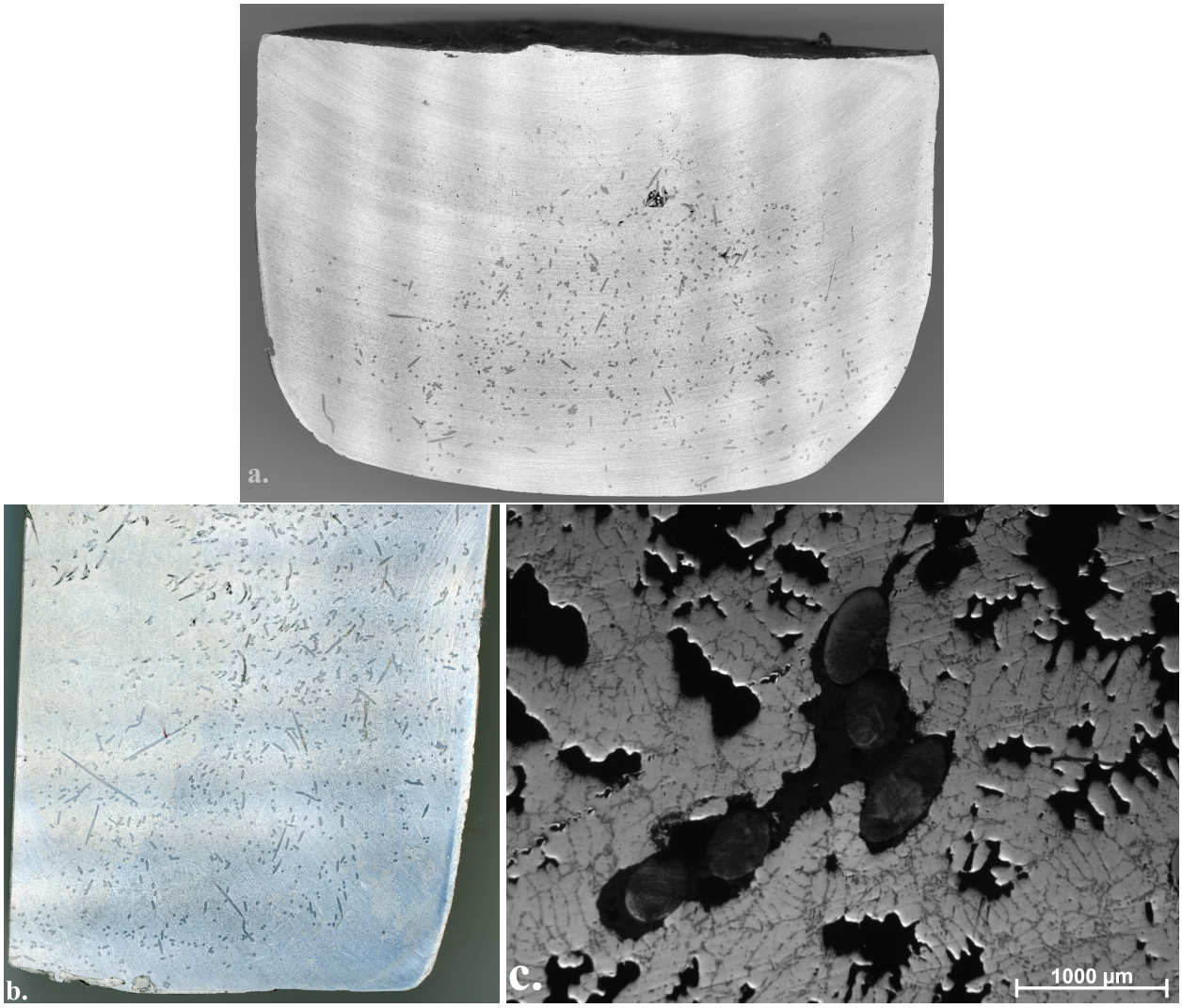

Figure 3.12: *Photographs of three different reinforcement fractions. 5% weight (a.) shows poor mixing through the sample and collection if the fibres at the bottom of the crucible; 12% weight (c.) shows acceptable fibre distribution but poor matrix infiltration. 10% weight (b.) is an acceptable compromise. Some fibres have separated from the composite surface, but this was caused during the polishing process.*

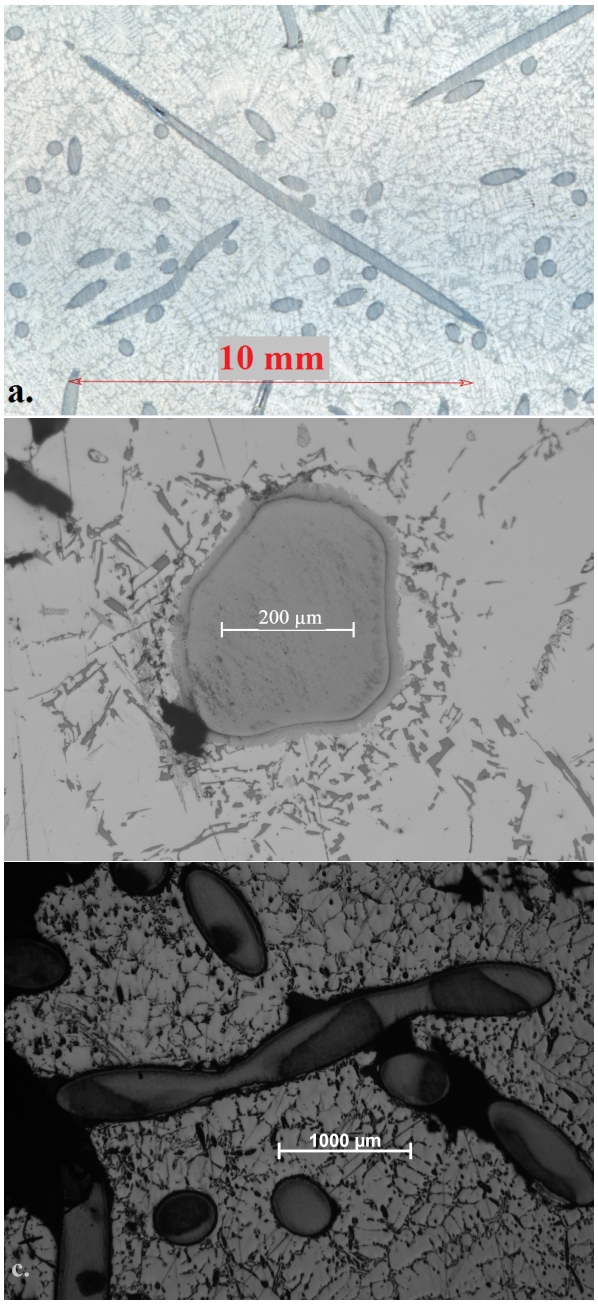

Figure 3.13: *Otherwise-identical samples which had been left for differing amounts of time at* $650°C$ *in the induction furnace. (a) a sample prepared without additional time, for a total of two minutes under induction current after fibre addition. (b) is a sample left for 3 minutes at temperature, for a total of five minutes under induction current. (c) is a sample left for 8 minutes at temperature, for a total of ten minutes under induction current. It can be seen that after 2 minutes, almost no thermal deformation is found in the steel fibres, whereas after 12 minutes it has become quite pronounced. There is no observed change in the fibre diameter for the deformed fibres.*

Number of Trials	Time Under Current (s)	Peak Temperature (°C)	Temperature at which Fibres Added (°C)	Notes
2	Not recorded	850	700	
2	Not recorded	850	700	
1	57	850	700	
4	130	850	700	
1	120	850	700	
1	300	850	700	
1	600	700	700	
1	Not recorded	700	700	Additional SiC in Matrix

Table 3.5: *Enumeration of the casting trials performed with the induction furnace with laboratory conditions*

to its minimum setting. When the temperature dropped to 645°C the current was raised again to maintain an even, high temperature in the crucible. When the timer reached 5 or 10 minutes, the current was deactivated and the crucible was removed from the furnace.

Examining the microstructure of these specimens, shown in Figure 3.12, it can be seen that extended time under current causes the steel fires to deform. Given that their relatively high electrical resistivity will cause them to be more strongly heated by the induction current than the A357 matrix, this is thought to be a result of their approaching their melting temperature. After ten minutes under current, the deformation had become both significant and widespread, and so samples were produced with only 2 minutes under current between fibre addition and removal from the furnace. Using the 80/30 BP fibres, this was significantly less of an issue than with the 80/30 SL fibres because the 8/30 SL fibres showed a much stronger tendency to react with the matrix alloy, which would be exacerbated by an extended period at high temperatures.

Initially, 3D-80/30-SL fibres were used, as had been the case for most of the initial testing. After these became temporarily unavailable, RC-80/30-BP fibres were substituted. The RC-80/30-BP fibres were very much less reactive with the aluminium matrix than the 3D-80/30-SL fibres.

The RC-80/30-BP fibres were a high-carbon steel rather than a stainless steel which will account for this. The precise steels used in the fibres could not be determined using the available equipment.

The RC-80/30-BP fibres were also supplied in glued bundles, which had to be manually separated and cleaned as the organic glue was flammable. Even after washing and separation, the fibres were more prone to agglomeration than the 3D-80/30-SL fibres, and so they required a slightly longer stirring time to prevent exclusion voids from being left in the matrix.

HMMC reinforced with SiC was also manufactured to assess its properties. The addition of SiC made the A357 very much less fluid, and so the manufacturing conditions used for A357 alone left a composite with voids and bubbles. If more time had been available, further attempts involving a lower volume fraction of iron, higher furnace temperatures and a longer stirring period would have been made.

The SiC was introduced to the Al alloy by first melting the alloy in an induction furnace, then cooling it to a semi-solid state, adding the pre-measured SiC powder in foil packets and stirring the mixer with an impeller until it became too solid. The mixture was then reheated and impelled as soon as it reached the semi-solid state for at least 5 minutes. It was then cast and allowed to cool. The final SiC content was 15% vol.

In Section 3.2, it was noted that a significant quantity of iron dissolved from the fibres into the matrix. It was therefore hypothesised that a composite manufactured from aluminium with a high iron content would not have dramatically worse strength and ductility. In order to test this, LM0 with 4% wt iron was manufactured by dissolving alloy chips of 45% wt iron into molten LM0 at at 850°C and stirring every 15 minutes until the iron-rich chips appeared to have gone, approximately 4 hours. 4% wt was chosen as it is substantially above the threshold at which iron becomes detrimental to the alloy properties.

The resulting alloy was cooled and checked for undissolved chips, then re-melted in the induction furnace and fibres were introduced using the methods described above. Samples were then machined from this for tensile testing.

Figure 3.14: *Smoothed cross-section of the induction-cast composite showing the distribution of fibres and shrinkage pores from the centre to the edge of the crucible.*

3.3.1 Imaging and Analysis

The induction-cast samples showed, in addition to the thicker interface visible under ordinary microscopy, the Al-Fe-Si compounds formed all three of their primary crystal forms: large polyhedral crystals, thin platelets and "Chinese script" crystals. This indicates the presence of α-Al-Fe-Si (polyhedral) and Al-Fe-Si-Cr compounds ("Chinese script").

The thin, platelet crystals are the primary contributors to brittleness by increasing shrinkage porosity and impeding large-scale stress relaxation. It is worth noting that the majority of shrinkage pores seem to have formed in or adjacent to the Fe-Al-X compounds [98].

Chromium tends to promote the formation of the other crystal morphologies, such as the star-shaped π phase, thought to be $Al_{12}(Fe, Mn, Cr)_3Si_2$ [98], which is likely to have been beneficial to the overall properties.

The fibre distribution does not show any obvious aggregation, suggesting that a rigid preform structure was not needed and that the fibres were benefiting form the magnetic stirring of the induction furnace.

Pictures of polished sections show that there is good infiltration but noticeable shrinkage porosity. Shrinkage pores are reduced in size compared to those found in the matrix alloy prepared under

the same conditions. This is thought to be because the fibres nucleate solidification, which would similarly explain the small crystal size from such a slowly cooled ingot (see below).

Electron microscope images of the composite show an absence of gap between the steel fibres and the matrix, but also show that intermetallic compounds form only on the surface of the 3D-SL fibres and not the RC-BG fibres, believed to be because the two fibres have a different chemical composition.

Intermetallic ($FeAl_3$) crystals formed at or near the fibre surface tend to be approximately hexagonal in shape, as shown in Figure 3.15. At some distance from the fibre surface, both the α-phase (iron-aluminium with some silicon) and β-phase (iron-aluminium-silicon) intermetallic inclusions can be seen, as well as some π-phase. The α-phase inclusions were not found at all in the gravity-cast specimens, and are thought to be beneficial to the strength of the composite [98].

Shrinkage pores, where they appear, seem to be mostly in the Fe-Al crystals which have dispersed into the matrix and somewhat near the fibre surfaces, with very few appearing in the matrix itself.

Comparing this with the gravity cast specimens, different intermetallic compounds are forming and there seems to be a decrease in beta-phase inclusions. The interface shape is not entirely dissimilar to that found by Pattnaik et al [6] shown in Figure 2.2, but is very much thinner. This is likely due to the lack of any external pressure on the mixture during formation, and to the relatively short exposure times.

Comparing the interface thicknesses with the model discussed in Section 2.8, putting values into Equation 2.14

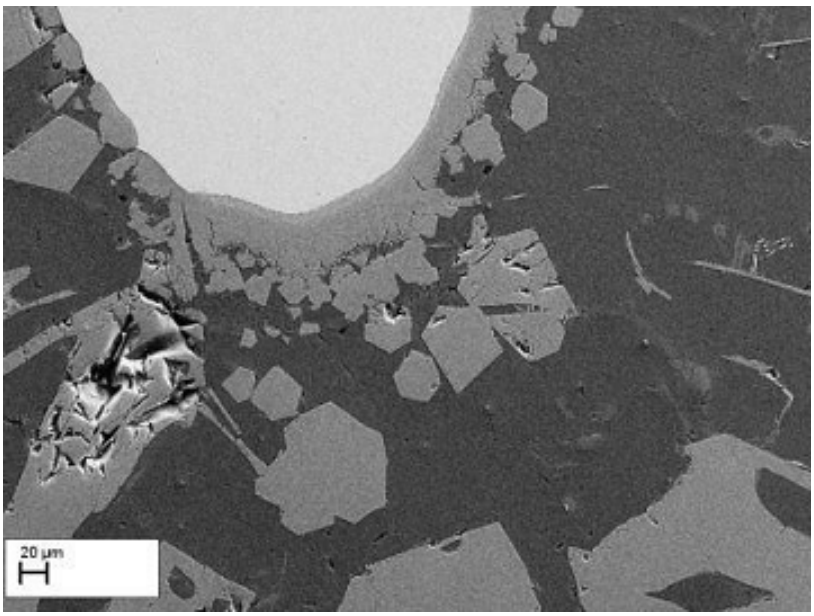

Figure 3.15: *SEM picture of the interface between a 3D-SL fibre and the A357 msatrix. Two regions can be seen in the interface, and approximately hexagonal crystals can be seen in the matrix region. Some shrinkage pores can also be seen. The change in fibre diameter was not measured.*

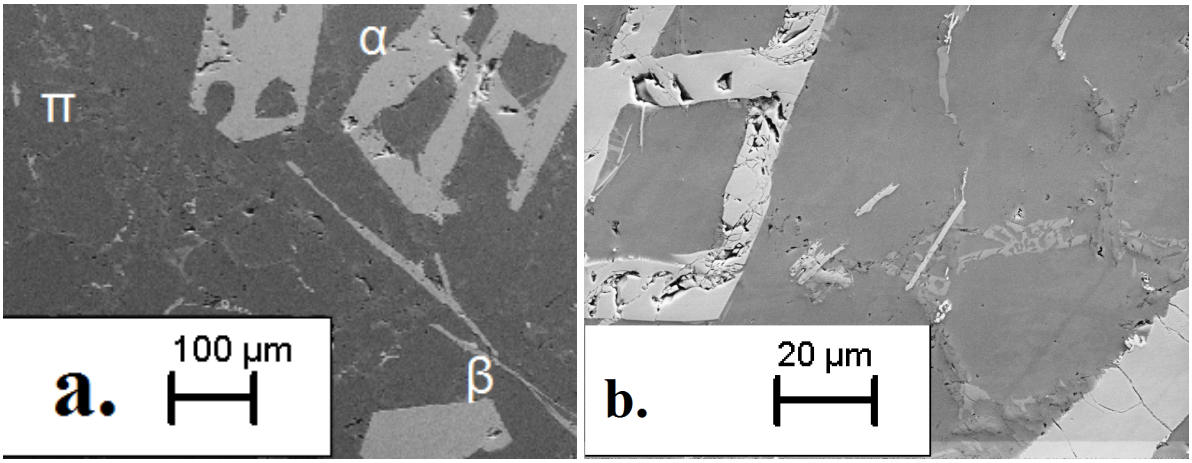

Figure 3.16: *(a) SEM image showing the three phases of Al-Fe-Si crystal present in the matrix after casting. The upper right, thick crystals are α-phase FeAlSi compounds, probably $Al_{15}Fe_3Si_2$ based on Shabestari et al. [98]. The faint, feathery pattern in the upper-left quadrant is thought to be the π-phase. Lower-right is the needle-like detrimental β-phase Al_5FeSi. (b) another SEM image of the same sample, showing the π-phase growing out of the β-phase, as seen in Shabestari et al.*

$$h\frac{2r_0+h}{2r_0} = \sqrt{k't} \tag{3.3}$$

$$h\frac{(2\times 950+h)}{2\times 950} = \sqrt{k'\times 300}$$

Taking $h = 20\mu m$ as a lower bound and $h = 200\mu m$ as an upper bound (3.4)

$$20\frac{(2\times 950+20)}{2\times 950} = \sqrt{k'\times 300} \tag{3.5}$$

$$\simeq 1.361$$

$$200\frac{(2\times 950+200)}{2\times 950} = \sqrt{k'\times 300} \tag{3.6}$$

$$\simeq 149.2$$

(3.7)

[39] was 1.70×10^{-13} m^2/s, even the lower bound here is very much higher than this. This suggests that the interface growth is reaction driven rather than diffusion driven, which agrees with Hwang et al, who state the validity of the equation as 15 minutes $< t <$ 24 hours.

3.3.2 Electron Microscopy

Sample Preparation and Results

Samples were prepared for use in the SEM by sectioning, grinding and polishing using the techniques described above, with a very good mirror finish necessary. When samples were mounted for use in the SEM itself, any electrically insulating sections were bridged with carbon tape to ensure that there could not be any charge build-up which could affect the results.

An attempt was made to use EBSD to gain more precise information about the steel alloy used in the reinforcing fibres, but this was unsuccessful because there was too much noise from the surrounding mounting resin and/or the fibre shape.

Of the two fibre types used extensively, the Dramix 3D 80/30 SL and Dramix 3D 80/30 3D BP, both showed very similar behaviour in the matrix at some distance from the fibre but the 3D SL fibres showed substantial interface formation whereas the 3D BP fibres showed almost none. This has been attributed to the different compositions of the steel in the two fibre types.

Based on the atomic ratios seen, of 10:1 Al:Fe and trace Cr and Si, the 3D SL fibre/matrix interface seemed to be composed of a mixture of Al-Cr-Fe compounds, probably $Al_{19}Fe_2Cr_4$, Fe-Al and Fe-Al-Si compoinds, probably Al_5FeSi and FeAl [58].

In Figure 3.17, the fibre-matrix interface is examined using the "line-scan" function of the SEM. This uses the EDAX detectors with the electron beam set to slowly cover a pre-designated line instead of the usual raster scanning pattern, and gives a very spatially-precise measurement of the elemental composition of a surface region. The $10:1:1$ ratio of Al to Fe and Cr suggests [58] a mixture of $Al_9.5FeCr_2$, Al_5FeSi and FeAl. Silicon appeared to preferentially segregate to the edge of the matrix, which may well be a factor of its lack of solubility in solid Al. The intermetallic compounds form very clean-edged crystals rather than a more amorphous region, suggesting that the interface growth is reaction-driven rather than diffusion-driven.

Looking at the needle-shaped inclusions in the matrix, shown in Figure 3.18, the hypothesis that β-phase Al_5FeSi is present is well-supported. The consistency of composition across all the areas

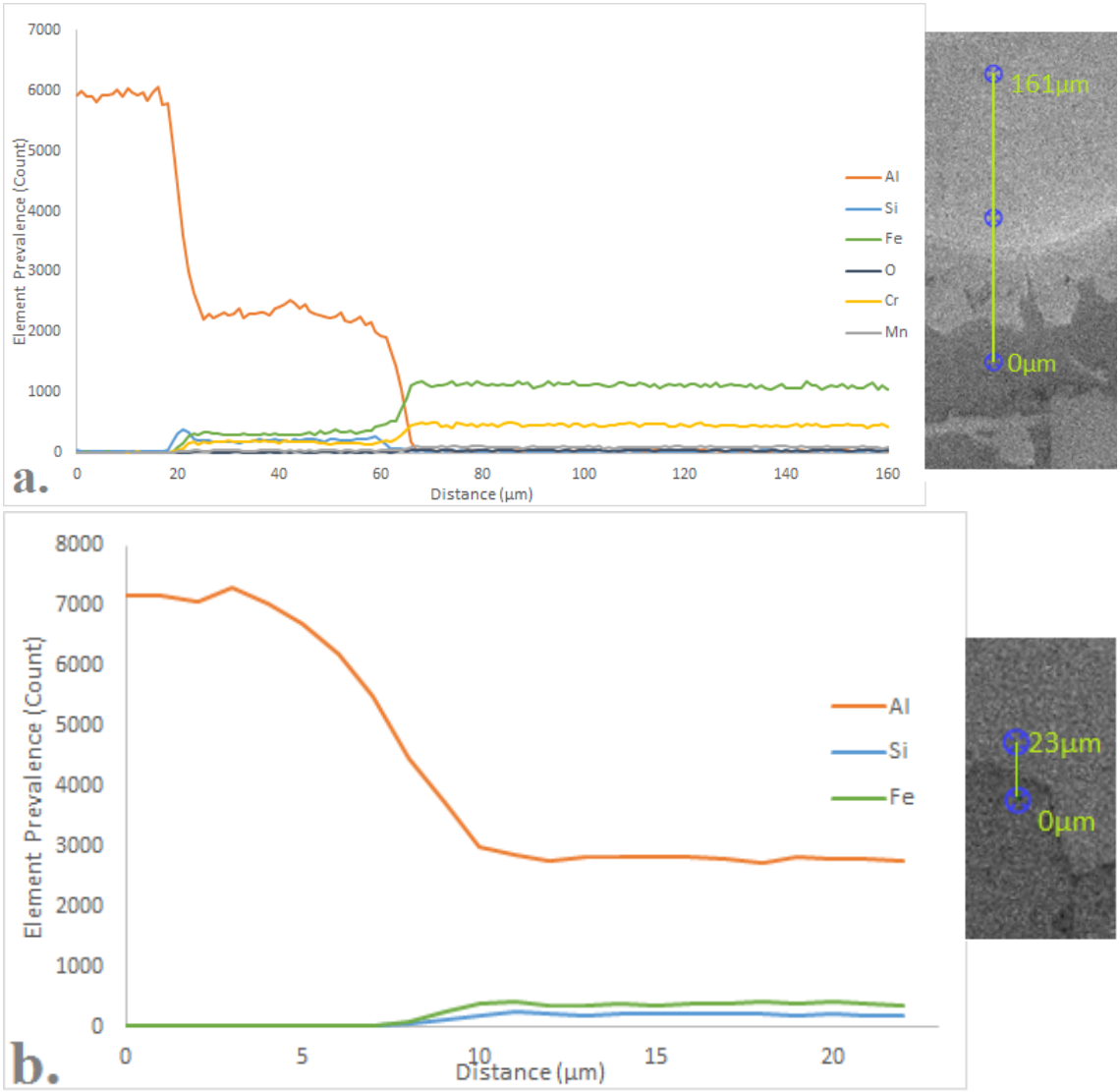

Figure 3.17: *(a) SEM line-scan showing a single phase present between the Fe fibre and the Al matrix. The recorded ratio is 10 : 1 : 1 by atomic weight, suggesting a mixture of* $Al_{9.5}FeCr_2$ *and,* Al_5FeSi *and FeAl [58]. The silicon seemed to be segregated towards the matrix edge, though this may be a depth artefact. (b) a close-up on the edge of one of the intermetallic crystals, showing a sharp edge. Fibre: 3D SL.*

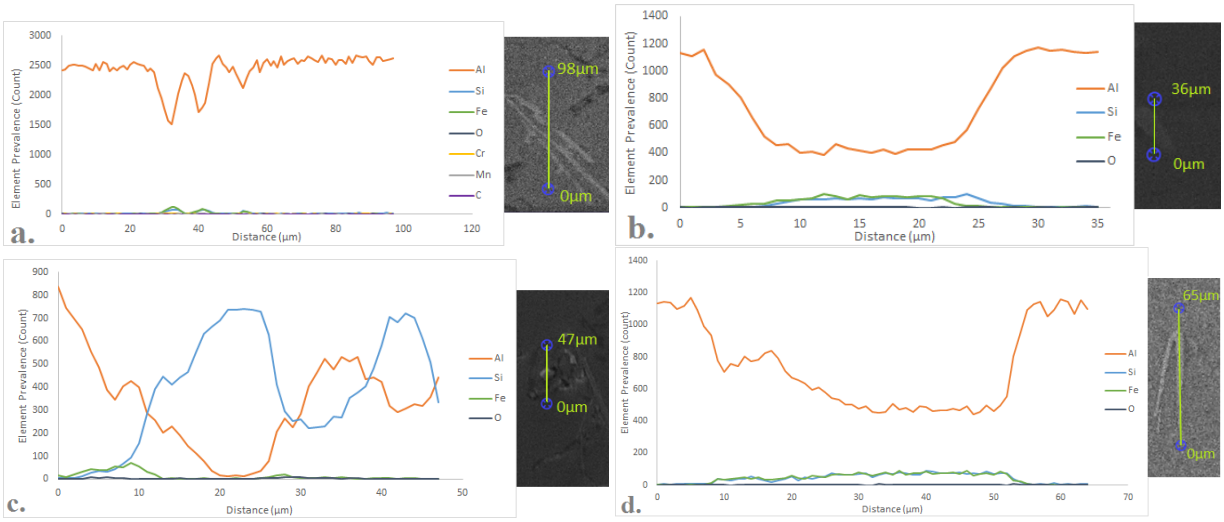

Figure 3.18: *Four β-phase inclusions, in which Si and Fe are present in equal quantities. This supports the hypothesis that this phase is $Al-5FeSi$. There is no significant difference between the 3D SL (a,b,c) and 3D BP fibres (d).*

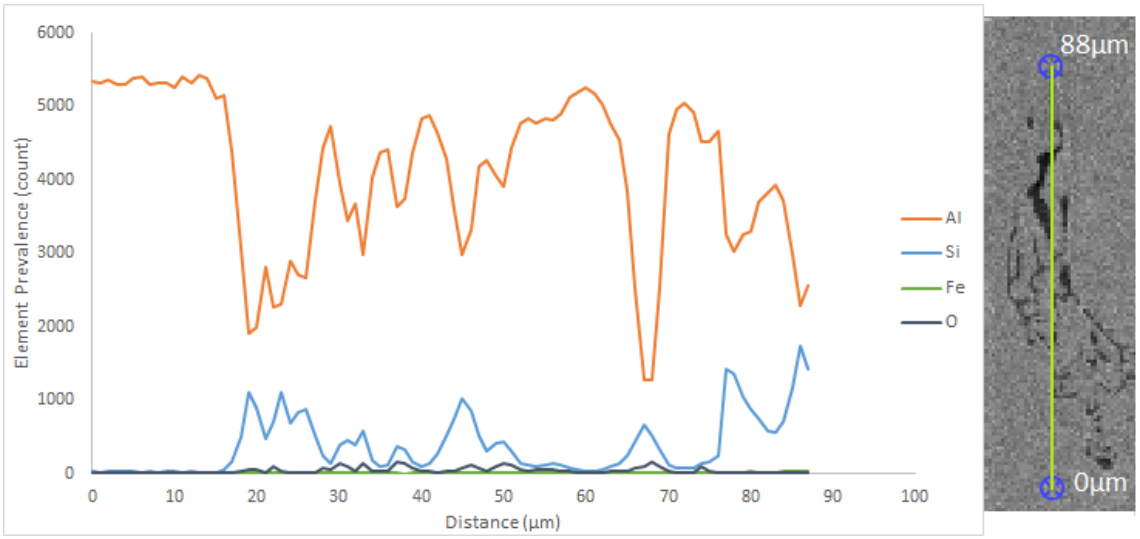

Figure 3.19: *An includsion in the matrix. Elementally composed of Al, Si and O it is thought to be a combination of Al_2O_3 and SiO_2.*

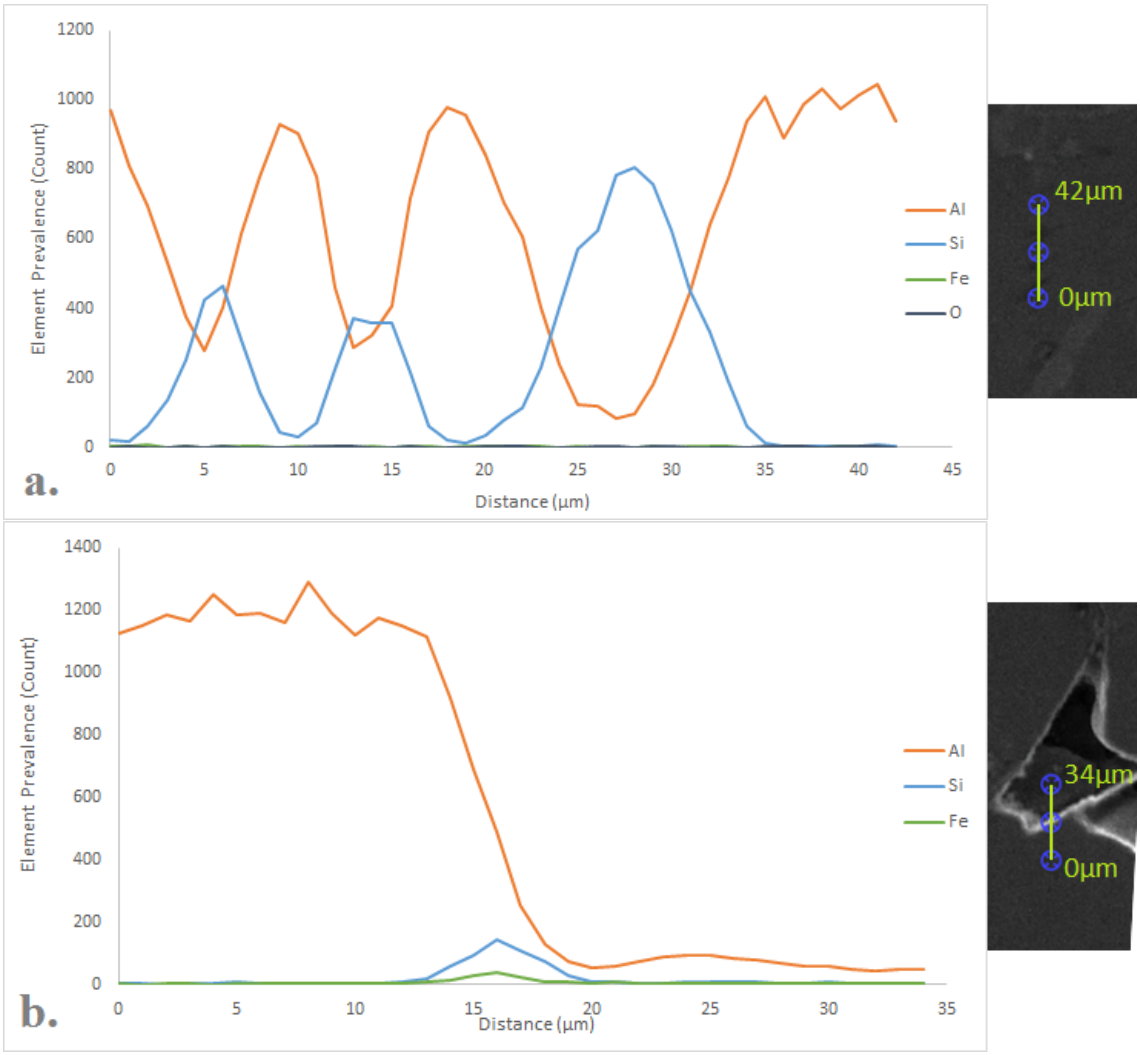

Figure 3.20: *(a) Some inclusions were composed of AlSi compounds entirely, with no iron measured present. Fibre: 3D SL. (b) a scan across one of the small shrinkage pores, showing that Si does segregate towards the grain boundaries, as would be expected for the matrix alloy.*

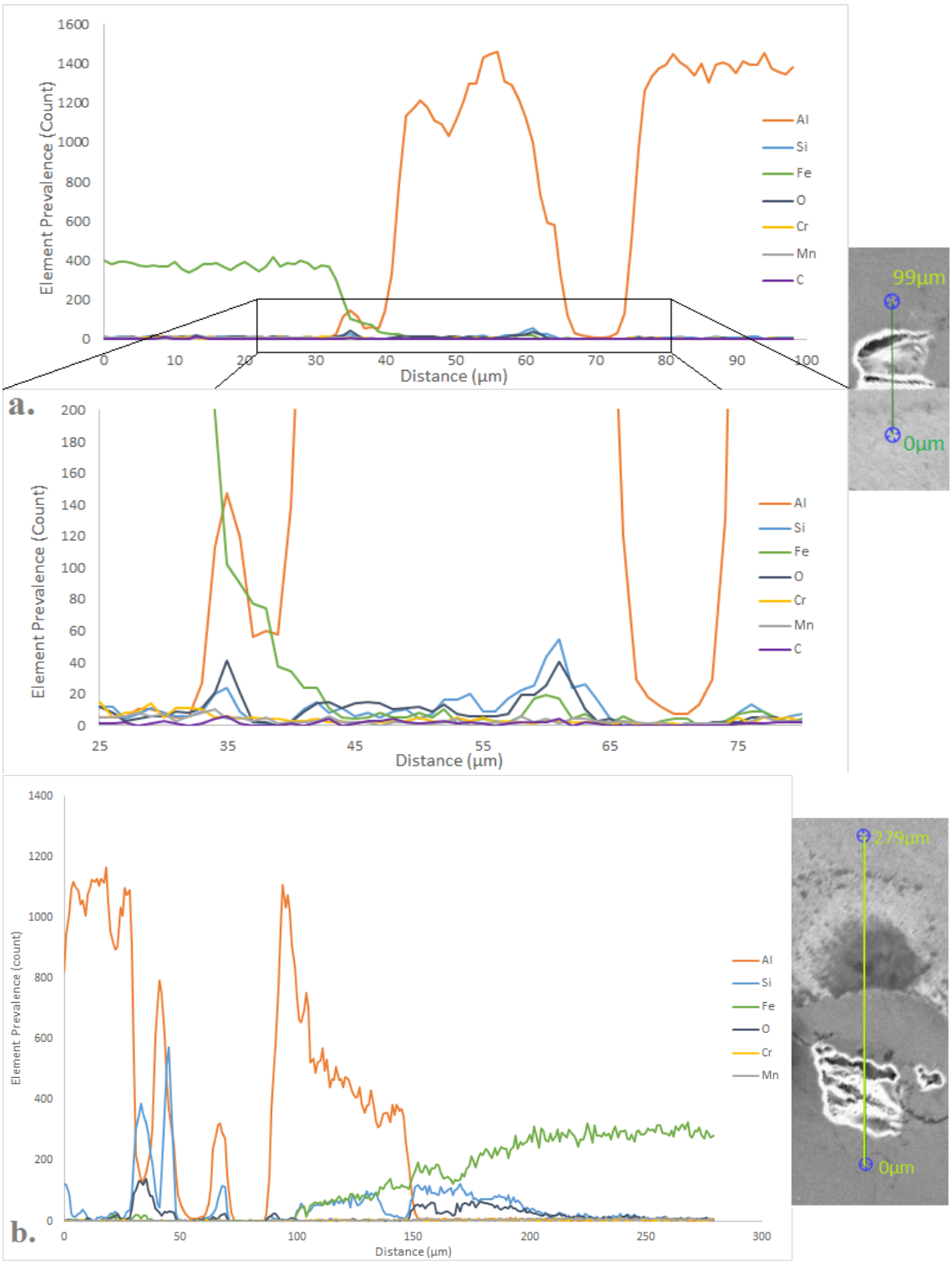

Figure 3.21: *(a) A void formed precisely at the fibre/matrix interface. Within the void, O and Si are more present. Fibre: 3D BL. (b) The smooth increase of iron is probably indicative of fibre present below the surface seen, rather than intermetallic compounds, but the segregation of Si and O to the void is still seen.*

scanned further suggests that the needle-shaped inclusions are a single phase. The variation in the measured Al present is due to the "depth" to which the inclusion is found vertically through the surface, since the SEM scans a small volume rather than precisely the surface. Figure 3.18c shows the inclusions perpendicular to the polished surface, and suggests that pure Si may be present around the β-phase needles.

Looking closely at a large Al-Si-O inclusion in a matrix region, in Figure 3.19, based on the atomic ratios present, the region is thought to be a combination of Al_2O_3 and SiO_2. This is likely to have formed around the oxide layer from the molten Al, which will have been broken up and pushed into the melt by the addition of the fibres.

Figure 3.20 shows the composite in a region of matrix more than 200 μm from any fibres. In Figure 3.20a, it is seen that some inclusions at a distance from a fibre surface were composed entirely of Al and Si, with no Fe detected. It is thought that these Al-Si compounds have formed, due to cooling of the area, before any iron, reacting and moving away from the fibre surface, has reached the area. The cooling of a region would further impede this process. In Figure 3.20b, a small shrinkage pore, Si is seen at the edges of the pore, suggesting that it has precipitated out of solution at the grain boundaries as it would be expected to in monolithic A357.

Looking at the line-scans taken across a void at the fibre/matrix surface (Figure 3.21), it is more difficult for the automatic element-selection program to identify which elements are present in the void area. Oxygen and silicon are both more strongly detected, suggesting that the oxide film from the surface of the liquid aluminium has not reacted as it has elsewhere, and that Si segregates to the crystal edges during solidification as it has elsewhere in the composite. Figure 3.21b shows one of the limitations of the line-scan technique, in that the apparent smooth increase in iron concentration is much more likely to result from the angled surface of the steel fibre taking up an increasing fraction of the scan depth than a true indication of chemical behaviour at the visible surface.

Using element maps (Figure 3.22), it can be seen that the chromium reacts with aluminium to form Al-Fe-Cr intermetallic compounds in both the interface region and the matrix. It is present in the "Chinese script" inclusions but not the β-phase needles. The nickel and manganese are not found

outside the fibre surface. This is attributed to the greater reactivity of Al with Cr and the fact that the Cr will tend to have been present on the fibre surface in a stainless steel. Two distinct phases of Al/Si compounds are also visible, one (the β-phase) much richer in Si than the other.

While not as precise as a line-scan, element maps can give an overall visual representation, shown in Figures 3.22 and 3.23, of the atomic composition of a sample. They can also give an approximate quantitative breakdown of the composition of each phase. From this we learn that the Fe has dissolved into the matrix at around 1% wt, that it is present in some of the inclusion phases quite strongly, and that the Ni has indeed not left the fibre but the Cr has to a small extent.

This is similar to the behaviour seen in the gravity cast samples (see Section 3.2), except that there is substantially less iron dissolved into the matrix. This is perhaps due to the fibres being introduced to the matrix after being removed from a preheat oven set to 120°C rather than at 550°C. Since iron inclusions weaken the matrix, this is a further reason to prefer the induction manufacture process.

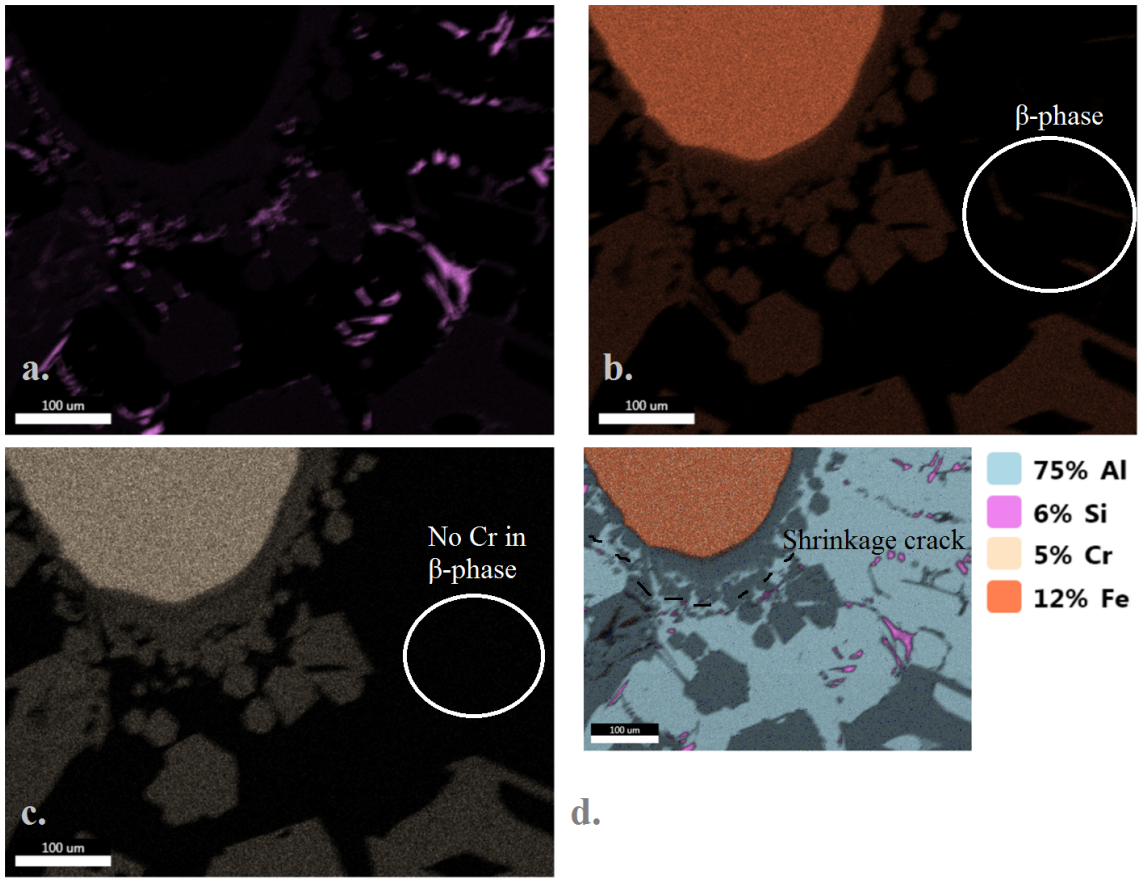

Figure 3.22: *Example of an element map from the SEM. The images show the distribution of (a) Si, (b) Fe, (c) Cr and (d) Al, Fe, Si and Cr, overlaid onto a low-contrast greyscale image of the region. Worth noting is that the Si seems to have segregated to the edge of the shrinkage crack and that the Cr is present in the interface phase along with the iron, but not present in the β-phase needle.*

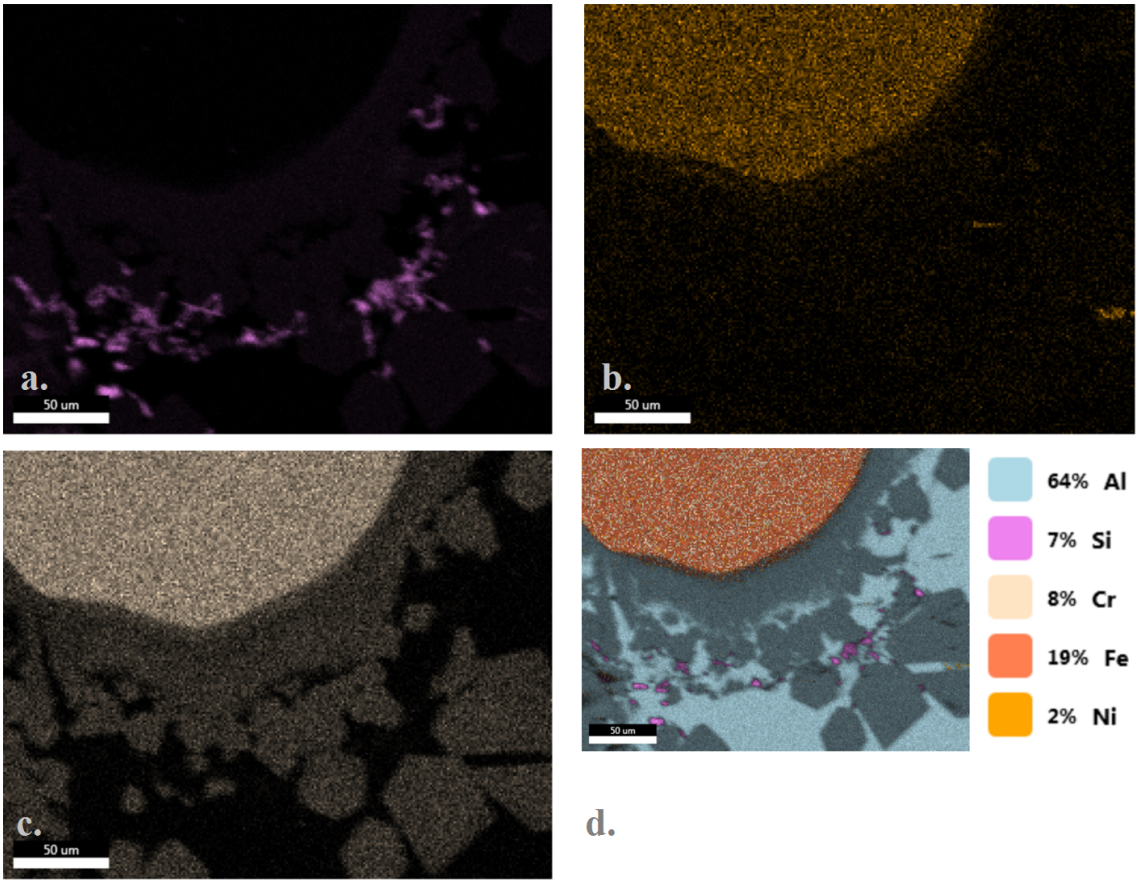

Figure 3.23: *Example of an element map from the SEM. The images show the distribution of (a) Si, (b) Ni, (c) Cr and (d) Al, Fe, Si, Ni and Cr, overlaid onto a low-contrast greyscale image of the region. In this case, the Ni is not present in any phases outside the fibre, unlike the Cr.*

3.4 Summary

This chapter discussed the fundamental considerations behind the design of the HMMC, including the reasoning behind the choice of A357 as the matrix alloy, the commercially available fibres and a summary of their properties, and the choice of a non-oriented fibre distribution. It also discussed the initial attempts to produce a composite by open-air casting using only the pressure created by the weight of the Al to force infiltration onto the fibre network, the reasons this was unsuccessful and the fact that other casting methods were not pursued beyond initial experiments. The best parameters were found to be 700°C A357 cast into 560°C fibres.

It detailed the investigation of a 4%wt iron matrix, to determine whether the composite could extend the usability of otherwise-unrecyclable aluminium. The reinforced high-iron composite did not show higher strength than the unreinforced reference specimen.

The successful induction manufacturing process was covered, including the discovery of the optimal casting parameters: immersing fibres at 200°C into A357 at 700°C without current, reactivating the current and stirring while the temperature was raised to 650°C and removing from the furnace over approximately 2 minutes.

Microstructural examination of the resulting composites showed the types of intermetallic compound formed at the interface. Specifically the presence of both beneficial α-phase and detrimental β-phase intermetallics were confirmed in the induction-cast composite, although α-phase inclusions were not found in the gravity-cast specimens. π-phase inclusions were also seen, and potentially provided some strength through grain refinement. The difference in the intermetallic compounds formed is thought to result from the shear forces created by the current in the induction furnace.

Detailed SEM maps and scans of regions of interest were taken. This enabled verification of the composition of the previously identified compounds and some observations about the reactions with alloying elements in the steel fibres.

The induction furnace manufacturing route is both more rapid and more effective in producing a composite free of voids and with a good microstructure than the gravity casting route. It allows in

principle for control of the interface thickness when stainless steel fibres are used, without requiring pressurised casting apparatus. The grain sizes in the final composite product were comparatively large, and the investigation of further grain refinement by heat treatment or by melt additives would merit further work.

The fibre-matrix interfaces formed using this route are similar to those found in the literature [39] [6], albeit thinner, and they do not follow the diffusion-based growth rate hypothesised by Hwang et al [39].

Twin-roll casting around a sintered fibre mat, also a commercially available product, would be another potential manufacturing route for producing a flat composite with a comparatively fine grain structure. Extremely preliminary examination suggested that infiltration was good but that producing an even layer of matrix on either side of the reinforcement would be difficult.

Chapter 4

Quasi-Static Testing

The behaviour of aluminium alloys is strongly strain-rate dependent [66]. Given this, it is helpful to divide the characterisation of an Al-matrix composite into two regimes.

The quasi-static regime is found at strain rates below 10^3 s^{-1}. All relaxation mechanisms are active and the sample can be assumed to behave isothermally [26]. The dynamic regime is found at strain rates greater than 10^4 s^{-1}. Some relaxation mechanisms, such as dislocation motion, operate on shorter distance scales, and a sample can be assumedto behave adiabatically. This means that the relative importance of different relaxation mechanisms to material deformation will be varied as the long-distance mechanisms will not have time to become active. Testing at a variety of temperatures or in the intermediate strain rate regime is outside the scope of this project.

Properties such as compressive strength, tensile strength, surface hardness and bending or fatigue performance are best measured in the quasi-static strain rate regime. This is particularly true of tensile testing, as high-strain-rate tensile tests are both difficult to calibrate and require specialist machinery to perform.

The combination of macroscopic testing with microscopic analysis is very effective in providing insight into the characteristics of a composite material. This chapter discusses both the properties directly obtained from the tests performed, such as the ultimate tensile strength (UTS), and their relationship with the nature of the damage sustained within the samples.

When considering the characterisation of a composite, the most commonly tested properties are the ultimate and yield strengths in tension, compressive strength, thermal cycling, fatigue, hardness (which can vary in different test planes), and possibly thermal fatigue [37].

4.1 Compressive Testing

The main priorities for the experiments discussed in this chapter were rapidity and repeatability: it was necessary that the tests take a minimum of time as the imperfect casting procedures suggested that good deal of repetition was likely necessary. This was borne out by the initial rounds of both tensile and compressive testing, in which poor casting procedures resulted in some unusable data as discussed below.

Compressive tests were chosen to begin with since the test pieces do not require independent design and can be cut directly from the initial casting. A custom pressure head for the compressive test machine was made in order to prevent damage to the compressive tester. The several types of available fibre were compared and the effects of strain rate were looked at, in an attempt to get an overview of composite behaviour.

Compressive testing was performed on an Instron hydraulic test machine with a 100 kN load cell. The samples were placed between a tungsten disc and a steel pressure head, which was designed to fit into the machine's grip and to be smoothed between tests. These were used to prevent damage to the testing machine. In order to prevent barrelling, the top and bottom of the specimens were lubricated with petroleum jelly. Compressive tests were performed at a strain rate of 0.25 mm/min unless stated otherwise, to ensure quasi-static strain rate behaviour when not exploring strain rate sensitivity. 0.25 mm/min will lead to a strain rate of 1.5 /s for a 10 mm sample and 1.0 /s for a 15 mm sample, well below the 10^3 /s threshold. An overview of the tests performed is presented in Table 4.1.

Compression or Tension	Number of Tests	Strain rate (mm/minute)	Gauge width (mm)	Notes
Compression	8	0.15 - 10	20 - 30	
Compression	7	0.15	20	
Tension	9+1 reference	0.15	12.5 mm	2 specimens slipped in grips
Tension	4+1 reference	0.15	12.5	As-cast
Tension	4+1 reference	0.15	12.5	Heat treated
Tension	4+1 reference	0.15	12.5 4 %wt	Fe matrix

Table 4.1: *Specification of the mechanical tests performed*

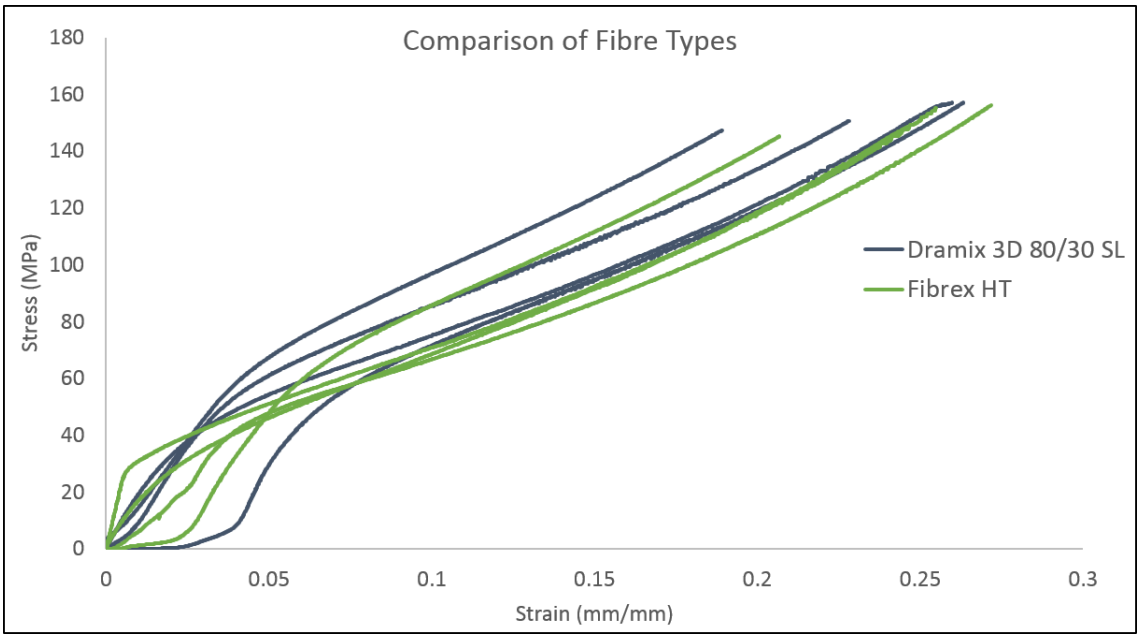

Figure 4.1: *Initial compressive tests showed that the A357, 10% wt reinforcement composites were almost entirely plastic, as expected [6] [55]. Tests were performed at 0.25 mm/minute (quasi-statically). This graph compares the strength added by the two fibre types (Dramix 3D 80/30 SL and Fibrex HT). The Dramix fibres have a higher average strength and a higher peak strength, but the difference is not large and the spread (due to voids and casting defects) was large. All of the specimens with each fibre type were cast under the same conditions to ensure comparability of the tests.*

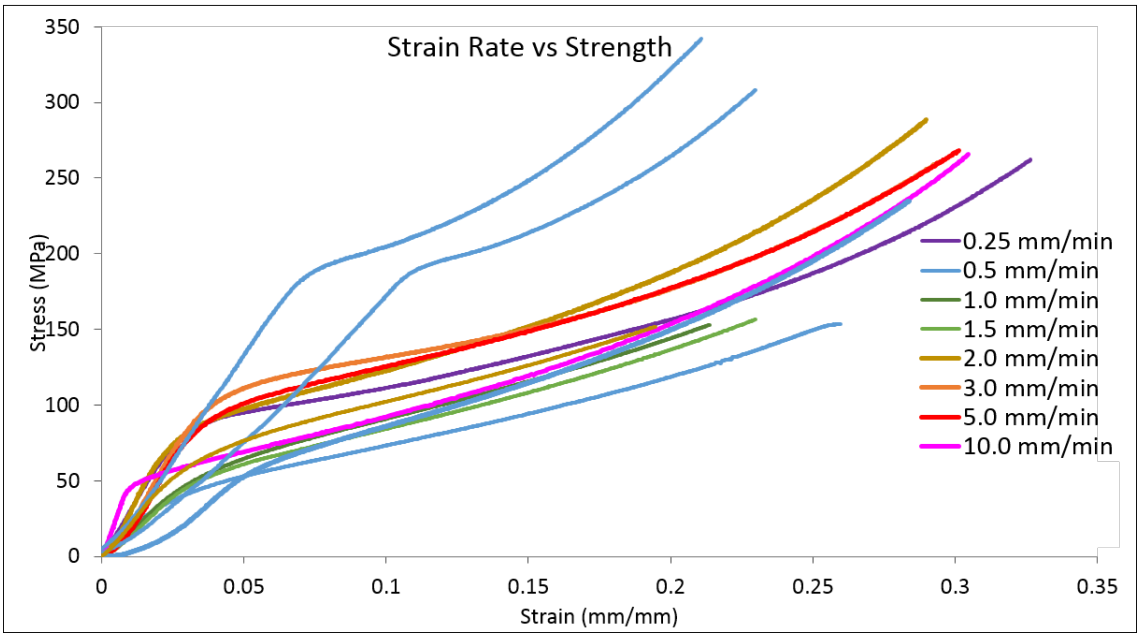

Figure 4.2: *A comparison of the compressive stress/strain curves for an A357/10 % vol Fibrex HT composite at strain rates from 0.25 mm/min to 10 mm/min. While there is a general trend for higher strength at higher strain rates visible even across this narrow range, it is obscured by the general inconsistencies from sample to sample.*

4.1.1 Results, Imaging and Analysis

Despite the lubrication used, the samples did show evidence of barrelling after testing. They also showed crushing damage to the matrix between the fibres, but little damage to the fibres themselves. Fibre displacement was observed to a great extent, with some loops of fibre pushed clear of the matrix in which they had been embedded.

As shown in Figure 4.1 and Figure 4.2, the addition of any reinforcement renders the composite almost entirely plastic. The variation in stress response with strain rate was not straightforward. The change from a more Γ-shaped curves seen are plausibly representative of a better-produced composite, with the slow crushing of voids in the material giving a smoother S-shaped curve with a less clear yield point. Some increase in strength with increasing strain rate is seen but the trend is weak.

The absence of elastic deformation during low strains is in agreement with Clyne et al [3], who attribute this to the stress inhomogeneity in the matrix arising from the reinforcement. This is somewhat corroborated by the fact that microstructural analysis found crushing damage at the fibre edges rather than in the bulk of the matrix, meaning that the strain concentration effects of the fibre/matrix interface is dominating the damage mechanisms.

The peak strength obtained, defined as the specimen which reached the highest stress before a large change in slope on the stress-strain graph, was 190 MPa. This is smaller than the range predicted by the Rule of Mixtures in Equation 4.1. This is thought to be because of the the casting technique did not produce a true composite material.

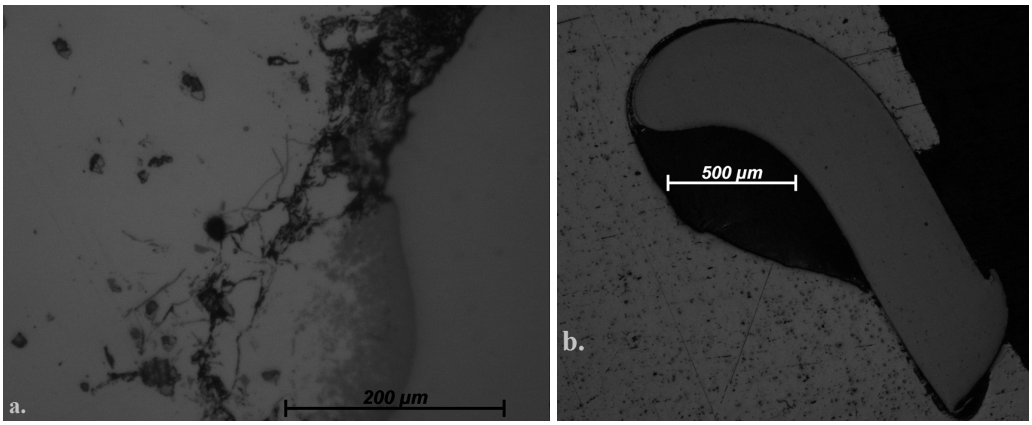

Figure 4.3: *Post-test compressive sample, showing (a) some crushing damage around a pre-existing shrinkage crack and (b) deformation of one of the fibres. It is thought that the void was already present in the sample, and that the fibre has been deformed adjacent to the weak point. Note that the fibre, while deformed, is undamaged.*

4.2 Tensile Testing

Tensile test design proved problematic, as the tensile bar was required to be as large as possible within the constraints of the available moulds. The design in 4.4 was chosen in order to maximise the gauge thickness of the specimen after it had been machined down to form the grips.

The maximum thickness of 20 mm corresponds to the mould used. While the minimum thickness of 12.5 mm minimised any "edge effects", which arise from the large size of the fibres in comparison to the gauge thickness, it did not eliminate them.

Initial attempts were made to test the bars on a 15 kN Instron test machine, but this was insufficient to break the samples used. The machine used for the test results shown here was an Instron 8802 250 kN pseudo-dynamic hydraulic machine equipped with a video extensometer and Dynacell loading cell.

Strain measurements were based on the force-extension data from the video extensometer, which tracked markings made on the exterior of the sample in white correction fluid (see Figure 4.4). These markings were placed at the limits of the gauge length, and for each sample their separation

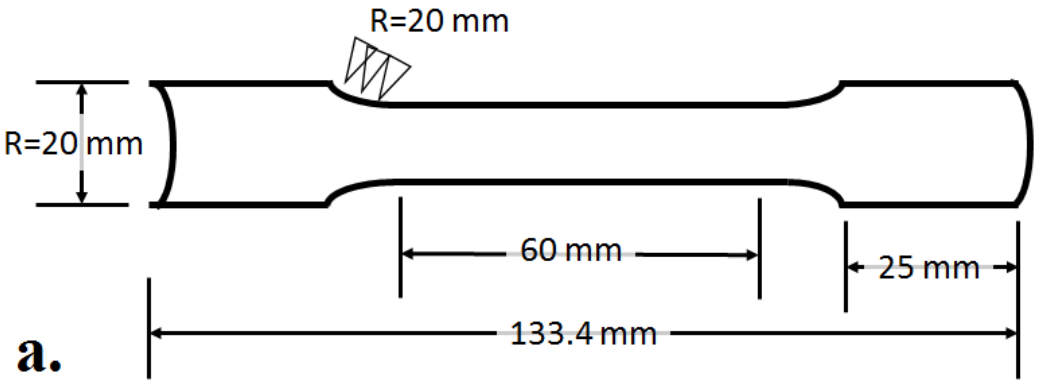

Figure 4.4: *(a) Diagram of the tensile test specimens used. (b) photograph of intact and post-test specimens. Note the markings for the video extensometer (red circles).*

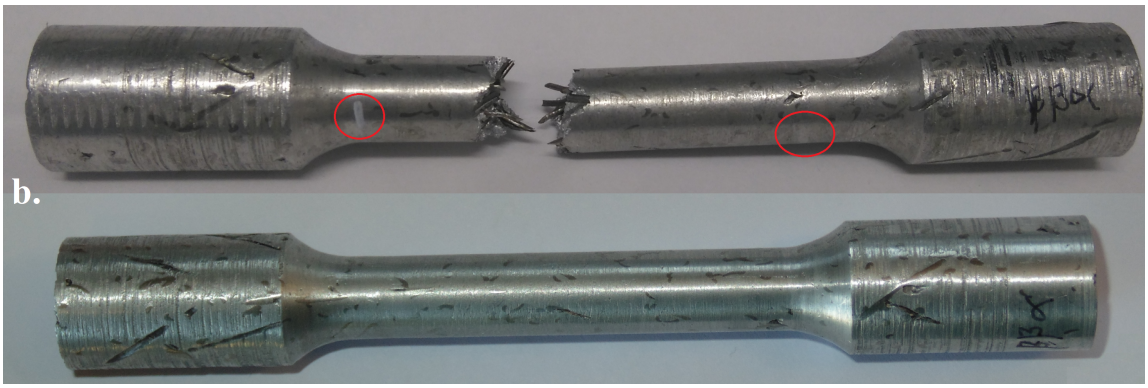

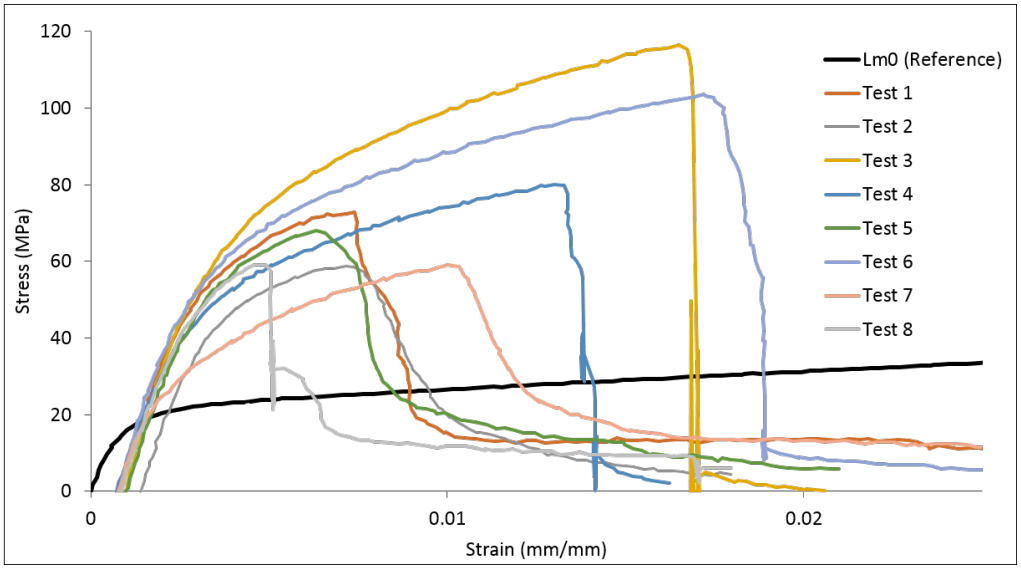

Figure 4.5: *Results of the initial tensile tests, which were all performed under the same conditions (0.1 mm/min). Tests 1-5 used Fibrex HT reinforcement and Tests 6-8 used Dramix 3D 80/30 SL. While the reference curve here is for pure Al rather than A357, the results are broadly as expected: a slightly higher strain and significantly higher stress at yield, followed by substantially improved load-bearing capability between strain and failure as well as increased brittleness.*

was measured with callipers and input into the test computer, as was the exact sample diameter. The video extensometer was preferred to a strain gauge because it was not possible for fracture to occur outside its measurement region and it could not change the strain response of the material.

The presence of fibres entirely spanning the gauge width created a point of critical weakness, which in the samples tested invariably nucleated fracture when present, as seen in Figure 4.6. However, the fibres which bridged the gap parallel to the testing axis allowed the sample to retain strength after the initial fracture, as had been predicted by Pemberton et al [10]. The nature of the fracture sites in Figure 4.6 suggests that the yield strength seen may in fact represent the fibre-matrix bond strength.

The testing also demonstrated that the casting process used for the fully-aligned composites was not sufficient to create a true composite, as in two out of three cases the entire fibre preform pulled out of the matrix. This, combined with the fact that a robust preform is needed to create such

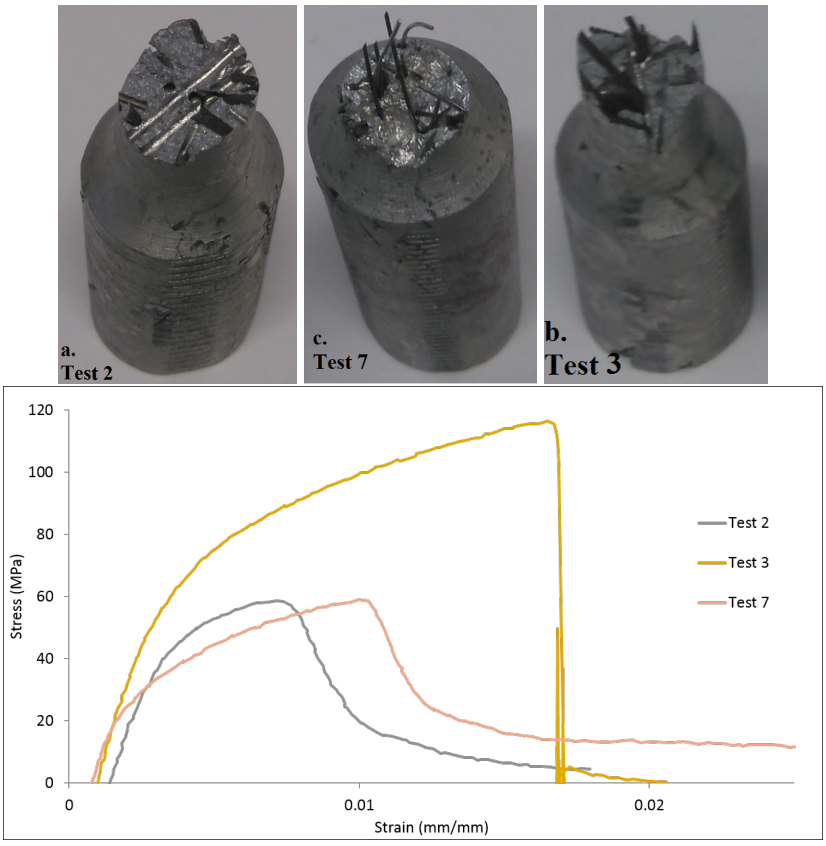

Figure 4.6: *(a) and (b) show a break point containing fibres parallel to the strain axis, with c. showing a break point with no such fibres. The graph (d) illustrates that these fibres spanning the break point provide post-fracture strength to the composite. Data are selected from the graph in Figure 4.5.*

composites, suggests that squeeze casting is a more suitable manufacturing method.

The largest voids seen were as much as 1 mm across. This is almost 10% of the gauge width, and in one of the very few samples not to have failed due to a fibre entirely covering the gauge width such a void was seen on the fracture surface. The clear detrimental impact of these voids was a significant motivating factor in the switch to induction-based manufacture.

The maximum strength achieved during these tests was 116 MPa, and the peak elastic modulus was 30 GPa. Using the figures for strength and elastic modulus quoted in this thesis and Equations 2.1 and 2.2, the strength would be expected to be within the region

$$344MPa \leq \sigma_c \leq 645MPa \tag{4.1}$$

and the elastic modulus within the region

$$74.3GPa \leq E_c \leq 92GPa \tag{4.2}$$

The measured strength falls significantly below this, thought to be because the weak point introduced by the bridging fibres is dominating the tensile behaviour. Using this casting method, critical weaknesses could not be eliminated as the maximum measured strength for any gravity-cast tensile specimen was 128 MPa and the highest stiffness was 30 GPa.

Attempts to measure the elastic modulus from these test results were so unreliable that the results were not regarded as a meaningful. Very high variation was observed and the values were consistently much lower than expected. A better tool to measure this property might be a plate vibration tester, which relates the resonant requencies of the material in the three coordinate planes to its elastic modulus.

For the majority of the initial test batch, failure occurred at a site where one or more fibres bridged the gauge width, which would be expected to create a weak site by presenting a very large cross-section of material only joined by the fibre-matrix bond rather than homogeneous Al. The weakest

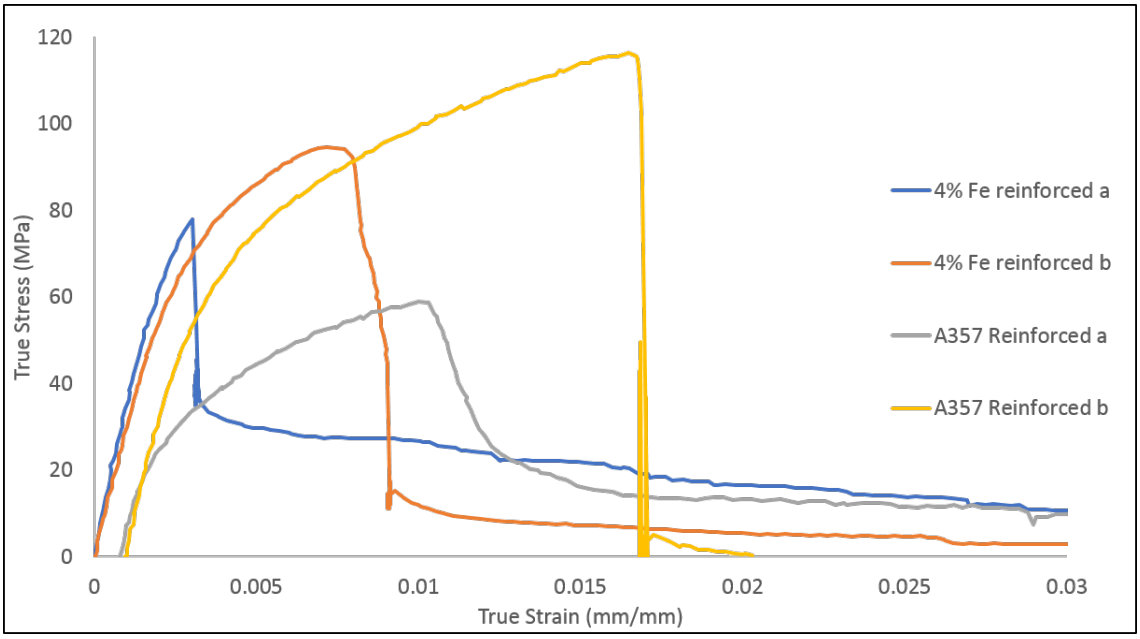

Figure 4.7: *With 4% iron by weight in the A357 matrix, it has become very brittle. While some fibres maintained some strength until 7% strain, the strength has not been improved over the base alloy.*

of the composites had the only failure site entirely bridged by two parallel fibres, supporting this hypothesis.

Exceptions to this were the aligned-fibre composites, which in two out of three cases failed due to the pulling out of the entire foil-wrapped fibre bundle from one half of the specimen piece, indicating that inadequate infiltration of the matrix alloy into the reinforcement had occurred. This was confirmed by later cross-sectioning. In the third case, the failure site was bridged by a single fibre. The results in Figure 4.6 suggest that the sample failed due to fibre pull-out, and that this sample was not detectably weaker than others.

The single thin-fibre sample in this test batch yielded at approximately 70% of the peak strain in the thick fibres. It also failed at a similar fibre-bridge point, though with far more significant pull-out. While interesting, the single sample does not permit reliable inferences to be made.

The samples with 4% wt iron added to the matrix performed very poorly, experiencing brittle failure at very low strains as shown in Figure 4.7. The results of these initial tests were sufficiently

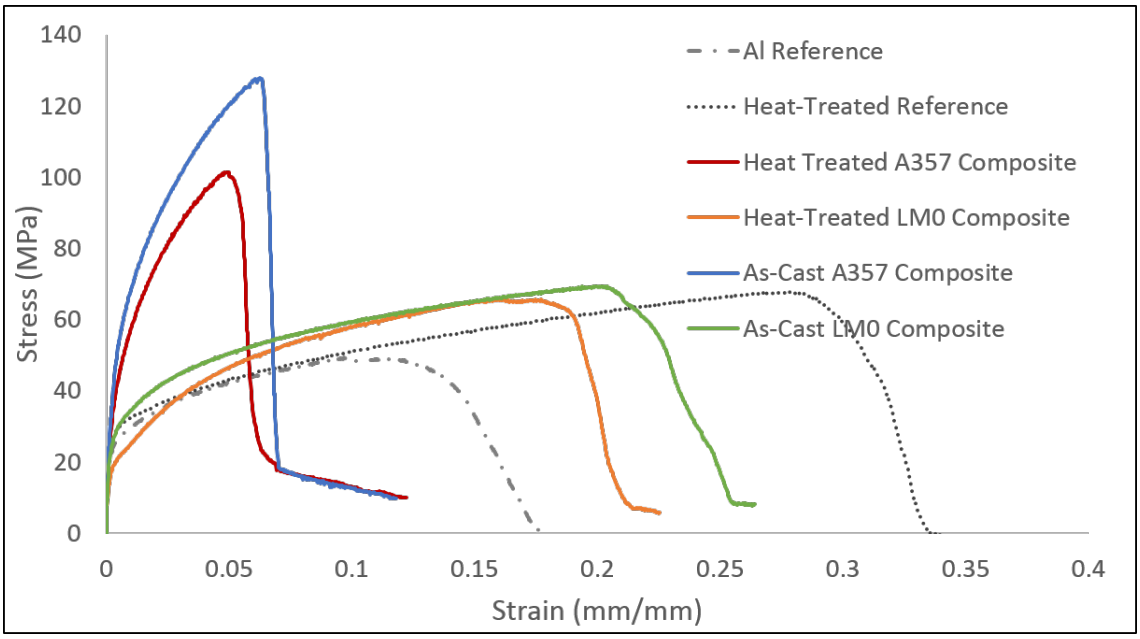

Figure 4.8: *More proficient casting has reduced the number of problematic fibre arrangements, as verified by photographs of the fracture sites, meaning that useful strains have been reached. However, the resulting composites are still of very uneven quality and only two reached high strength. The similarity of the heat-treated and as-cast specimens shows that heat treatment has not made a significant difference to the performance of the composite.*

un-promising that the idea of using the composite process to extend the usability of iron-rich Al alloys was not pursued.

The brittle failure of the high-iron specimens was indicated by the facture surfaces of the tensile bars, which had a very grainy structure with little peak-trough height variation. This is consistent with the literature suggesting the embrittlement of aluminium alloys by iron [99].

Looking at Figure 4.8, testing LM0/10% wt Dramix 3D 80/30 SL, it can be seen that while the peak stress achieved was higher than that in Figure 4.5, and there was significantly less rapid brittle failure (in part due to the LM0 matrix) the composite is still less strong than A357 alloy. In addition, the very uneven quality suggests that the gravity casting process cannot be used to create a satisfactory composite.

In an effort to improve the performance of the tensile specimens, some were heat treated. The

heat treatment was performed as follows: samples were put into an oven at 110°C and then heated over the course of approximately ninety minutes to 560°C, left at this temperature for 7 hours and then cooled over a further 4 hours to 150°C, then removed from the furnace and and quenched. These conditions, particularly the high maximum temperature, were intended to strengthen the A357 matrix and encourage the fusion of any internal voids present. A standard heat treatment procedure would have held the specimen at 560°C for 7 hours, quenched it and then aged it at 150°C for 4 hours in order to increase the strength through Al-Mg and Mg_2Si precipitation. In contrast, these specimens were not quenched at the higher temperature in order to minimise the risk of damage from the difference in thermal expansion rate between Al and steel.

The heat treated samples showed a slight degradation of strength, which is consistent with a thicker brittle region in the interfacial zone weakening the composite overall or with Al-Fe-Si grain growth. This is consistent with other work [39] [6] which found detrimental interface growth occurring above 400°C.

An examination of the fracture surfaces, examples of which can be seen inFigure 4.6 and Figure 4.13, suggests that failure was entirely brittle. This is in agreement with the stress-strain curves seen.

4.2.1 Single-Fibre Pull-Out Testing

Single-fibre pull-out testing, as performed by Pemberton et al. [10], provides useful information on likely failure modes as well as parameters for modelling the overall composite behaviour. Unsuccessful attempts were made to perform such tests with the HMMC.

To begin with, it was necessary to produce specimens with isolated single fibres embedded in the matrix. To achieve this, several fibres were partially embedded in a "comb" arrangement into heat-resistant sealant, which acted as a grip. Molten aluminium was then poured into a mould heated to 580°C, and the bare end of the fibre was inserted to approximately half its length and held in place until the Al reached a semi-solid state. The specimen was then removed to a room-temperature area and allowed to cool.

When cool, the specimen was carefully cut into several bars, each with a single protruding fibre. This procedure was modelled after that used by Pemberton et al [10].

When prepared, the samples were to be tested on a 1.5 kN Instron screw-driven test cell. Test parameters were set up for a standard tensile test. Force-distance information was measured only by the loading cell. The sample was gripped at one end by the Al bar. Several attempts were made to grip the exposed fibre, none of them successful.

Gripping the fibre directly invariably resulted in fracture at the grip point, invalidating the test. Encasing the fibre end in two-part epoxy resin resulted in a specimen which could not be clamped sufficiently tightly without shattering the resin and losing grip on the fibre. Winding the fibre around a test pin and gripping the pin also resulted in fibre fracture at the edge of the test pin. It was not possible to cast the upper end of the fibre into Al because the high thermal conductivity of the fibre would have caused the Al at the lower end to melt. Since no simple method could be found to grip the exposed fibre, the test was abandoned.

4.2.2 Imaging and Analysis

Samples were prepared for microscope analysis as described in Chapter 3. Microscope photographs of the exposed fibres resulting from tensile testing shows that there is some bonding occurring between matrix and fibres, since the exposed fibres have pulled some of the matrix out with them, as shown in Figure 4.9.

Some fibres also show pitting, which suggests that the matrix/interface bond was growing into the fibre surface as well as or instead of growing out from it in some cases. This is shown in Figure4.10.

This was not the case for all fibres, and large stretches of fibre have no attached matrix, which indicates that the initial bonding was weak or patchy (as shown in Figure 4.11.

Figure 4.12 shows three fibres at different distances from the fracture surface: Figure 4.12a, at the fracture surface, shows extensive cracking along the outside of the dendrite zone. Figure 4.12b

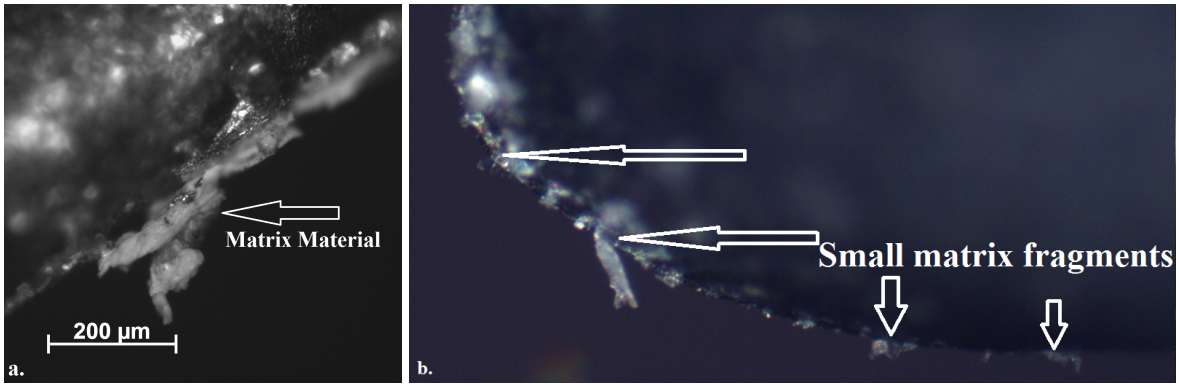

Figure 4.9: *Exposed fibres which have pulled out of the matrix during tensile testing. (a) a large section of matrix on the side of one of the fibres. (b) Many small fragments of matrix around the end of the fibre.*

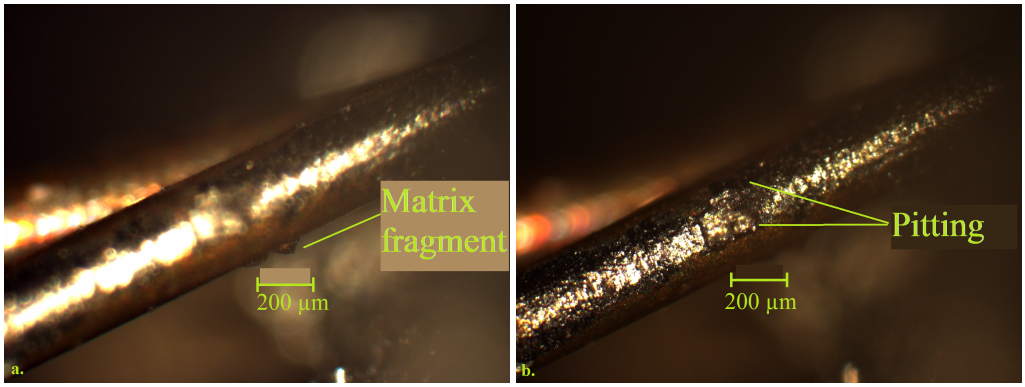

Figure 4.10: *Exposed fibre which has pulled out of the matrix during tensile testing, showing both pitting (b) and matrix fragments (a).*

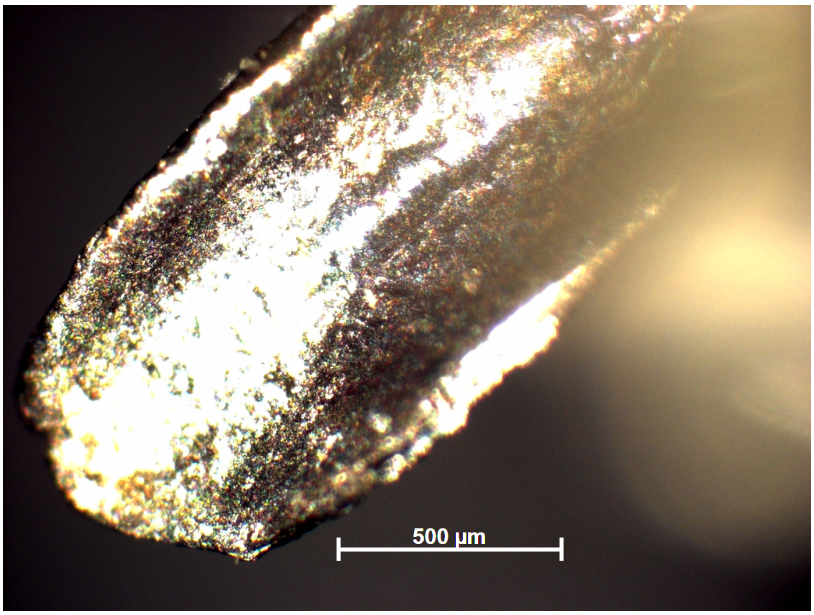

Figure 4.11: *Exposed fibres which have pulled out of the matrix during tensile testing. Very little matrix is attached to the fibre end in this case.*

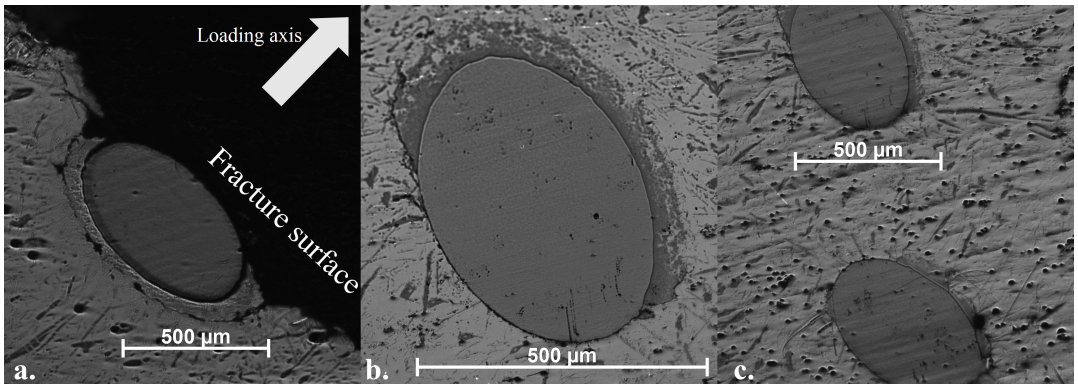

Figure 4.12: *Micrograph images of the composite from Figure 3.6 showing fibres and interfacial regions at (a), close to (b) and more than 10 mm away from (c) the fracture surface. There is no visible damage to or deformation of the interfacial region at any of the three sites, and the crack in (a) is entirely outside the visible interface.*

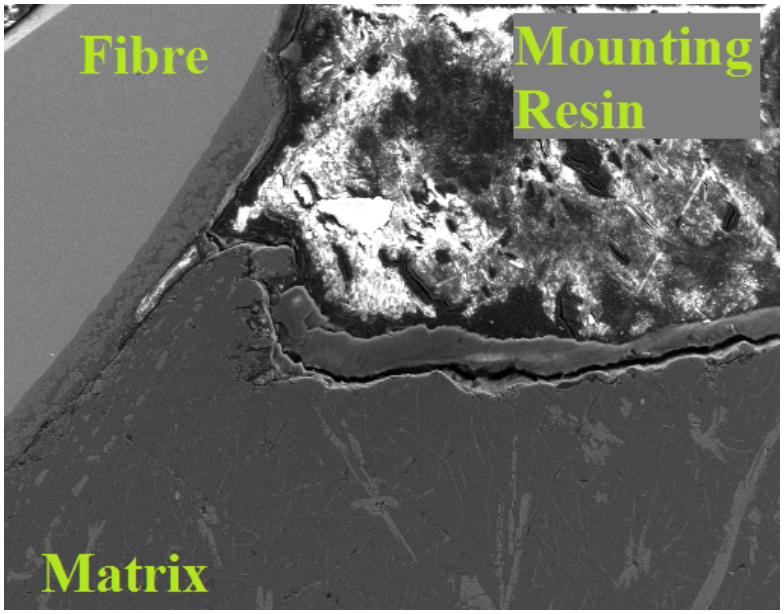

Figure 4.13: *FFracture surface of one of the tensile samples, showing both fibre and matrix. The surface is suggestive of brittle failure. Where an interfacial layer had formed, fracture appears to have been between it and the matrix rather than it and the fibre.*

shows less dendrite formation and much less cracking. It is not known whether this crack occurred during cooling of the composite or whether it was caused during testing. The Figure 4.12c shows a fibre with no cracking or visible matrix deformation, and no visible dendrite zone.

The variation in fibre state through the body of deformed samples means that damage was entirely localised at thepoint of failure. This is in agreement with the hypothesis that the fibre-matrix interface presents a point of critical and catastrophic weakness in the gravity-cast samples.

X-ray CT

X-ray CT scans were taken of three tensile specimens (Tests 2, 3 and 7 from Section 4.2, shown in Figure 4.6) at Nottingham University. the resulting images were converted into 3-D pictures and the individual images were assessed by the quadrat method to examine whether the fibre distribution was strongly clustered.

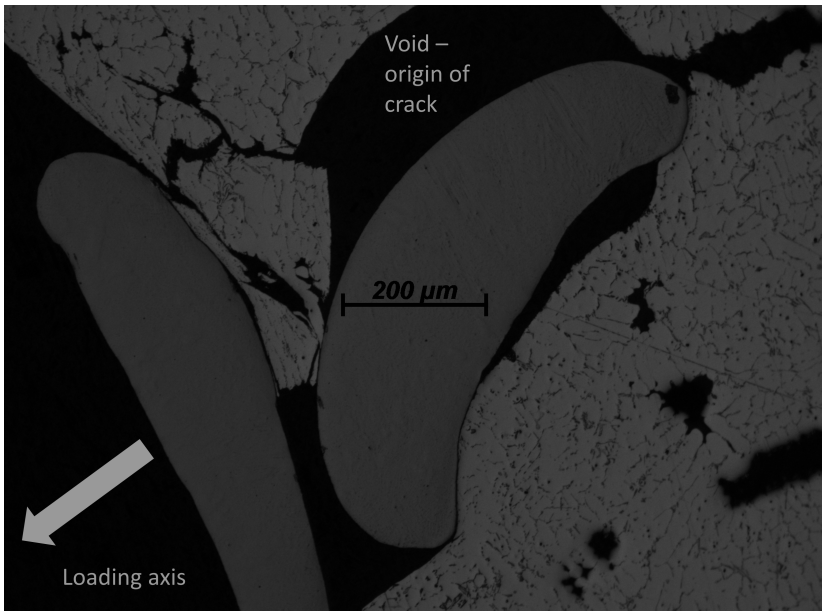

Figure 4.14: *Fracture surface of one of the tensile samples, showing cracking between and around two fibres. An explanation for the structure of the damage shown is the void here was the origin of the critical crack, and the damage propagated both perpendicular and parallel to the applied load.*

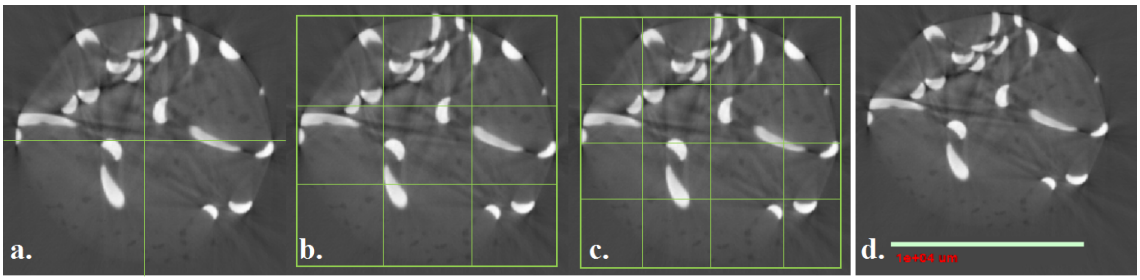

Figure 4.15: *An image of a single slice through the scanned specimen (d) and that slice divided for quadrat analysis (a, b, c). In the first quadrat analysis three grid sizes were used because the result should be independent of grid size.*

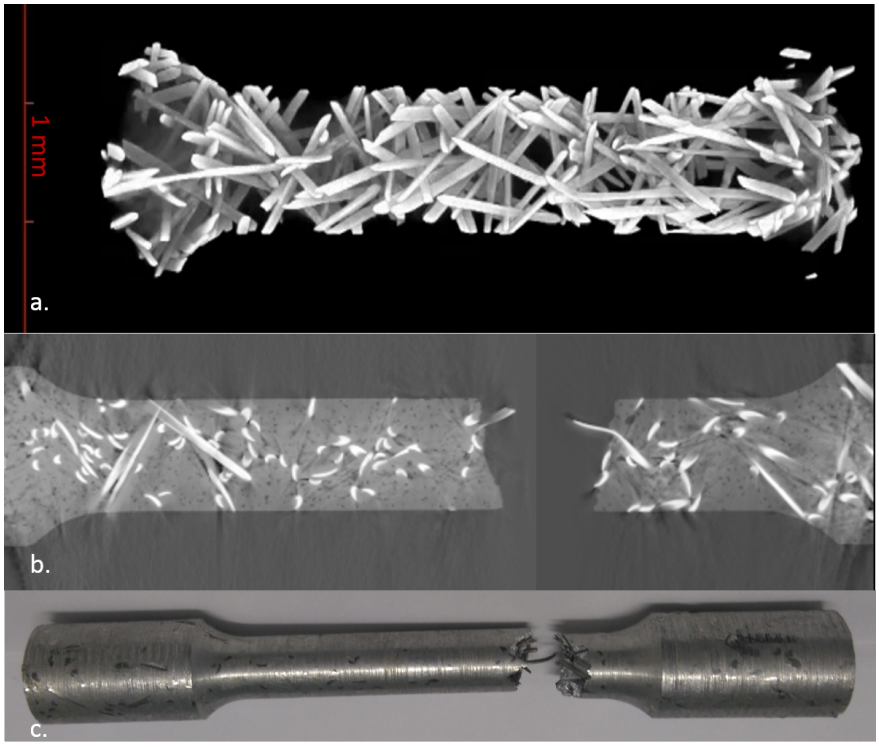

Figure 4.16: *For an A357/10% wt Fibrex HT composite, CT scans are presented in an as-cast state (a) and after tensile testing (b) and a photograph of the specimen after testing (c). The CT scan clearly shows that fibres not in contact with the failure plane have not deformed, showing that the bulk strength of the composite was not affecting its failure.*

The quadrat analysis was performed on every 50th slice in order to reduce the calculation burden (an average stack contained 1500 slices). Since grid size selection is so important to the method, for the first specimen analysed, as shown in Figure 4.15, three different grid sizes were trialled. If the results found are independent of the grid size chosen then this is an indicator that they are reliable.

The 2×2 grid gave a mean/variance value of 2.36; the 3×3 grid 0.92; and the 4×4 grid 1.03. This shows that both the 3×3 and the 4×4 grids were suitable, and the 3×3 grid was used for the subsequent specimens. The other specimens gave values of 1.22 and 1.35. These results suggest that the distribution of fibres is close to 2-D random in the partially-aligned fibre samples.

Presented in Figure 4.16 is a comparison between the internal fibre arrangement before and after

the specimen (an A357/10% wt Fibrex HT composite) was tested to failure in tension. This is presented in Figure 4.5 as the pink curve. Its peak strength was 55 MPa, and some post-failure strength was seen in the graph. This is attributed to the protruding fibre visible on on the CT scan, which had bent until it was approximately parallel to the loading axis and then snapped. This behaviour was consistent across the three specimens scanned before and after tensile testing.

4.3 3-point Bending Testing

Three-point bending tests are an additional method for characterising a sample, and were performed as a preliminary test to validate the choices of specimen dimensions before repeating the experiment under cyclic loading on a notched sample, giving a measure of the fatigue strength of the material. They also permit an examination of failure in tension which is not expected to be limited by the presence of bridging fibres.

Three-point bending tests were chosen rather than torsional tests because the torsional fatigue machines used at Brunel required samples with a 4 mm neck, which proved impossible to machine from as-cast samples.

In order to calculate the strength of a notched sample deformed under bending load, K, the stress intensity factor at a crack tip or fracture toughness, is defined along the three coordinate axes as

$$K_1 = \lim_{r \to 0} \left(\sigma_{yield} \sqrt{2\pi r} \right) \tag{4.3}$$

$$K_2 = \lim_{r \to 0} \left(\tau_{xy} \sqrt{2\pi r} \right) \tag{4.4}$$

$$K_3 = \lim_{r \to 0} \left(\tau_{yz} \sqrt{2\pi r} \right) \tag{4.5}$$

$$\tag{4.6}$$

where r is the radial distance from the crack tip. K is referenced as K_{ab} in which a is the plane perpendicular to that of the starting crack and b is the direction of expected propagation. Definitions

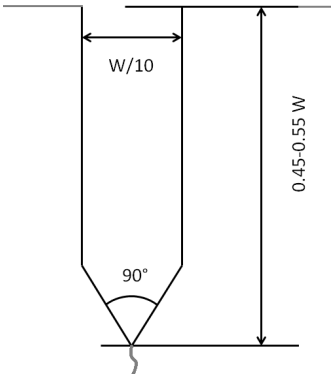

Figure 4.17: *Chevron notch chosen, diagram a copy of that in ASTM E-399 [100]*

are taken from ASTM E-399 [100]. The standard also requires a minimum of three tests in order to characterise a material.

Two groups of tests were performed, both on a screw-driven Instron 30 kN test machine fitted with a 3-point bending test head and set up for quasi-static compressive loading (2.0 mm/minute). The deflection heads had a radius of 15 mm and a spacing of 60 mm (the top two heads were 60 mm apart with the bottom head symmetrically between them).

The first batch used bars of 80 mm length, 20 mm width and 5 mm depth. The second used notched bars of 100 mm length, 25 mm width and 8.5 mm depth and a notch of 4.1 mm height and 4.0 mm width located 50mm along the length. The $1:4:16$ ratio of depth to width to length was chosen based on recommendations in ASTM E-399 [100]. All test bars were machined from an A357-Dramix 3D 80/30 SL composite with 10% wt reinforcement.

The flexural stress, strain and elastic modulus are defined as

$$\sigma_f = \frac{3FL}{2bd^2} \tag{4.7}$$

$$\epsilon_f = \frac{6Dd}{L^2} \tag{4.8}$$

$$E_f = \frac{L^3 m}{4bd^3} \tag{4.9}$$

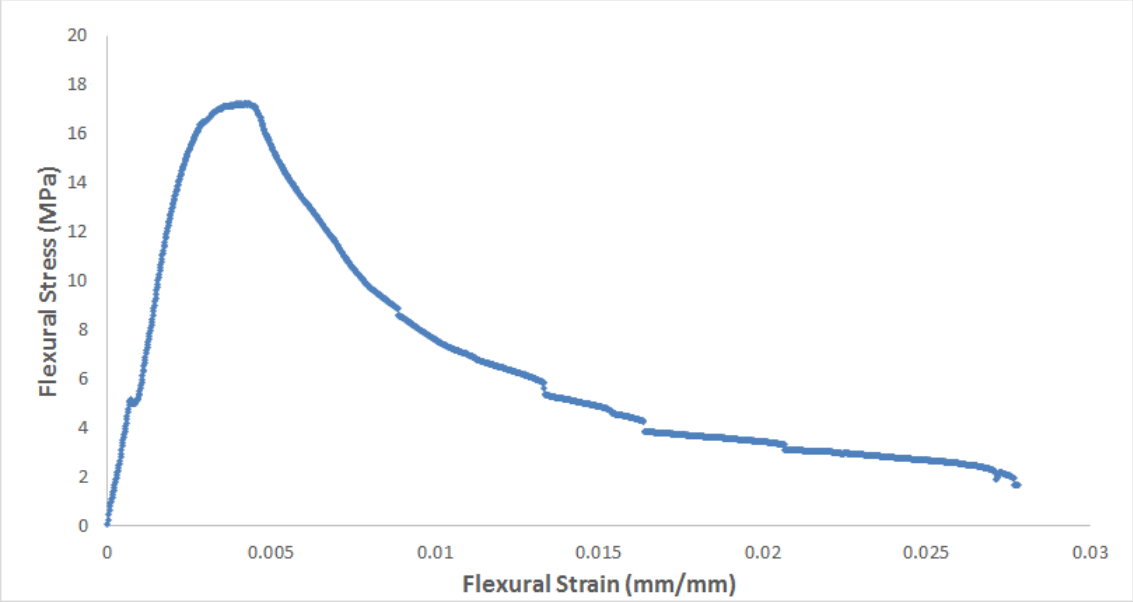

Figure 4.18: *The stress-strain curve for this sample shows very clearly that the material retains strength when several fibres bridge a crack - the graph discontinuities at approximately 0.009, 0.014, 0.017 and 0.021 indicate the snapping of a specific bridging fibre, which was audible during the test.*

in which σ_f is flexural stress, F is the instantaneous load, L is the diameter of the three bending rolls, b is the width of the test specimen, d is the depth of the test specimen, ϵ_f is the flexural strain, D is the instantaneous deflection of the specimen center, E_f is the flexural elastic modulus, and m is the gradient of the initial straight-line portion of the load-deflection graph.

When testing the specimens, an initial crack appeared very quickly even on specimens which had not been notched. All notched specimens failed at the notch, and not elsewhere. However, in many cases a fibre was sitting orthogonal to the loading axis, and would be anchored in the matrix on both sides of the emerging crack. These fibres would tend to snap rather than be pulled out of the matrix, with a sharp "ping" sound audible during the test. An example of this is visible in Figure 4.18. This shows that the material retains significant strength after fracture and before failure under flexural loads.

In some specimens, an initial crack could be heard which did not open up immediately, indicating the the critical crack length for failure is lengthened by the presence of fibres. This is in agreement

with both Pemberton et al [10] and the tensile test results. Some of the specimens had visible voids present, which would tend to nucleate failure except when a notch was present.

Using Equations 4.7 to 4.9, the flexural stiffness for each of the tested specimens was calculated and the mean flexural stiffness was found to be 2.8 MPa $\pm$ 2 MPa. The error was calculated using the standard deviation of the measurements. The very high measurement error is in part caused by the difficulty in identifying the elastic region of the stress-strain graphs. The peak flexural strength seen was 43 MPa, lower than the 95 MPa found for HIP-manufactured monolithic A357 [93]. This is most likely due to the solution strengthening produced by the thermal cycle in the HIP.

The geometry of the specimens, with a large cross-sectional area and a small depth, loaded such that the wide cros-ssectional area would be under stress rather than the depth, presented a specimen which did not fail when a fibre bridged the specimen vertically. An example of this from a single specimen is presented in Figure 4.18. This behaviour was more representative of the bulk properties of the composite than tensile loading. However, the very high variation in average flexural stress suggests that the specimens were still too small for bulk material behaviour to have been seen.

4.4 Hardness Testing

Vickers hardness is measured [26] by pressing a diamond-shaped indenter into the surface of the material and permitting it to dwell there for a defined period, in this case 15 seconds. The area of this indent is then related to the hardness via the formula [101]

$$H_v = \frac{2F\sin(136/2)}{d^2} \tag{4.10}$$

in which F is the applied force, 136° is the angle between the faces of the indenter and d is the average length of the measured diagonal.

In practise, because the indent is measured by a microscope and Vernier callipers, the number read from the callipers under high magnification was used to find the hardness in a look-up table supplied by the manufacturer.

Measuring Vickers hardness of the matrix before and after tensile testing gave an average value of 79.7 pre-test and 40.6 post-test; of the intermetallic zone gave 69.5 pre-test and 138.1 post-test and of the fibres gave 319.9 pre-test and 372.9 post-test. Aside from the matrix, this looks to be fairly consistent with work-hardening. Hwang et al [39] found the Vickers hardness of the fibre-matrix interface to decrease from around 950 towards the fibre to around 720 towards the matrix, though indenter pressure, matrix and fibre values and dwell time were not quoted.

Brinell hardness is measured by using a hemispherical steel indenter [102]. The indenting ball is pressed into the test piece at a specified force, allowed to dwell for around fifteen seconds and the resulting indent is then measured. The indent size is related to the hardness by

$$\text{Brinell} = \frac{2F}{\pi D - \left(D\sqrt{D^2 - d^2}\right)} \tag{4.11}$$

$$\text{and} \qquad 0.24 \leq d/D \leq 0.6 \tag{4.12}$$

in which d is the diameter of the indent, D is the diameter of the indenter and F is the indenting force. The hardness of a a reference piece of aluminium matrix was 42 ± 0.7, and of an induction-cast HMMC sample was 49 ± 2.7. The internal structure of the composite is quite large when compared with the size of the indenter head, so this high measurement error is not surprising.

In general terms, the Brinell hardness method is to be preferred to the Vickers hardness method because the indenter is large enough to cover intermetallic inclusions, matrix and some fibre in a single indent and thus gives a hardness value more representative of the bulk properties of the material.

Hardness Method	Specimen	Hardness Number	Notes
Brinell	1	41.952	
Brinell	1	42.444	
Brinell	1	40.802	
Brinell	2	43.080	
Brinell	2	42.373	
Brinell	2	42.052	
Brinell	2	42.264	
Vickers	1, Matrix	82.5	
Vickers	1, Matrix	62.7	
Vickers	1, Matrix	95.3	
Vickers	1, Matrix	80.5	
Vickers	1, Matrix	75.7	
Vickers	1, Matrix	81.5	
Vickers	1, Interface	60.0	
Vickers	1, Interface	57.5	
Vickers	1, Interface	60.6	
Vickers	1, Interface	99.8	
Vickers	1, Fibre	262.1	
Vickers	1, Fibre	321.9	
Vickers	1, Fibre	311.5	
Vickers	1, Fibre	356.7	
Vickers	1, Fibre	347.5	
Vickers	2, Matrix	44.2	Fractured in tension
Vickers	2, Matrix	41.9	Fractured in tension
Vickers	2, Matrix	41.1	Fractured in tension
Vickers	2, Matrix	35.2	Fractured in tension
Vickers	2, Fibre	372.9	Fractured in tension
Vickers	2, Fibre	376.3	Fractured in tension
Vickers	2, Fibre	369.6	Fractured in tension
Vickers	2, Interface	222.0	Fractured in tension
Vickers	2, Interface	54.2	Fractured in tension

Table 4.2: *Hardness tests on pre- and post-tensile-test specimens. All of the measurements were made more than 5 mm from any fracture surfaces.*

4.5 Summary

This chapter discussed the compressive tests performed on gravity-cast specimens, which helped to inform the choices of casting procedure and fibre choice. Tests confirmed that the composite was sensitive to strain rate, and found the tensile yield strength to be 190 MPa. Heat treating specimens was found to degrade their UTS and yield strength slightly.

The tensile tests performed on specimens demonstrated the need for large gauge widths in a test of this type, since the gauge width must be significantly greater than the length of the fibres.

The attempt to mitigate the embrittlement of aluminium with a high iron concentration was not a success, since the UTS was found to be 116 MPa, lower than the yield strength of the low-iron composite.

X-ray CT scans were performed on some specimens before and after tensile testing. These showed that the fibres, while axially aligned due to mould confinement, had a good degree of 2-D dispersion. The scans also showed that the damage was localised to the sites of critical weakness.

3-point bending tests were used to measure the flexural strength and stiffness. These tests found significant post-failure strength. Hardness tests were performed to further characterise the material. Vickers hardness measurements were of the matrix, interface or fibre rather than the bulk material. Work hardening was seen after tensile testing. Brinell hardness measurements found that the composite was harder than the matrix alloy.

Measurement of the elastic modulus was very difficult. The values found in tension and in flexure both had very high measurement errors and were significantly different to values found in the literature This is thought to be a flaw in the technique rather than a representation of the true values of these properties.

Both compression and tension show an improvement in strength when compared with aluminium cast under similar conditions, but the extensive presence of voids in the samples which were tested provide points of critical weakness from which damage can originate very easily. This was confirmed by a CT scan of some of the tensile specimens.

No significant difference in strength was found between composites reinforced with Dramix 3D 80/30 SL and the Fibrex HT fibres. The A357 matrix was found to be stronger than the LM0 matrix, but less ductile, which is in line with the behaviour of the monolithic alloys. The effect of volume fraction on final strength was not tested because attempts to produce specimens with volume fractions significantly above or below 10% wt were unsuccessful, as discussed in Chapter 3.

The presence of small fragments of interface on the exposed fibre surfaces suggests that a stronger interface will result in a stronger composite, but the performance of the high-iron composite and the strong influence of casting defects suggests that the strength of the matrix is more important to the performance of the composite.

The very high measurement errors for the tensile and flexural elastic moduli, which was primarily based in the difficulty in finding the elastic region of the stress-strain graphs, suggests that a small amount of damage may be occurring almost immediately without significantly detrimental effect on the material strength or causing failure. It is possible that the elastic modulus could be more reliably measured using a plate-vibration tester.

Specimens with a fibre situated across a point of emerging matrix damage were found to provide some strength and to delay catastrophic failure of the material. This was seen in the literature [10], in the 3-point bending tests and also in some tensile specimens, specifically those which contained a fibre at less than approximately 45° to the applied load.

Chapter 5

Dynamic Testing

5.1 Introduction

The dynamic strain response of composite materials is of interest because it is expected to differ from its static counterparts in rate sensitivity [12] [11] as well as potentially in qualitative behaviour because of the different stress-transmission mechanics seen [8].

The behaviour of the composite has been tested at both lower and higher strain rates in the dynamic regime, using the Split-Hopkinson Pressure Bar for strain rates of around 10^3/s and a gas gun for strain rates around 10^5/s or 10^6/s.

Sufficient damage was caused to the composites to permit observations of failure modes in these loading regimes.

5.2 Split-Hopkinson Pressure Bar

5.2.1 Specifics of the SHPB System

In the SHPB used for this research, the input and output bars were composed of Inconel 718 ($\rho = 8190$ kgm^{-3}, $Z = 41300000$ kgm^{-2}s^{-1}. The striker bars available were solid Inconel (229 mm), hollow aluminium (160 mm) and partially-hollow Inconel (solid section 63 mm, hollow section 88 mm, inner radius 3.5 mm). All bars had an outer radius of 6.75 mm. These were the bars for which the system had previously been calibrated and so were not changed.

The input and output bars were both 500 mm long, with strain gauges positioned 50 mm from the sample-bar interface. Battery-powered semiconductor strain gauges were used because it had been found that using mains power introduced additional noise to the system.

The striker bar was launched down a barrel by compressed air at a driving pressure of 0.5 to 5.0 bar. Strikers were constructed to fit inside the barrel with a minimum of clearance, to ensure smooth flight, rather than using sabots [71]. The barrel of the system was equipped with a laser velocity gauge at the end, although this was not functioning when these tests were carried out. The partially-hollow could be treated as an ordinary SHPB striker. The basic SHPB setup was modified as shown in Figure 2.12.

The load steps produced by the several configurations of the solid and hollow striker bars are shown in Figure 5.1. These can be used as a reference to be compared with the results for a composite material.

The specimens used for this test, excepting the reference specimens, were machined from a single induction casting to maximise consistency. Reference specimens were machined from a piece cast under like conditions intended for microstructural comparisons. Twenty-five specimens were produced, with four reference specimens, but an equipment failure meant that there were useable records from twelve of the tests, including two reference specimens. All specimens were machined to 4mm in diameter and 8mm in length, $\pm$ 0.2 mm.

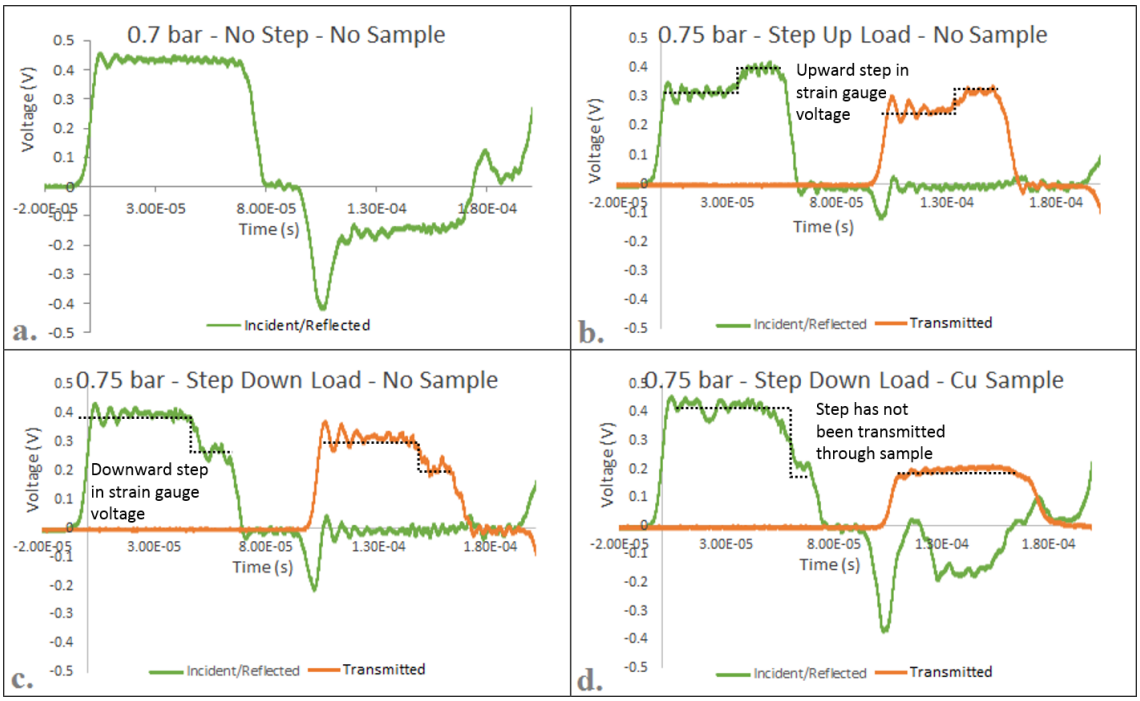

Figure 5.1: *A selection of the voltage-time traces from the strain gauges on the bars placed to either side of the specimen resulting from impacts with a solid bar, a partially-hollow bar in both step-up and step-down configurations and a stepped load through a Cu sample. The Cu sample does not show a sharp step in the transmitted wave due to its high plasticity. Data taken from [80].*

5.2.2 Testing Procedure

First, the length and diameter of the specimen to be tested were recorded. Specimens were then lubricated by smoothing a layer of petroleum jelly on to the bar ends and the specimen ends, then placed between the incident and transmission bars, as shown in Figure 2.10. The lubrication was used to mitigate barrelling by minimising friction between the sample surface and the bar ends.

The striker bar was then pushed to the rear of the gas gun barrel, the gas cylinder was brought up to the desired pressure and then triggered. The resulting pressure waves were measured by a multi-channel digital oscilloscope and exported. The oscilloscope was set to begin recording 0.1 ms before the measured spike in voltage.

After impact, the sample was recovered, marked with the test number and measured again. The bars were replaced in their initial positions and any remaining gas in the cylinders was vented to prevent accidents.

Pictures of samples pre- and post-test are shown in Figure 5.2. The x-rays show a good distribution of fibres, suggesting that the fibre distribution in the initial casts was well dispersed and that the specimens will adequately represent the properties of the material as a whole.

5.2.3 Results, Imaging and Analysis

After testing, the specimens were, with the exception of the sample sent to be x-rayed, were sectioned parallel to the loading axis, mounted in resin and polished as described in Section 3.2.1. Some samples were electropolished to highlight the dendritic structure.

Looking at the microstructure in Figure 5.3, wide bands can be seen between dendrites. These bands appear to be the result of deformation twinning [103], a phenomenon in which atoms are "shared" between two or more orthogonal crystals.

In face-centred-cubic (FCC) metals such as aluminium, twinned crystals are not usually seen until after the onset of plastic flow and are indicative of the high strain rate the material has deformed

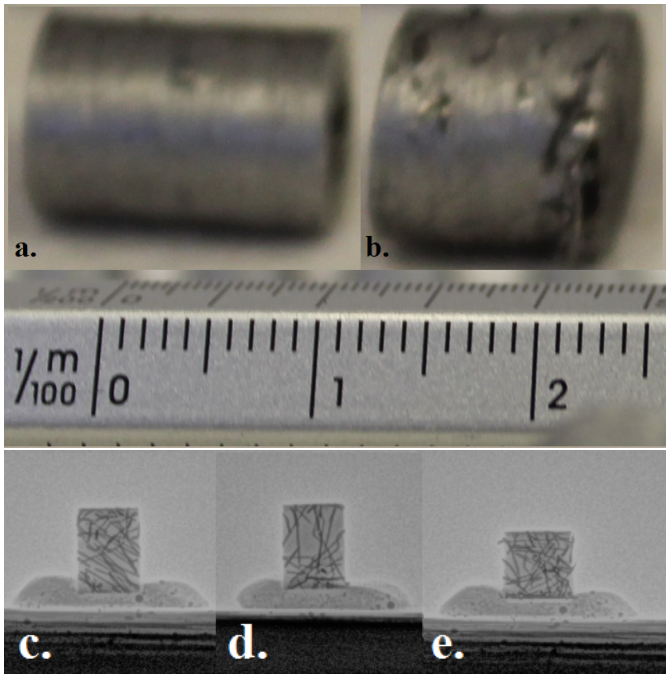

Figure 5.2: *Photographs and x-ray photographs of SHPB specimens, some of which have not been tested to serve as a visual reference. Photographs of untested (a) and post-test (b) and x-rays of untested (c, d) and post-test (e) specimens. Fibre distribution appears to be even, suggesting that they will be adequately representative of the bulk properties of the composite material. Kinking is visible on the x-ray photograph of the post-test specimen (e). The diameter of the un-deformed samples is approximately 8 cm and the length is 12 cm.*

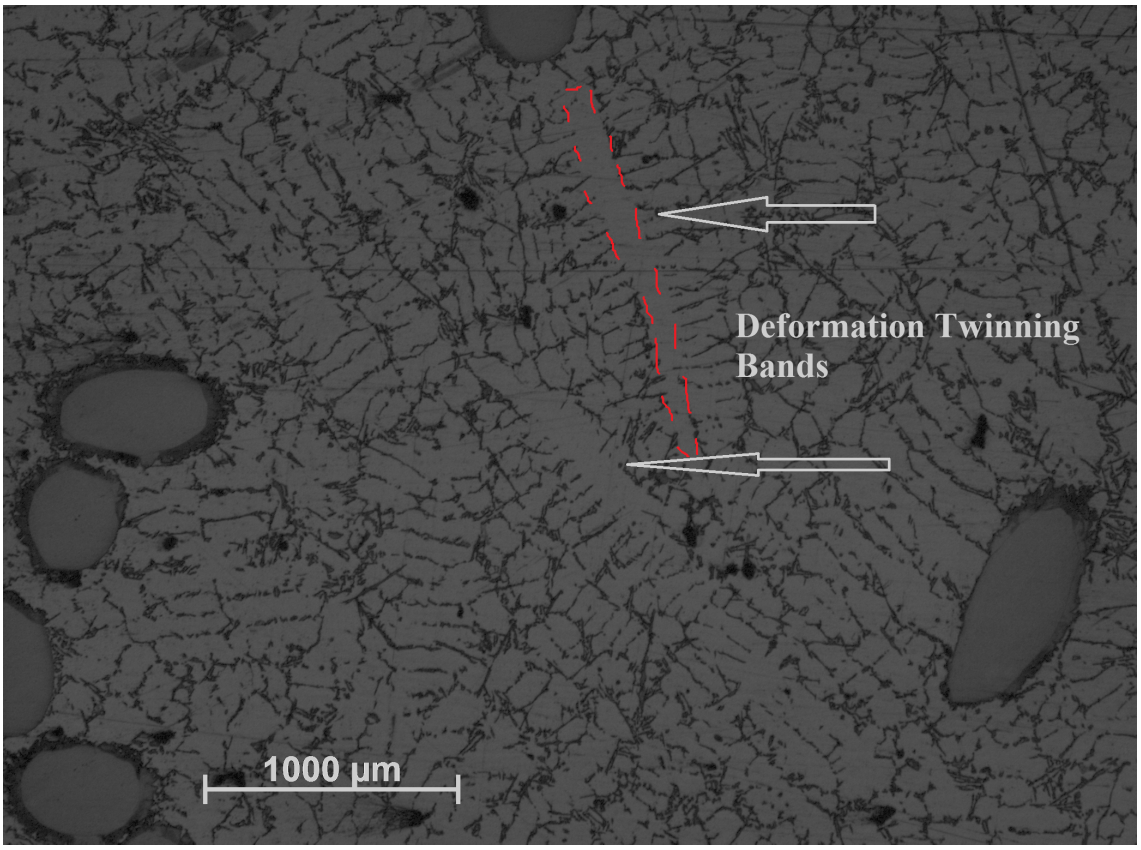

Figure 5.3: *Micrograph of a post-deformation SHPB specimen. The wide bands such as that outlined in red appear to be crystal twins induced by high shear stress or recrystallisation resulting from adiabatic heating, in which a small region is deformed so rapidly it will melt before the energy can equilibrate through the specimen.*

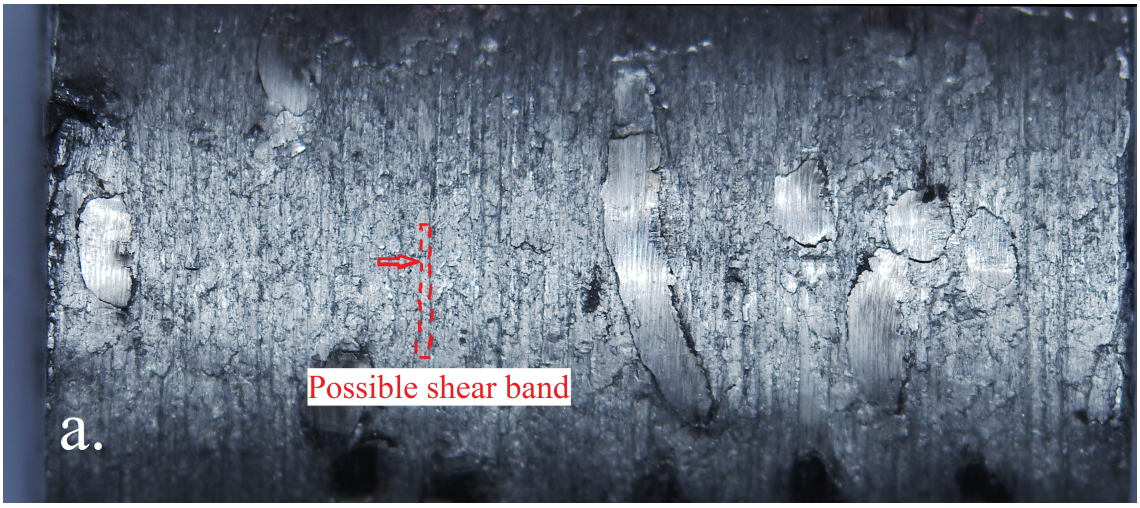

Figure 5.4: *The radial surface striations seen, such as that marked in red, appear to be adiabatic shear bands, suggesting sudden and localized failure in shear [104]. The diameter of the sample is 8.4 mm.*

in this way because it is unable to flow rapidly enough to alleviate the stress it is under. Deformation twins are often associated with phase transformations, but clear EBSD images could not be obtained to determine whether these had occurred. The twins are likely of delayed onset because there is not the sharp drop in load which would be expected from an immediate twinning [103].

Adiabatic shear bands, which form under similar conditions to deformation twins, were suggested by the circumferential striations visible on deformed samples, as shown in Figure 5.4, but could not be seen in the polished microstructures.

A possible shear band is also visible in Figure 5.2e, in the Z-shaped region of denser fibres in the upper third of the specimen.

Stress-strain curves were calculated using the Online SHPB Analysis Tool [105]. Voltage-time data were imported, the first peak region of the incident, transmitted and reflected waves were selected in the Tool's user interface and the resulting stress-strain graphs were exported to .csv files.

The stress-strain data are not to be considered entirely reliable, however, as one of the fundamental assumptions in the analysis of SHPB data is that the sample has reached stress equilibrium very

quickly on the time-scale of the test, and the large size of the samples used renders this assumption doubtful. Results are, however, of qualitative value.

Looking at graphs of peak stress and final strain vs initial firing pressure, in both cases the data suggest a very noisy linear trend. This is in line with the idea that peak stress is linearly related to applied force. Further, the stepped loads do not deviate significantly from these trends, supporting the idea that the composite removes the sensitivity of Al alloys to loading history [106] while increasing their sensitivity to loading rate. The much stronger specimen was not visually distinguishable but is thought to have contained a greater fraction of its fibres aligned parallel to the applied load.

Monolithic A357, tested by Gupta et al [107], showed a peak stress of 455 MPa and a peak strain of 55% when compressed to failure. For a strain of 10%, comparable with those reached in these tests, a stress of 410 MPa was reached. This was higher than all but one of the composite samples, which is consistent with the hypothesis that the samples had not reached their failure stress at the conclusion of the tests.

These results can be compared with those of Guden et al [11], who found that a step was formed in the transmitted wave, almost certainly as a result of the crushing of micro-voids. Additionally, while the composite showed higher strength at higher strain rates it also became less regular in its behaviour. The absence of such a step, in addition to the x-ray images, strongly suggest that any small voids or pores present in the composite were not affecting its behaviour.

Looking at the voltage-time traces produced by testing the composite under stepped and flat loads (Figure 5.7) and comparing them with those produced a stepped loading bar with no sample or with an OFHC sample (Figure 5.1) a much higher fraction the input energy has been absorbed by the composite than by the Cu, although the sample was larger, and the transmitted wave shows very little shaping, suggesting that the material is dispersing the pressure front as had been hoped.

Some sectioned samples were further examined under electron microscopy. Shown in Figures 5.8, 5.9 and 5.10 are images and linescans of a fibre which has failed under shear, deforming from a straight line into an N-shape. This will be a highly energy-absorbing failure mode, involving plastic flow of both matrix and fibre.

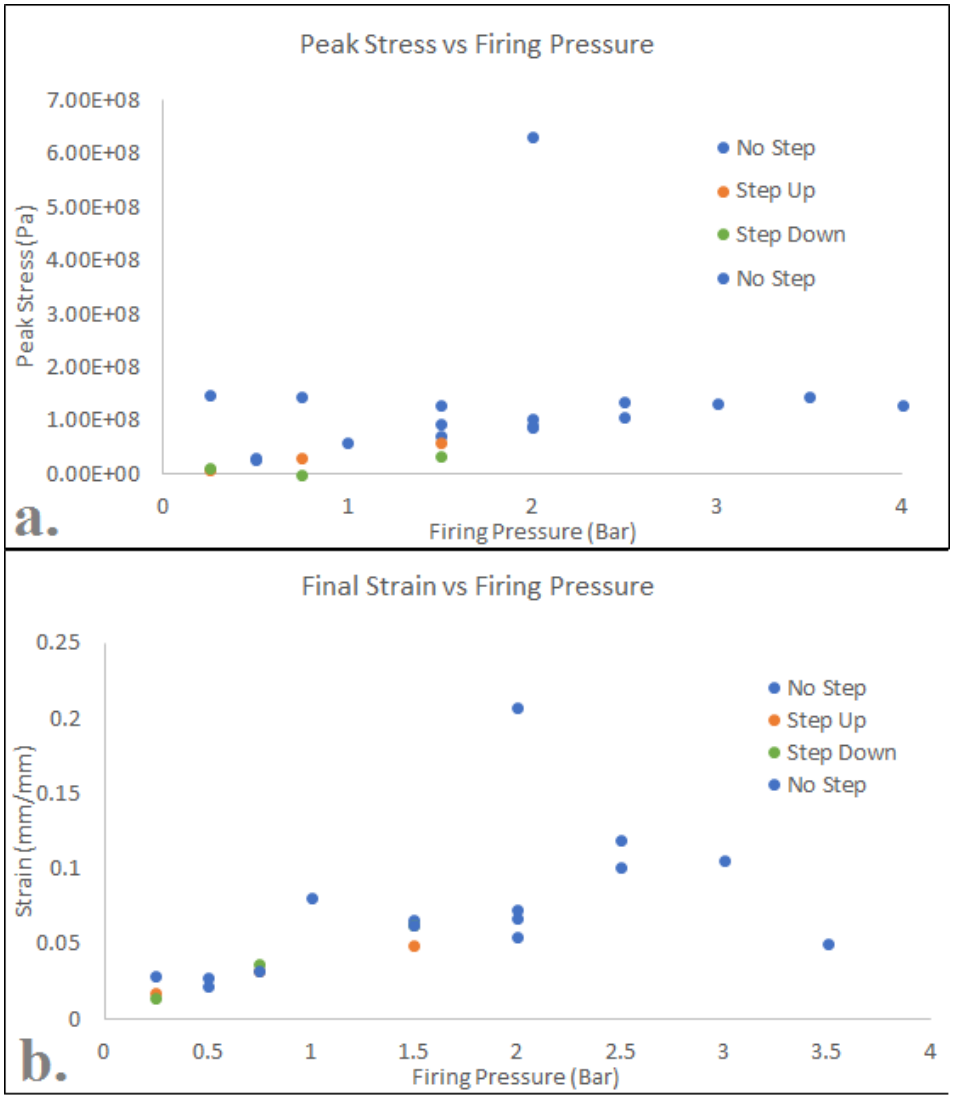

Figure 5.5: *Correlating peak stress and final strain with initial firing pressure from the gas cylinder, a noisy linear trend can be seen. The stepped loads fall consistently within the lower bound of the range for each firing pressure.*

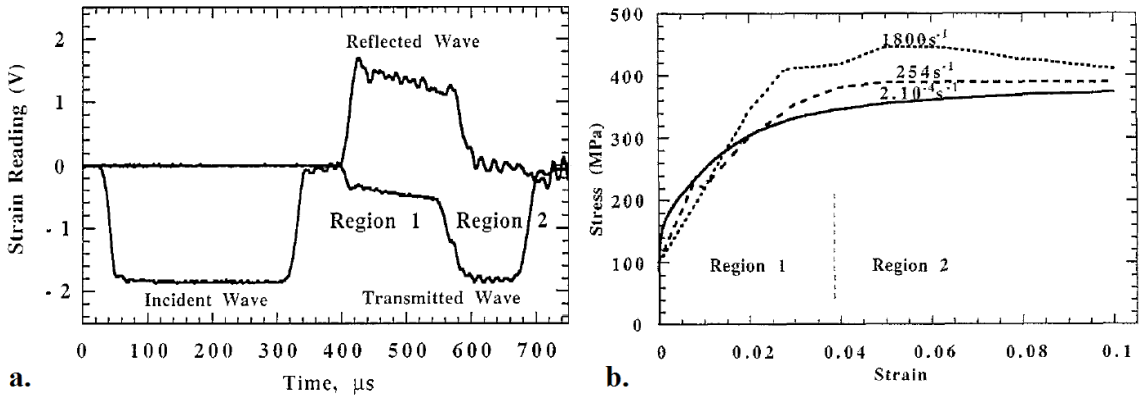

Figure 5.6: *Voltage-time and stress-strain curves for an SiC-reinforced MMC, measured by Guden et al [11]. A "smearing" of the reflected and transmitted waves is seen, as is a step in the loading profile. This may well be due to an initial compacting phase in which all voids were crushed out of the composite.*

High-resolution scans of the elemental composition were taken at two points on the fibre-matrix interface, indicated in Figure 5.8. The regions were chosen to highlight the difference between areas with low and high shear damage.

In the less damaged region (Figure 5.9), there is still some possible fragmentation of the interfacial region, but the chemical composition does not show any obvious damage, suggesting that the matrix flowed with the fibre when the shearing occurred.

In the more damaged region (Figure 5.10), there has been visible cracking of the intermetallic compounds. This area is at the edge of the delaminated zone. The suggestion on the linescan of higher oxygen concentration at the cracks indicates that they are not only surface phenomena.

The SHPB allowed significant compressive damage to be observed, and new damage types to be seen. Shear bands and deformation twinning were both present, neither of which had been observed in quasi-static compression tests. A contrast can be drawn between the HMMC behaviour, in which failed fibres had sheared and deformed, and MMC behaviour [11] in which failed fibres had snapped.

Looking at the peak stresses and cross-sections of tested specimens, it is plausible that the SHPB

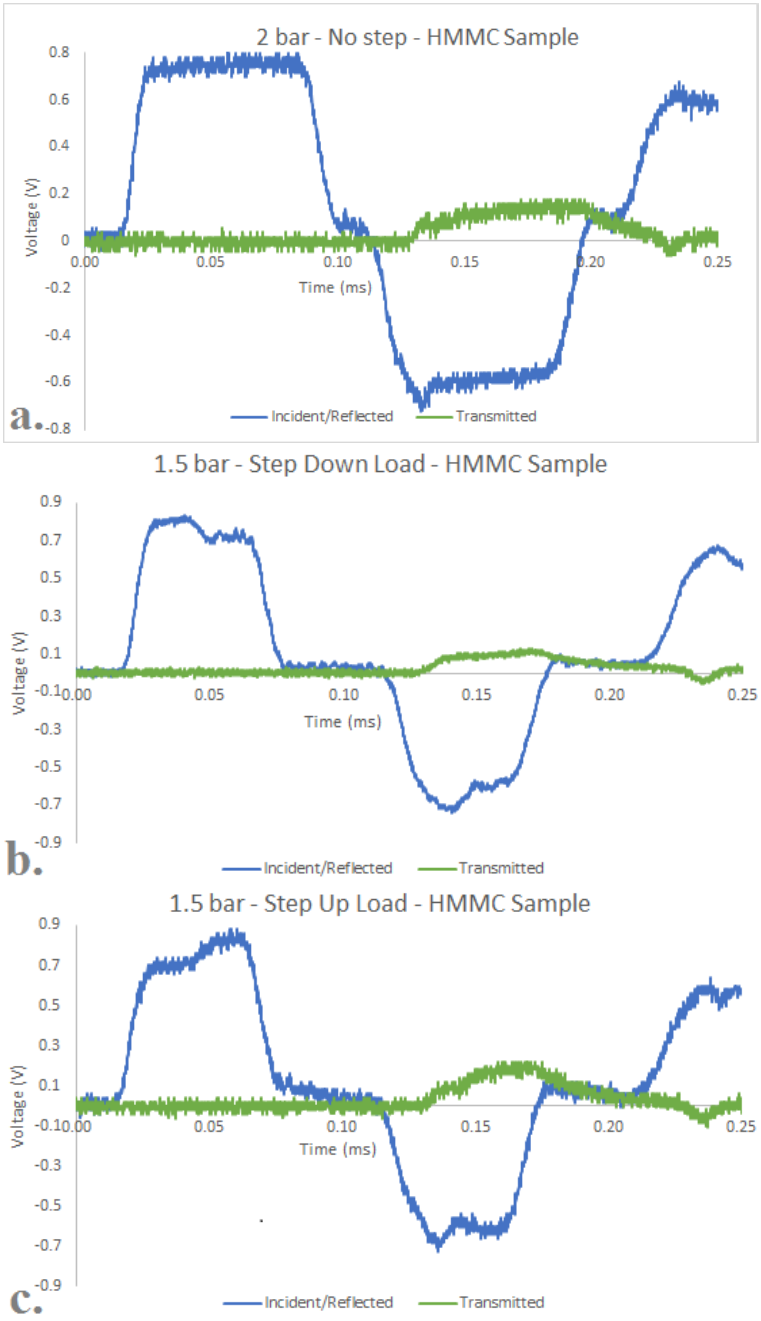

Figure 5.7: *Voltage-time traces from the strain gauges either side of composite samples under stepped load, as applied in Figure 5.5, showing the undetectability of the loading step at the strain gauge placed after the specimen. The poor definition of the transmitted wave suggests that the composite has absorbed most of the energy imparted to it, indicating its success at dissipating the additional pressure.*

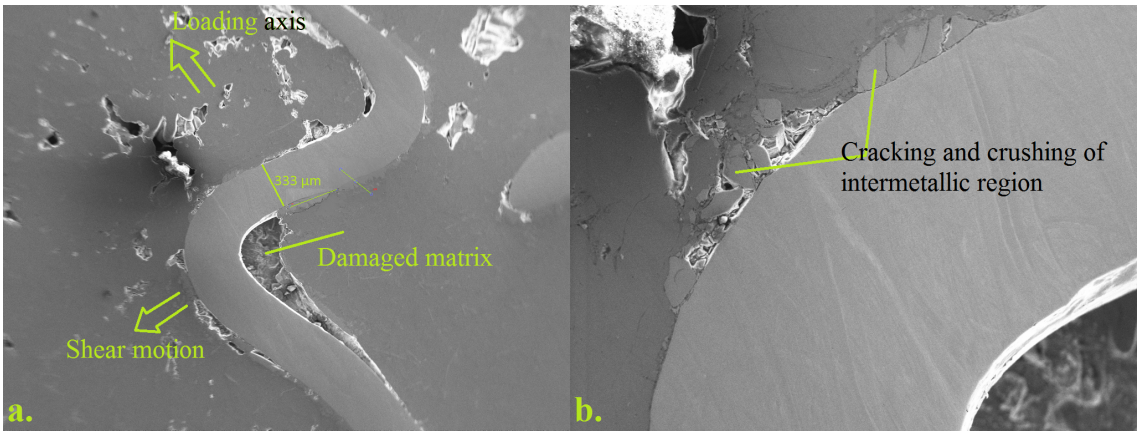

Figure 5.8: *SEM pictures of a damaged region of composite showing a "kinked" fibre, which has failed in shear. In addition to the plastic flow of both matrix and reinforcement, there has been damage to the brittle intermetallic compounds, seen on the right.*

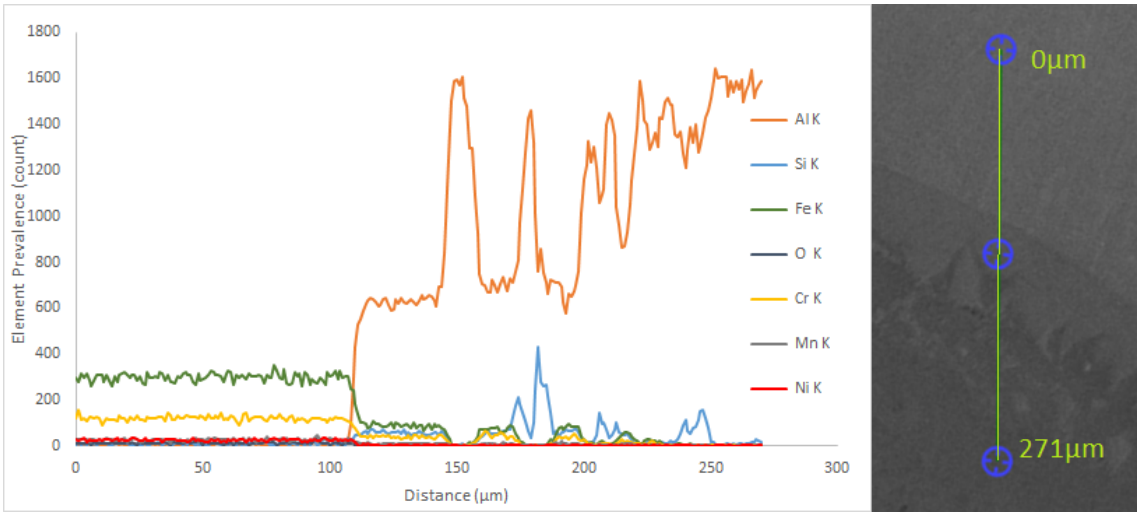

Figure 5.9: *SEM linescan of a damaged region. There is little damage to the interfacial region visible here, and the linescan resembles those in Section 3.3.2.*

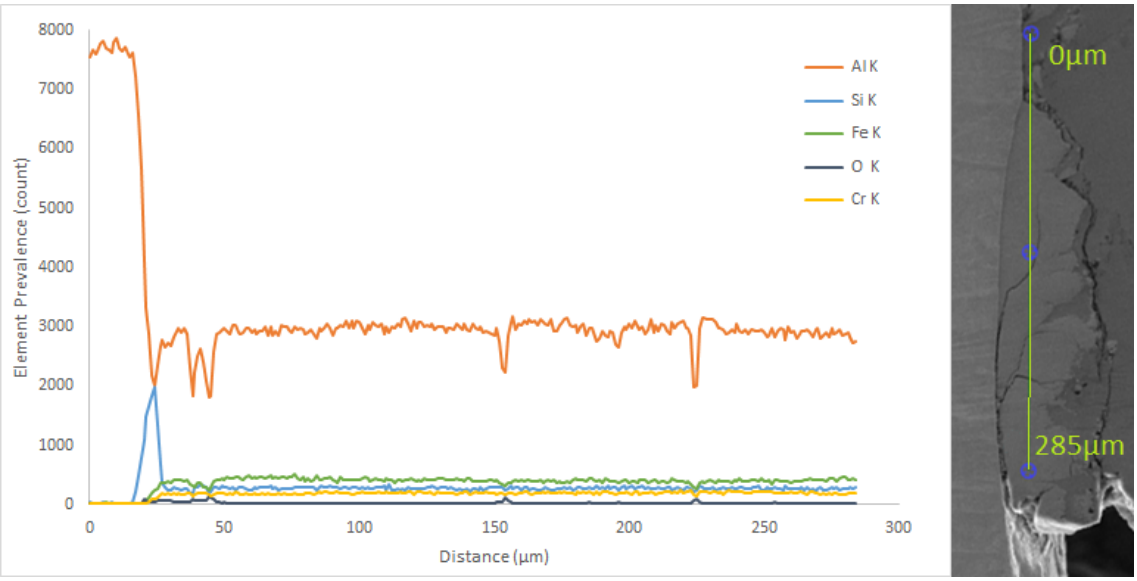

Figure 5.10: *SEM line-scan of a damaged region. This region is on the inside of the N-curved section of fibre. The oxygen spikes visible at the cracked sections are thought to be either an artefact of the air present or of the absence of other elements.*

has not compressed the specimens to failure. The fragmentation, internal voids and substantial lateral buckling of fibres seen in the quasi-static compressive tests were not seen here.

While the quantitative values obtained for peak stress are not to be relied upon, the qualitative trends seen are in fair agreement with the literature.

5.3 Ballistic Testing With Gas Gun

Gas gun tests were chosen because they reach very high strain rates, on the order of 10^6/s, and because if they are done with a small pellet then they give insight into the ballistic response of a material. It was expected that materials of this type would provide interesting ballistic properties because of their unusual load response mechanisms.

A gas gun of this type uses high-pressure gas to propel an impactor into the sample at very high velocities. The gun used in this research was based at the Institute of Shock Physics at Imperial

College London.

The pressure was regulated with Mylar (a polyester resin) sheets of designated thickness: the sheets would burst once a designated gas pressure was reached, creating a very sharp pressure pulse which accelerated the projectile.

The specimens were machined from induction-cast composite pieces to 100 mm diameter and 15 mm thickness, except the SiC MMC reference piece, which was 5 mm thick because of casting problems. Twelve test pieces were used, of which one was a 15 %wt SiC piece and one was a combination 15%wt SiC and 10 %wt fibre composite.

Because of the very high velocity of the projectile, it was important to follow a strict procedure when setting up and firing the gas gun. A schematic of the gas gun layout is shown in Figure 5.12.

First, the projectile was prepared. The impacting projectile was attached to a plastic flyer with two circumferential rubber O-rings. For large impactors, the impacting plate was glued to the flyer with cyanoacrylate. For small pellet impactors, a metal plate with a small central hole was glued to the flyer and the pellet was then secured inside the hole by a small amount of vacuum grease. The combined flyer and impactor were then weighed and placed to one side ready for insertion into the gas gun barrel. Photographs of the impactors before and after use can be seen in Figure 5.11.

For all but the last test, the projectile was mounted in a "guide" flyer or sabot, which was prevented from impacting the sample by the sabot stripper. The final test used a plate impactor.

The sabot system is used for small projectiles because the gas gun barrel is very much larger than the projectile, meaning that any asymmetry of loading or acceleration would cause the projectile to hit the walls of the barrel rather than the sample. The sabot was designed to be of the same diameter as the barrel, ensuring axial acceleration.

It was then necessary to prepare the Mylar sheets. The sheet thickness, between 25 μm and 100 μm, was selected and two octagons of approximately 3 cm per side were cut. The size of the octagons was chosen to fit between the pair of O-rings used to ensure the breech is sealed.

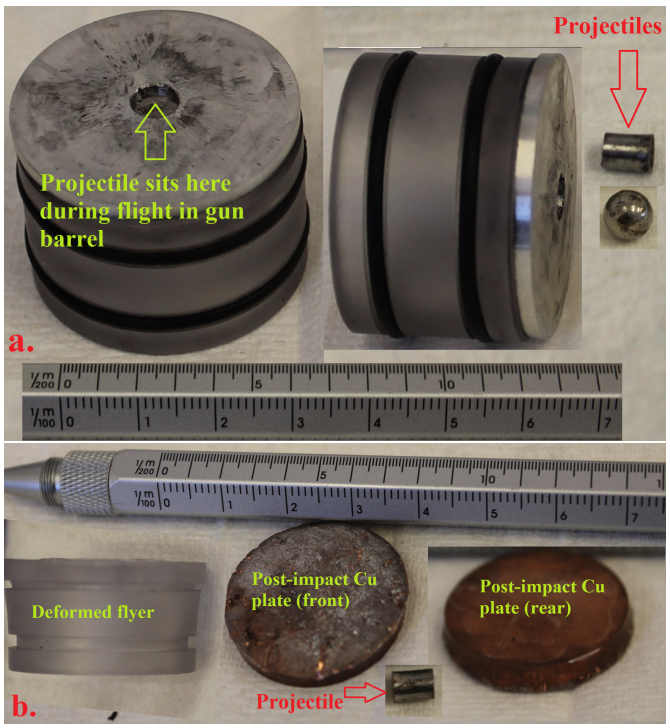

Figure 5.11: *Images of flyers and projectiles from the gas gun (a) before impact, showing the cylindrical and spherical flyers next to the sabot which ensured straight flight down the gas gun barrel before impacting the sabot stripper and leaving the projectile to impact the specimen. (b) after impact, the sabot had been significantly damaged by impact with the sabot stripper. The cylindrical projectile has also visibly deformed, and the heavy Cu plate used to break a sample has been substantially damaged by the impact.*

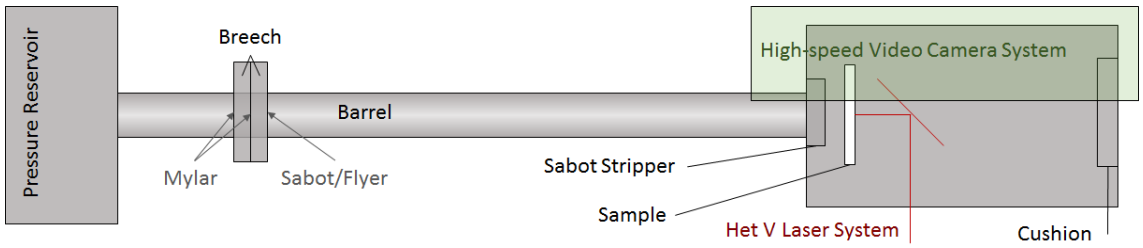

Figure 5.12: *Schematic diagram of the gas gun layout. Pressure was built up in the reservoir, then released through a valve into the barrel, where a pressure pulse was created by a pair of Mylar sheets at the breech which would burst when the desired pressure was reached. This pressure pulse would then accelerate the flyer, which would be stopped by the sabot stripper leaving the projectile to impact the sample. The instantaneous velocity of the rear surface of the sample was measured by a laser Het-V system and the projectile velocity was tracked using a high-speed camera system.*

The breech was then opened and the flyer inserted into the barrel, after which the Mylar secured in place with vacuum grease and the breech was re-sealed. The seal was then inspected to ensure it had been sufficiently fastened.

The test specimen was held in a mount within a large acrylic box. In addition to the sample and mount, the box contained the sabot stripper and the mirrors for the heterodyne velocimeter (Het-V), as well as some cushioning materials to prevent debris from causing damage. The sample box was constructed from clear acrylic in order to permit high-speed video recording of the impact.

The sabot stripper was used to prevent the flyer impacting the sample along with the small pellet, and was constructed from alternating aluminium and rubber plates mounted to studding with with nylon nuts and containing a small central hole through which the pellet could move.

The Het-V system was composed of an infrared laser and a modified Michaelson interferometer. The (metallic) sample forms one mirror of the interferometer, meaning that the interference pattern will depend on the Doppler-shifted frequency of the reflected light. Since Doppler shift is determined by the velocity of the moving object, the frequency of the light at the detector will be linearly dependent on the speed of the sample.

The next step in the shot preparation process was to put the sample into the mount and check that the Het-V system was properly aligned and the sabot stripper was in place. Once this had been done, the acrylic box was bolted shut.

Then, after any persons in the lab had moved to a safe area, the gas cylinder was slowly pressurised. When it had reached the desired pressure, the gas was evacuated into the gun barrel, bursting the Mylar sheets and firing the flyer.

After the shot had been fired, the infrared laser would be deactivated and the sample box and breach would be opened and cleaned, and any necessary repairs would be made, before setting up for the next shot.

The gun was instrumented in three places: the firing pressure was measured at the gas storage bottle, the velocity of the back of the sample was measured using heterodyne velocimetry (Het-V) and the impact itself was recorded using a Phantom high-speed camera.

The projectiles used were primarily steel cylinders 6 mm long, 4.5 mm in diameter and approximately 1 g in weight. Some spherical projectiles 6 mm in diameter and 1 g in weight were also used, and for the final shot a copper disc 26mm in diameter and 4 mm high weighing 17 g was used in (this impacted the sample whilst still connected to the flyer, for a total impact weight of 34 g and an estimated impact energy 16 times higher than the small projectiles).

The specimens being tested were discs 75 mm in diameter and 15 mm thick, except the MMC reference disc, which was only 5 mm thick because of casting defects in the ingot. the diameter was chosen to fit into the most commonly used gas gun mount, to minimise potential issues. 15 mm thickness was chosen to ensure that most of the specimens survived impact and to be easily machined from the as-cast ingots.

5.3.1 Results, Imaging and Analysis

After being tested, specimens were measured, photographed and then sectioned through the thickness of the disc. Half of the impact crater was mounted for microscopic imaging; the other half was flattened for hardness testing.

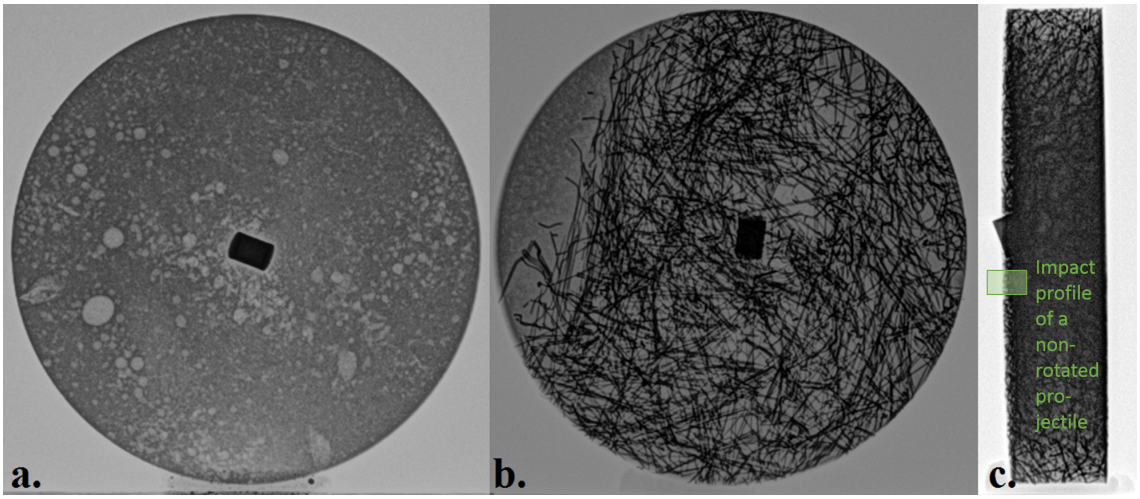

Figure 5.13: *X-ray photographs of an MMC sample (a) and an HMMC sample (b,c). The paler bubbles visible in the MMC are air rather than SiC agglomerations. An ingot edge was visible (left side of the centre image) on both the x-rays and the outside of the sample. The embedded projectile has rotated almost 90° to the impact axis.*

Some of the specimens were sent for x-ray imaging. A selection of the resulting images is shown in Figure 5.13. The fibre distribution is satisfactory except at the ingot edge, which was well away from the test region and was visible from the outside of the sample. Unfortunately, the fibre network is too dense to study the deformation caused by the pellet impact.

Computed tomography (CT) imaging as described above was attempted but did not yield usable images. The minimum vertical resolution for a sample of this diameter was 1 mm between slices, which was too large. Additionally, for images with an embedded pellet the contrast between fibres and matrix was not sufficient to see details.

A great deal of the material response to high-speed pellet impacts can be learned from the impact crater. For this reason, the craters were visualised by electron microscopy, optical microscopy before and after electropolishing, and by a 3-D camera on loan to the department.

When looking at the orientation of the craters, most were distinctly rotated about the impact axis. This is thought to be due to uneven resistance from the target, slowing the projectile by different amounts across its impacting face and leading to rotation. This rotation, known as “tumbling”, is

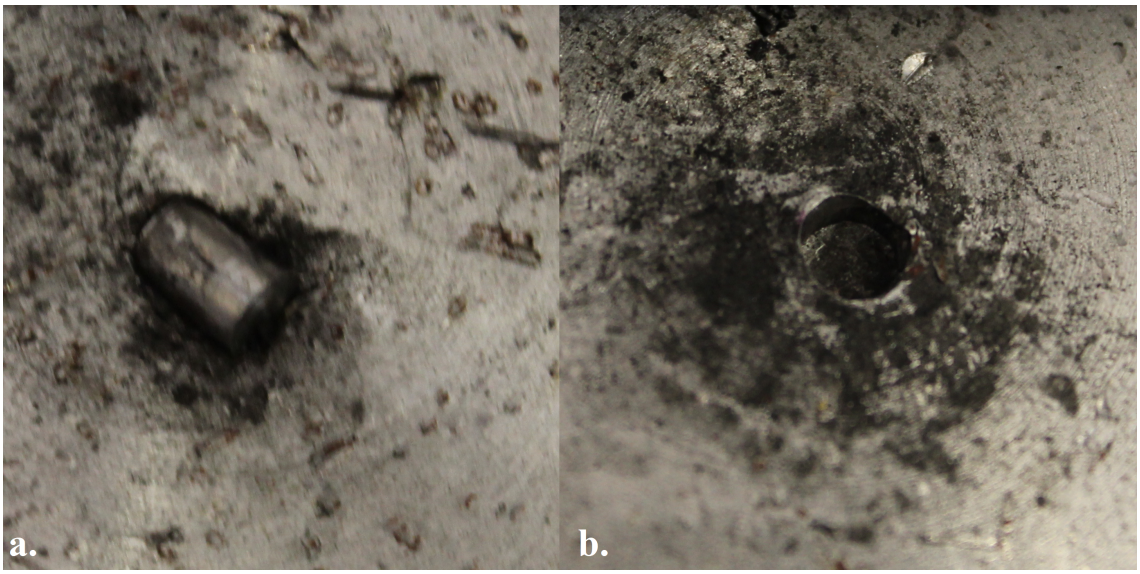

Figure 5.14: *Two images of the projectile impact sites showing the differing degrees of tumble experienced by the projectiles. Tumbling is caused by the differences in strength and stiffness of the matrix and reinforcement, which changes the resistance to projectile impact across its impacting face and thus the penetration speed of the two sides.*

a valuable property for ballistic resistance, as it substantially decreases the penetration depth for a projectile with a given kinetic energy. Examples of this are shown in Figure 5.14.

No spall damage was observed in any of the specimens. Since the projectiles were flat cylinders rather than sharp-tipped bullets, this effect will have been exaggerated compared with real-world ballistic performance but the results remain promising.

Looking at the 3D camera image of an impact crater (Figure 5.15) with fibres visible at the surface, the fibres have twisted and deformed into the crater. This will be a very energy-absorbing deformation route, and there is also some suggestion that the different flow stresses of the material have been significant, as the fibres are slightly raised and debonded from the matrix at the base of the crater.

Shock impacts produce several deformation zones, described in [108] [109] among others as radiating outward from the impact site as a vaporisation zone, a melted zone, a “shocked” zone with high shear and plastic flow, and a bulk deformation zone.

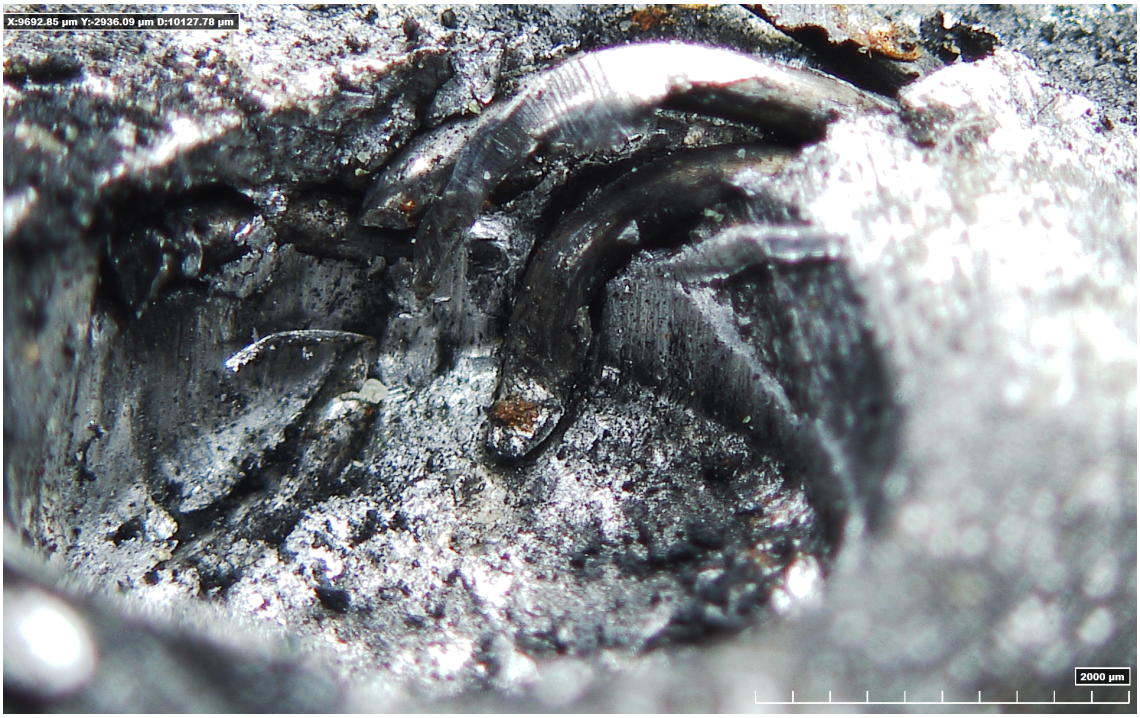

Figure 5.15: *Two images of the projectile impact sites showing the differing degrees of tumble experienced by the projectiles. Tumbling is caused by the differences in strength and stiffness of the matrix and reinforcement, which changes the resistance to projectile impact across its impacting face and thus the penetration speed of the two sides.*

In this work, the shocks produced were not large enough to cause melting or evaporation, but there is significant evidence of a distinct "shocked" zone very close to the impact site. The crater ridge in Figure 5.15, the nature of the cracks in Figure 5.16 and the drop in hardness very close to the crater edge all suggest a small region which has deformed differently to the bulk.

The crack propagation is unusual in that cracks are present but are very short. A branching crack next to very severe deformation would be expected to propagate some distance into the matrix if it did not break the specimen outright. It is hypothesised that the crack has propagated to the edge of the shocked zone and been halted by the hardened material in the bulk deformation zone.

The proposed mechanism for this is that the crack propagation speed would be expected to be lower than the sound speed in the matrix, and so the shock (and thus the hardening it has caused) would precede the crack tip. Since the shock front and crack are both formed at impact, there will be a region in which the damage precedes the compression, forming the shocked zone. The drop in hardness at the very edge of the crater described below supports this hypothesis, and it is consistent with the description of shock propagation in A356 by Peyre et al [110].

The images and SEM linescans presented below are all from the same specimen, an HMMC impacted by a cylindrical projectile at 300 m/s (40 bar firing pressure). The cylinder showed significant tumble and two damage zones are suggested.

Electropolishing the specimen as described in Section 3.2.1 significantly increased the contrast of inclusions and alloying elements in the aluminium. Comparing their density with that of undamaged material, it is possible to visualise the effects of the pressure pulse on material which has not been macroscopically damaged.

From Figure 5.17, it is possible to see that the material has been very strongly compressed in a band near the crater edge, and is most strongly concentrated in the corner region at the bottom of the crater as oriented in Figure 5.17, but the specimen had not been substantially affected 500 μm from the impact site.

Given both the very localised damage seen and the very high plastic flow around the impact site, it seems plausible that the shock has induced superplastic deformation. Superplasicity is defined

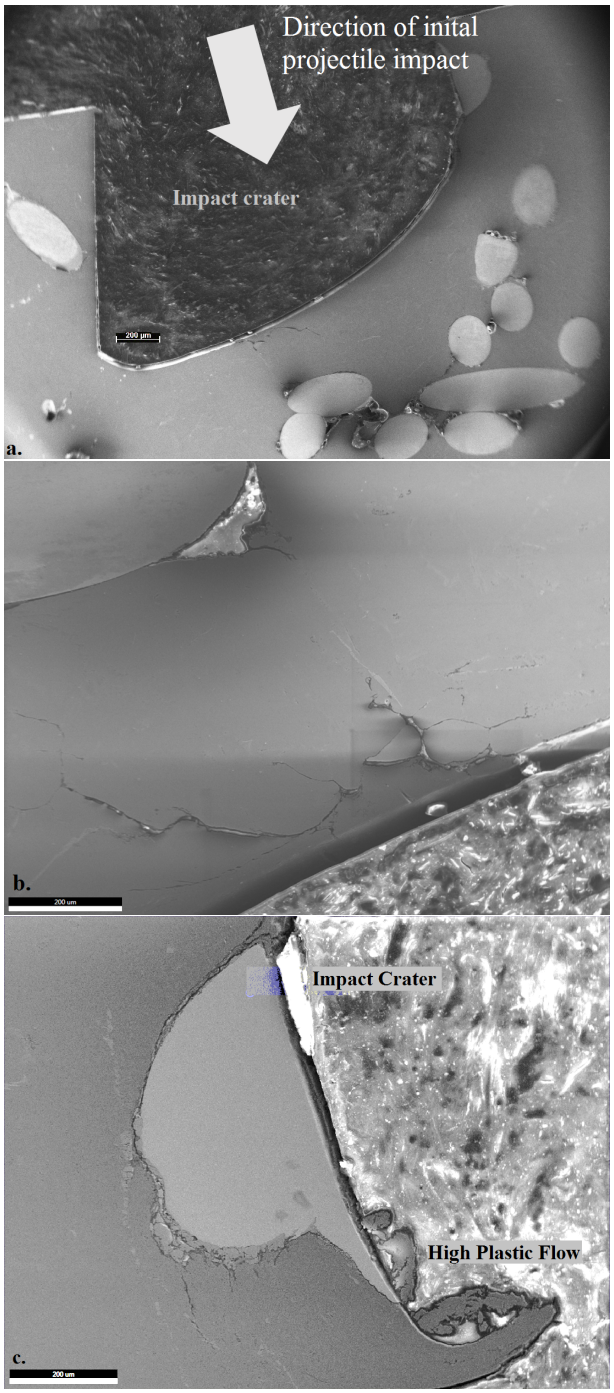

Figure 5.16: *Three images of the crater of a 40 bar impact. Specimen has been sectioned parallel to the impact axis to produce a cross-section of the crater. (a) a view of the entire crater; (b) a close-up on the cracked region; (c) is a close-up of the plastic flow at a crater edge. The rotation of the impacted projectile can be seen from the profile of the crater: instead of being square, it has a curved edge. The vortex of matrix at the crater edge is indicative of the very high plastic flows associated with shocks.*

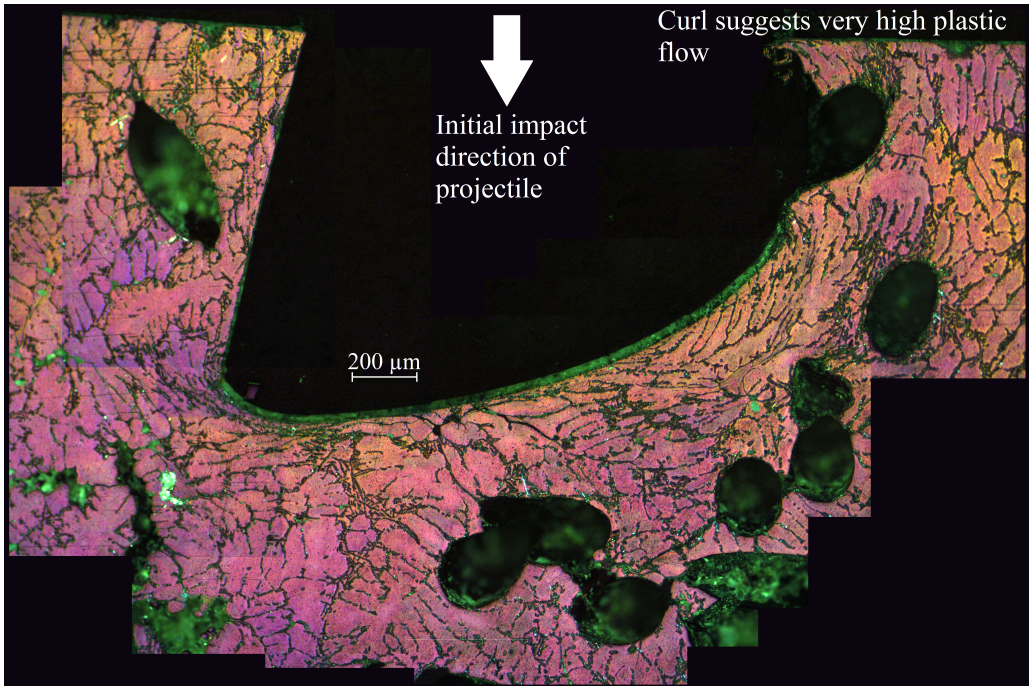

Figure 5.17: *Composite microscope image showing the entire damaged section of a sample after electropolishing. A region of extremely high plastic flow can be seen at the crater edge. The specimen was electropolished to attempt t oexamine the grain structure with increasing distance from the impact crater, but this was not visible. However, the dendrites which are deformed around the impact are seen with high contrast in this image.*

[111] as plastic flow much in excess of what would usually be expected for a crystalline material, without causing necking or cracking.

Superplastic flow has been observed in Al alloy/ceramic composites with a larger grain size than in monolithic Al alloys [111] and over a higher range of strain rates.

Examining the SEM scans of specific regions, the superplasticity and damage localisation ideas are supported by the very small amount of cracking visible and the small size of these cracks.

Examining the cracks in the matrix, more Si was found at the crack edges, suggesting that the crack is propagating along crystal boundaries. In addition, a β-phase Al-Si platelet is present precisely at the crack in the Figure 5.18, which may well have nucleated the crack.

Looking at the fibre-matrix interfaces in Figure 5.19, the first fibre at a distance of around 300 μm from the impact crater is not showing any anomalous behaviour. The region contains a small trapped air bubble or shrinkage pore and shows Si segregated to the fibre/matrix interface. The second region shows no interfacial material, suggesting that the impact was against a surface fibre exposed by machining. The very bright region appears to be highly compressed aluminium. This may have flowed across the fibre during initial compression. The very bright sliver of Al visible between the fibre edge and the mounting resin in Figure 5.19b may be coloured as it is because it has been so compressed.

The fibre-matrix interface close to the upper tip of the crater edge (Figure 5.20) showed extremely noisy data with a very low element count. This suggests that the crack was wider than the scanning beam, and that the interface contained the same Al-Fe-Si-Cr compounds described in Section 3.3.2.

The last specimen to be tested, using a firing pressure of 24.1 bar and a 34 g copper plate-fronted flyer, broke entirely, as had been intended. There were four large pieces, shown in Figure 5.28, and several very small fragments. The impact energy in this case was 16 times higher than the average of the small projectile tests.

The shape of the fracture surfaces on this specimen, shown in Figure 5.21b, indicates that the failure mode was brittle rather than ductile. The protruding wires failed in pull-out rather than

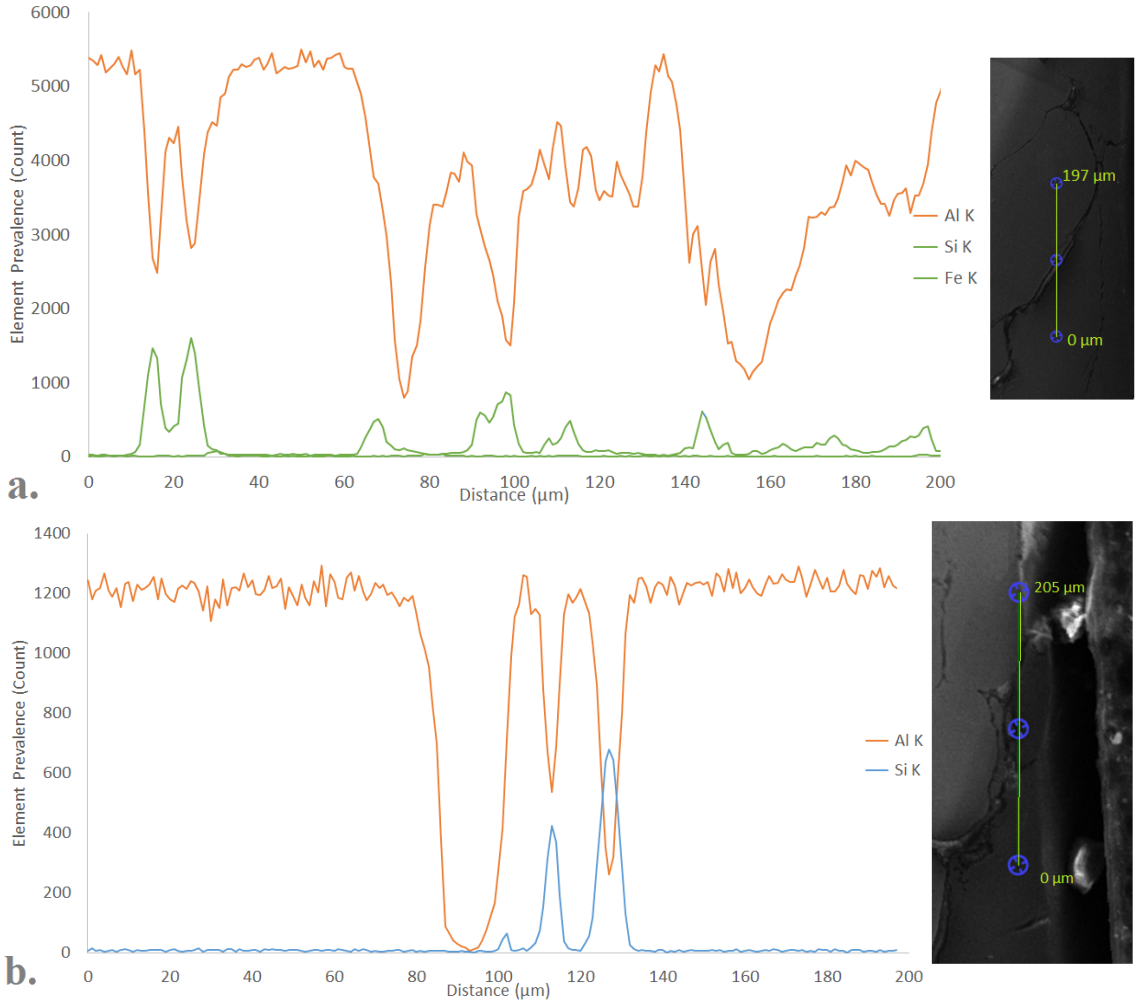

Figure 5.18: *A scan of two sections of the crack reveals more silicon at its edge, suggesting that the more brittle Al-Si compounds have nucleated damage. A β-phase AlSi platelet appears to be visible in the top image.*

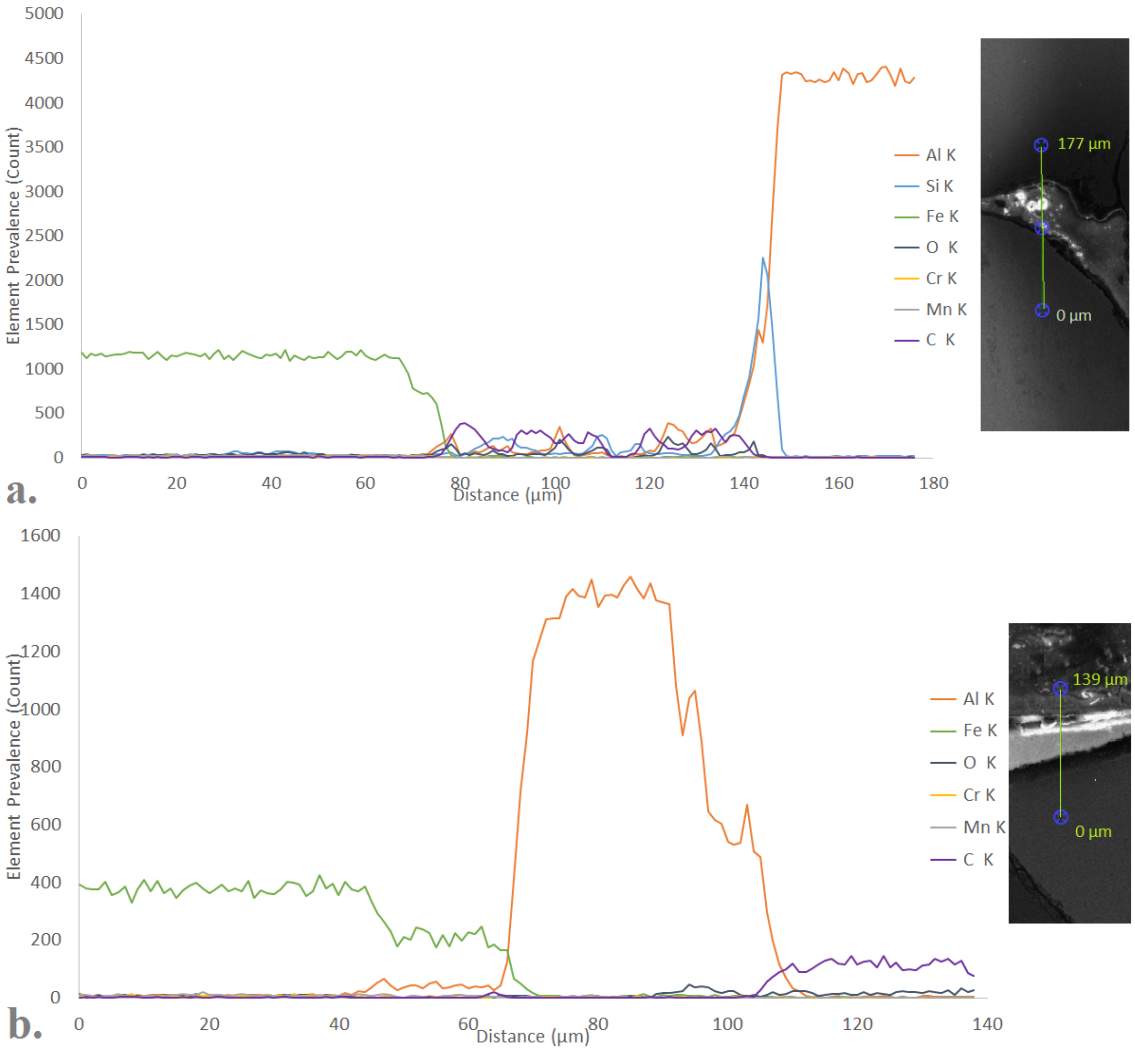

Figure 5.19: *A scan of the fibre-matrix interface close to the damaged zone (a) and of the fibre and matrix at the edge of the crater (b). Aside from the presence of a small pore, the interfacial region at a distance from the crater is not unusual.*

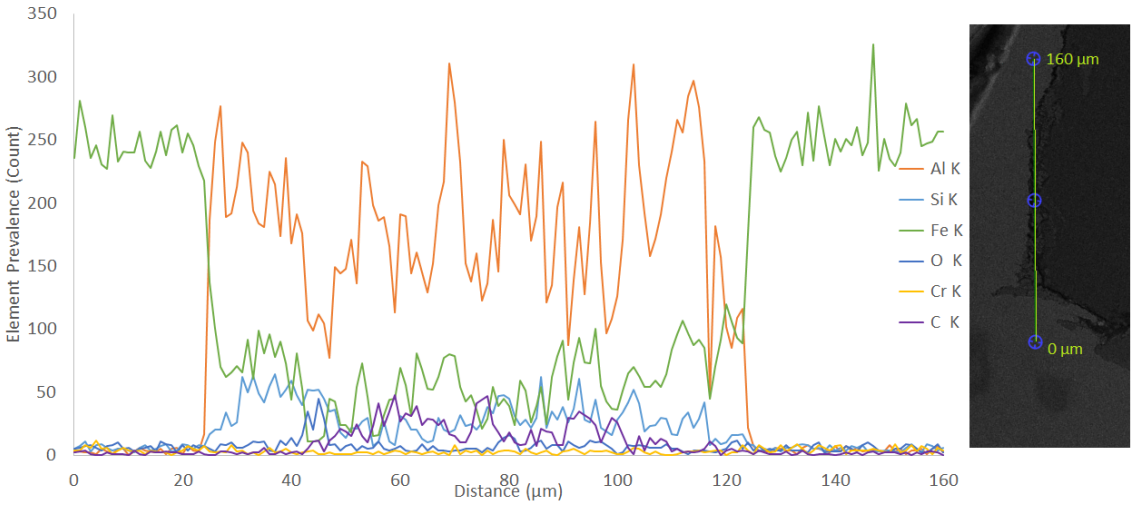

Figure 5.20: *A scan of the crack between the fibre at the crater edge and the matrix below. The noisiness of the readings suggests that the crack is wider than the beam scanning tip.*

fracture. The difference in shape of the front and reverse sides of the specimen lends support to the shock-dissipation theory.

It is also worth noting that although the damage is extensive, with cracking throughout the specimen, there is a clear region of localised extreme damage and no spallation is apparent on the rear surface. This is consistent with the hypothesis that this material does not transmit a pressure front smoothly, as it is the reflection of the initial pressure front at the rear surface of the specimen, and subsequent compression-rarefaction band, that causes spall damage.

Heterodyne velocimetry, also called photon doppler velocimetry, is a technique for precisely measuring the velocity of an object using commercially available laser systems. A laser beam is split, half is reflected from the target object and the reflected beam is then interfered with the other half. If the target is moving, Doppler shift will change the wavelength of the reflected bean half and the interference pattern seen at the detector will be related to the new wavelength and thus to the velocity of the object.

Analysis of the data gathered was performed using the "Het V tool" developed at Imperial College London [112]. It automatically performs a Fast Fourier Transform and outputs the data as a colour map, with intensity related to strength of signal. Plots are shown in Figure 5.22.

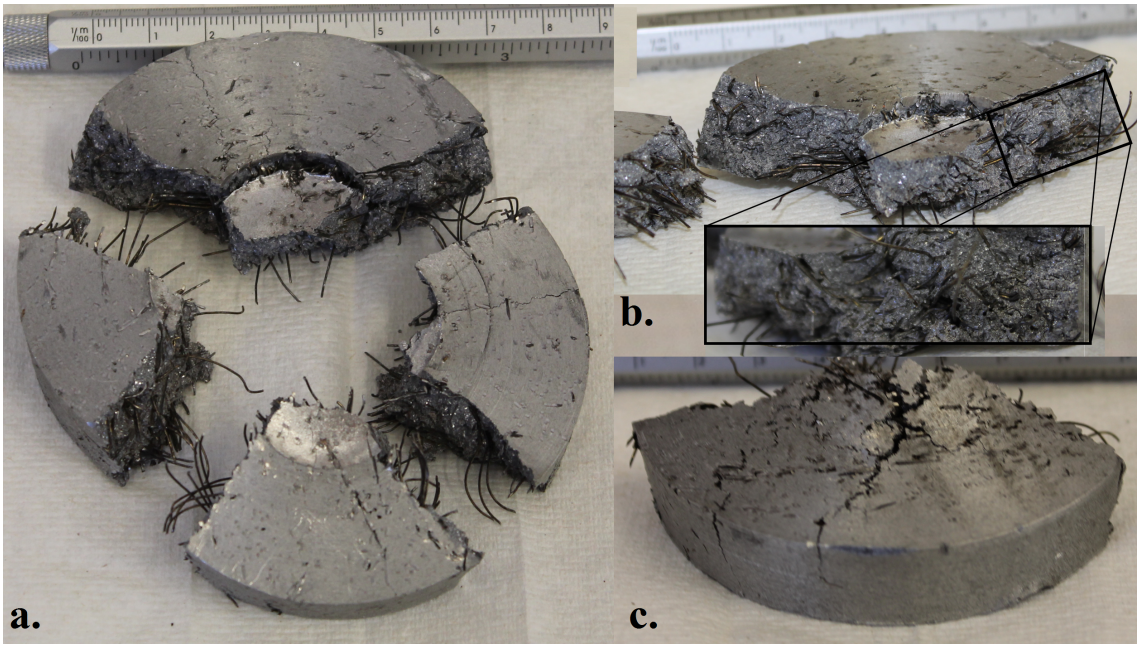

Figure 5.21: *Photographs of the plate impact specimen after it had been entirely broken. (a) all the largest pieces reassembled as they would have fit together. (b) Close-up views of one of the fracture surfaces. (c) the reverse side of the largest single piece. When first recovered, the specimen was held together in some places by the fibre network but this did not survive removal from the specimen box. The estimated impact energy was 16 times higher than that of the small projectiles.*

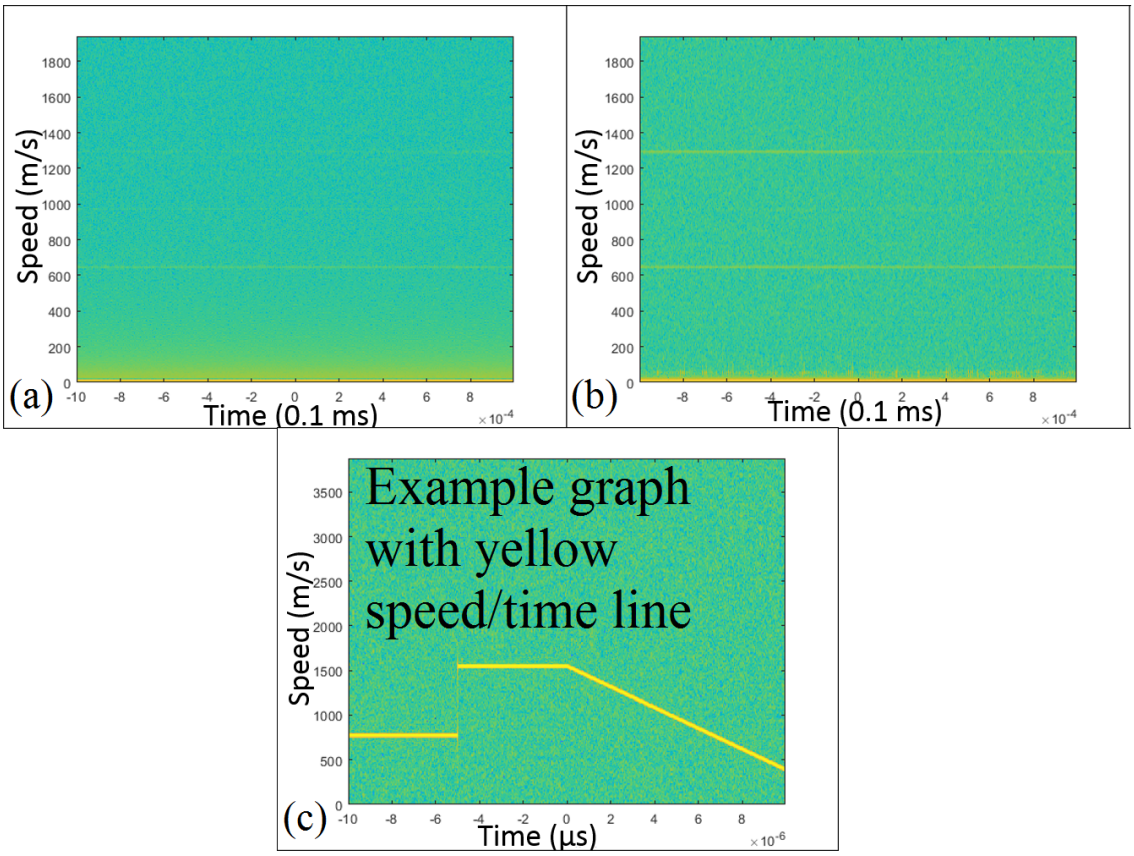

Figure 5.22: *(a) velocity-time data from a 9.5 bar impact. (b) data from a 31 bar impact. (c) example data from the analysis tool. The example graph shows a thick yellow line indicating the speed-time behaviour of the example projectile. The experimental graphs do not show any such line, suggesting that there was a problem with either the interferometer or the oscilloscope. No useful velocity information can be gained from the Het-V instrumentation used during the tests.*

Unfortunately, the data gathered could not be analysed to determine the velocity of the specimen. Different sampling windows (Hann, Hamming, Boxcar and Nuttall) were attempted without effect. It is suspected that the fault was with either the settings on the oscilloscope or the alignment of the laser system.

The impact speed of the projectile was calculated based on the number of frames taken for the it to traverse a set distance on the high-speed video taken of every impact. Since the particles were frequently supersonic when exiting the gas gun barrel, they would create a region of glowing air when entering the still air of the specimen box which obscured the precise location of the impactor.

Penetration depth of the projectile was plotted against the speed and kinetic energy of impact, shown in Figure 5.23. While kinetic energy provides a better linear fit, neither was very strong. Given the inaccuracy of the velocity determination, and that the kinetic energy of impact is proportional to the square of the velocity, and that this is the better fit despite the presumably magnified error, the penetration depth is hypothesised to be proportional to the impact energy rather than impact velocity.

The performance of the A357/10% wt Dramix 80/30 BP fibre (Orange points in Figure 5.23) was found to be less than twice as strong as the A357/15% vol MMC. An additional comparison was made with a composite was manufactured with both SiC and fibre reinforcement, but the fluidity of the MMC was so low that large casting voids were found. Although large voids were not present in the test region, as confirmed by the sectioning of the specimen after it had been tested, poor infiltration is suggested as a reason that the material performed comparatively poorly, as shown by the red data points in Figure 5.23. It is also possible that different chemical availability of Si and Al changes the nature of the interface in a detrimental way.

5.3.2 Work Hardening

In this case, the Vickers hardnesses were chosen because the maximum size difference between indents was approximately 30%, whereas for Brinell hardnesses it was less than 1%. Further, the

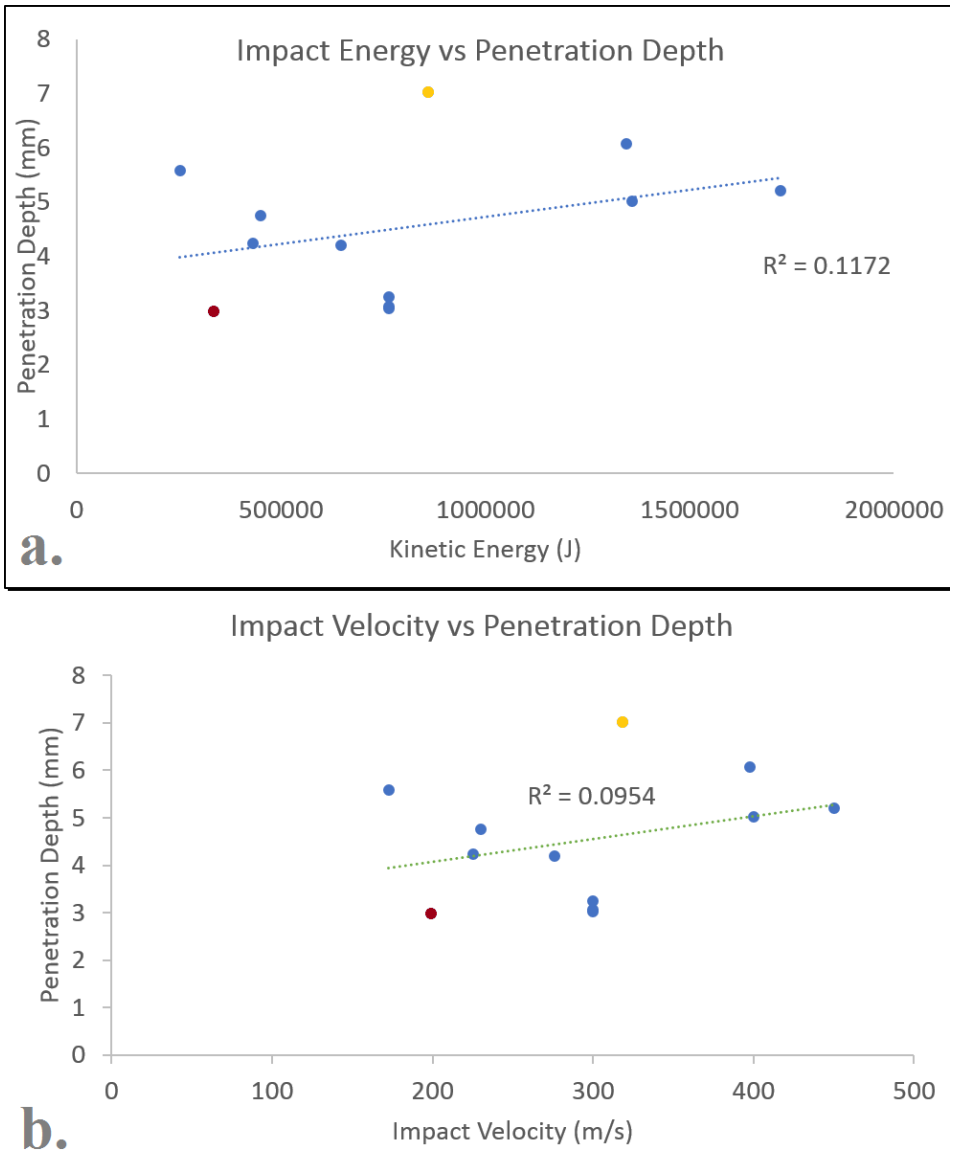

Figure 5.23: *Graphs of penetration depth versus the kinetic energy of the impacting projectile (left) and versus impact speed (right). Calculating the least-squares regression fit of the trendlines, kinetic energy had the better fit although neither was very strong.*

fact that the indent measured only μm instead of mm meant that far more data points could be taken in the region of interest.

Measuring the Vickers hardness (HV50 in this case) of the matrix material, taking care to avoid cracks, inclusions and fibres, at intervals of approximately 0.1 mm starting very close to the base of the impact crater and continuing parallel to the impact axis through the thickness of the disc found both hardening and softening. The area immediately adjacent to the impact site was softer than the matrix measured in a reference piece, that the hardness more than approximately 0.75 mm away was on the order of 20% higher than the reference material and that it decreased towards this reference value over around 10 mm.

Testing the hardness at sides more than 40 mm away from the impact site and comparing the results with those taken near the rear surface of the disc, they were sufficiently similar to each other an to measurements of a reference piece of material to say that the hardness had reached its bulk value at the end of the closely-measured region.

Comparative measurements of the hardness of the disc at the surface and in the sectioned thickness hardnesses found that the surface was approximately twice the hardness of the bulk. This is likely work hardening caused by the machining method used (a lathe). The cross-sectioning method used was a precision cutter run very slowly through the disc, which will have minimal surface hardening effects on the region of interest.

Figure 5.24 shows examples of the plotted trendlines of hardness versus distance, with an error on the trendline of the R-squared value of the line plotted above and below it. Individual points have an estimated measurement error of around 1% based on the uncertainty in Vernier calliper measurement of the diagonal lengths. The trendlines varied between 14.1 and 29.6 in gradient. They are correlated pretty well with impact speed but less well with penetration depth.

One of the MMC reference samples showed very strong work hardening and very low penetration distance (3 mm at about 200 m/s vs 5 mm under similar conditions for a fibre-only MMC). This is in line with the excellent hardness of MMC materials.

Points measured at 0.01 mm and 0.5 mm from the impact crater showed lower hardness than the

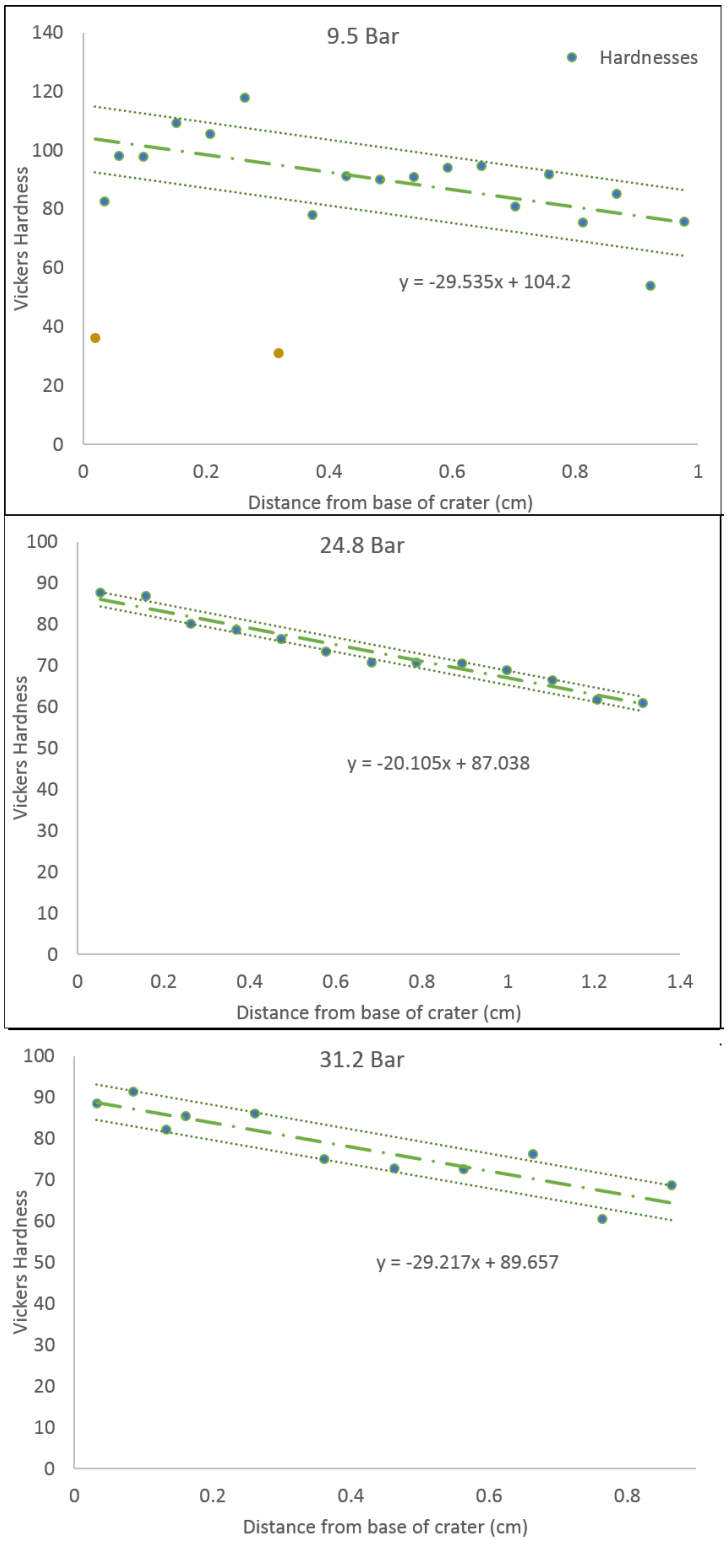

Figure 5.24: *Example graphs of Vickers hardness versus distance from the impact crater. To plot the trendline, in some cases outlying points were removed because they were either very close to the impact site, over a sub-surface pore or too close to a reinforcement fibre.*

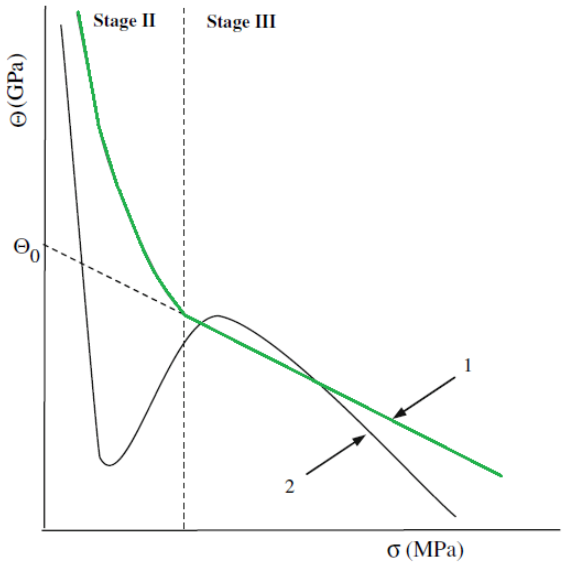

Figure 5.25: *Tiryakoglu et al [113] found that work hardening was proportional to applied stress, with two regions of hardening behaviour based on stress and two regimes based on ageing history. Curve 1 represents under-aged alloy. Θ represents the work hardening rate.*

bulk material, suggesting damage in the high-flow zone has reduced the effective hardness of the material. The size of the softened zone was higher for higher-pressure impacts.

Cast alloys such as A357 are confirmed to work-harden under deformation. Tyriakoglu et al [113] give a schematic illustration of strain hardening with applied stress in Al-Mg-Si alloys, shown in Figure 5.25. The two curves represent different regimes, accessed by the author by different ageing history. The data found in this work could be explained by the high-flow region having transitioned from type 1 hardening, representing under-aged aluminium, to type 2.

The fact that a different work hardening regime has been seen in the close vicinity of impact suggests the possibility of a shock-induced effect in the material.

Looking at the potential correlations between impact energy, impact velocity and penetration depth (Figure 5.26), the correlations with penetration depth and impact energy are equally good. This suggests that there is an underlying mechanism governing the energy imparted by impact, the depth to which the pellet became embedded and the degree of work hardening in the material.

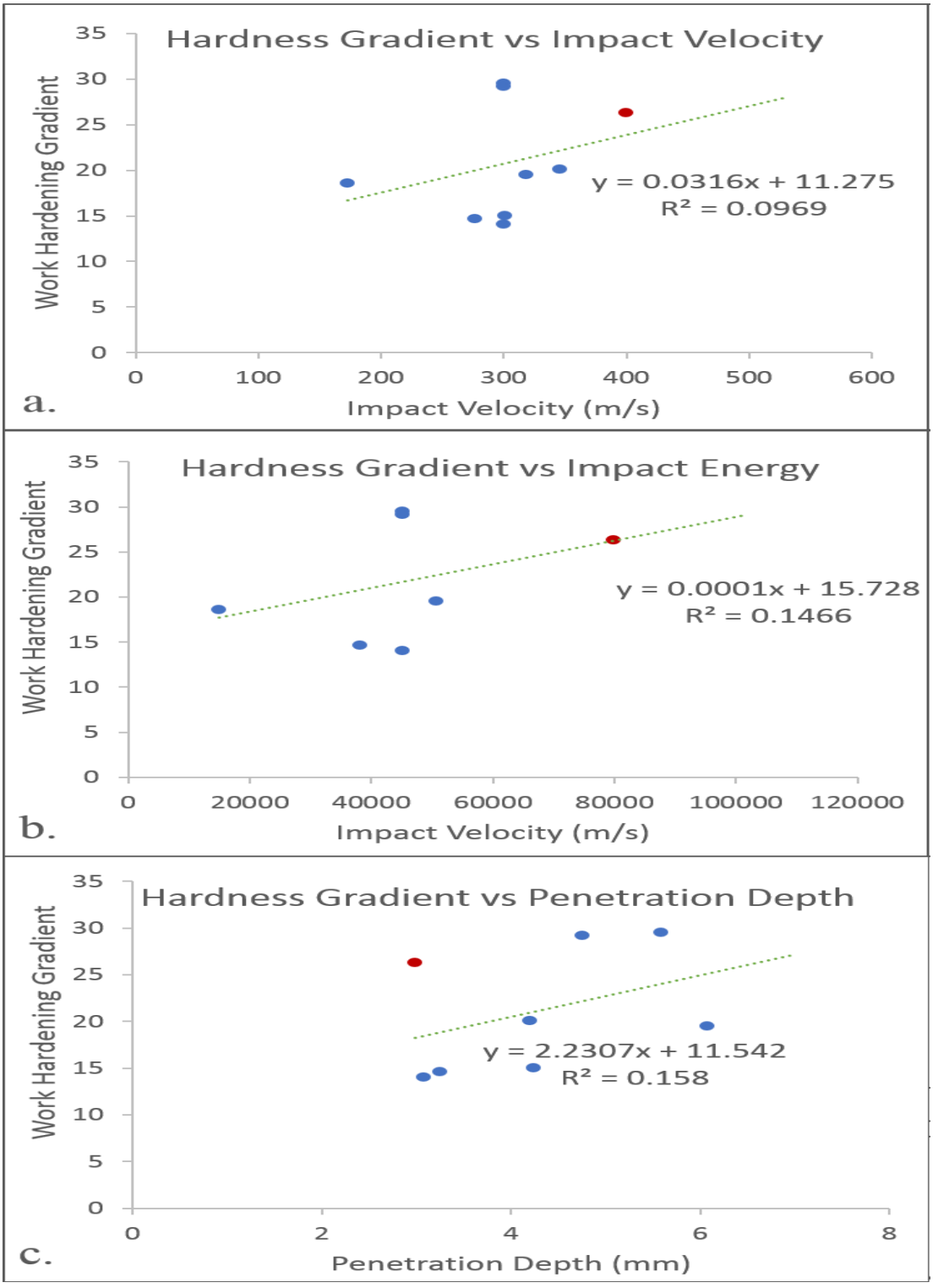

Figure 5.26: *Vickers hardness gradients versus impact velocity, impact kinetic energy and penetration depth. Impact energy and penetration depth are equally well correlated. The red point on these graphs marks an A357/15 %wt SiC-based MMC used as a reference material.*

Cast alloys such as A357 are confirmed to work-harden under deformation. Tyriakoglu et al [113] give a schematic illustration of strain hardening with applied stress in Al-Mg-Si alloys, shown in Figure 5.32. The two curves represent different regimes, accessed by the author by different ageing history. The data found in this work could be explained by the high-flow region having transitioned from type 1 hardening, representing under-aged aluminium, to type 2.

The fact that a different work hardening regime has been seen in the close vicinity of impact suggests the possibility of a shock-induced effect in the material.

Further, Peyre et al [110] found that shock-induced hardening in A356 was consistent at a distance of more than 350 μm from the shock site, rather than continuously decreasing as was found here. This is consistent with the earlier hypothesis that the mixed-impedance nature of the composite material will act as a shock-dissipating structure. These results agree with the conclusions of Olney et al [21] that a shock will not propagate well past changes in acoustic impedance.

Looking at the potential correlations between impact energy, impact velocity and penetration depth (Figure 5.26), the correlations with penetration depth and impact energy are equally good. This suggests that there is an underlying mechanism governing the energy imparted by impact, the depth to which the pellet became embedded and the degree of work hardening in the material.

5.4 Summary

This chapter discussed the SHPB system for the compression of composite material, which deforms material in the slower region of shock regime. Finite element simulations validated the choice of stepped loading to demonstrate strain response. the load dissipation of the composite was significantly better than the A357 results in the literature. There was evidence that the specimens were not fully compressed during the test.

Specimens were found to have deformed in shear, which is indicative of strain-dependent mechanisms. The results of the SHPB tests are presented as qualitative rather than quantitative.

The chapter also covered the gas gun system and the results of ballistic impact on MMCs and HMMCs. The penetration depth found in SiC-based MMCs and HMMCs comparable. Damage was found to have been very strongly localised. Projectiles were found to have rotated about their impact trajectory ("tumbled").

Very strong work-hardening was seen, which when coupled with the decrease of work hardening with increasing distance from impact site, suggests a shock forms and is dissipated. The surface of the shattered sample suggested brittle failure, consistent with shock behaviour.

The SHPB tests were found to give good qualitative agreement with the literature. They also provided an opportunity to examine the patterns of shear damage in a composite material and gave good support to the hypothesis that composites deform very differently under dynamic and static loads. Its stress-absorption compared favourably with OFHC (oxygen-free high-conductivity) copper, and its measured strength of the material was good, but it was thought not to have reached its maximum compressive load during the tests.

Under ballistic impact loading, the hybrid MMC offered very similar strength and damage resistance to a ceramic MMC, with a safer and much lower-cost manufacturing route available. The HMMC and MMC both also showed evidence that it caused projectiles to rotate after impact, which dramatically reduces their maximum penetration depth.

Suggested further work in this area includes using bullet-shaped projectile impact tests to verify the tumbling behaviour; using more energetic plate-impact tests on larger composite plates to study the damage threshold of the material and to further examine its shock-dissipative properties; and using electron back-scatter diffraction (EBSD) microscopy to look for any shock-induced phase transformations in the material.

Chapter 6

Conclusions

The extant literature about metal matrix composites, both ceramic- and metal-reinforced, is primarily focused on improving on manufacturing techniques. For all MMCs, the primary challenge in developing a manufacturing technique is the infiltration of matrix into the reinforcement, owing to the high surface tension of aluminium and its alloys.

In fibre-reinforced composites, most methods attempted to force infiltration by imposing external pressure, either by isostatic pressing or by squeeze casting. These methods are expensive, difficult to use at large scales and require specialist preparations, either sintered preforms for squeeze casting or carefully-milled powders for an isostatic press.

This work attempted to develop a less expensive manufacturing route, first by using an open-air casting method which would have strongly minimised costs but which was ultimately unsuccessful, and then successfully by using the motive force imparted by the electric field of an induction furnace to force infiltration into the fibres.

This method was ultimately successful, producing a composite of A357 matrix and 10% wt Dramix 3D 80/30 SL fibres. Microstructural analysis was used to evaluate the success of this method and to determine the optimum casting parameters.

It was determined that the minimum time required to ensure full A357 infiltration by raising its temperature well above its freezing range, approximately 120 seconds, was greater than the min-

imum time required to force infiltration by the A357. Longer exposure began to melt the steel fibres, which would tend to be heated more quickly than the matrix because of their greater electrical resistivity.

The fibres were introduced to liquid A357 at 700°C and the composite was brought to a measured temperature of 650°C before being removed from the furnace and cooled. Volume fractions above 10% were found to contain very substantial voids, and fibres were found to have settled when 5% wt was tested, creating regions of higher reinforcement concentration and regions of unreinforced A357.

Further work would be useful in scaling these methods to larger casting volumes and evaluating more precisely the optimum parameters for composite manufacture.

The other area of significant focus in recent literature on MMCs has been on modelling. New imaging techniques such as X-ray CT scanning have permitted the use of actual internal fibre structures in analytical models, and the increases in computing power in the last two decades have permitted much more complex models of mechanical behaviour to be applied. However, while many of these models have reached good agreement with specific tests, none has yet emerged as a clear and satisfactory standard.

Comparatively little work has been done on mechanical characterisation of composite behaviour, other than quasi-static tensile tests used to evaluate manufacturing parameters or determine the suitability of a specific material for a particular use, such as automotive components [36].

This is perhaps because of the increased difficulty in performing even basic tests on a composite material. To be representative of the bulk properties of a material, a test specimen must contain a large number of the "cells" which compose it. In a metal, this is a crystal and the test specimen must be much larger than the gain size. In a composite, the "cell" must contain more than one reinforcement piece, rendering it and its test specimens much larger. This means that specialist, high-force testing machines must be used. Composites are also more difficult to machine, making some test pieces difficult to produce.

These challenges were very apparent during the tensile and compressive tests performed during

this work. An important area of further study would be to attempt these tests again using large test specimens and induction-manufactured composites.

The composite did perform better than A357 produced under the same conditions but not as well as T6 tempered A357. Age hardened composite specimens performed slightly less well than as-cast specimens, thought to be because of the detrimental interface growth found above 400°C.

The 3-point bending tests and some of the tensile tests showed measurable post-failure strength. Some investigation of the limits of this phenomenon, such as the circumstances under which it becomes active and the maximum strength which can be achieved, is merited here.

The dynamic properties of the composite material were very good. It showed high strength and damage resistance under SHPB loading, with strains of 20% supported without catastrophic damage having been sustained. Under ballistic testing, it performed comparably with a SiC-based MMC in terms of resistance to projectile penetration.

Its shock- and pressure-dissipation properties, attributed to the difference in acoustic impedance between the matrix and the reinforcement, were seen in both SHPB tests and after projectile impact in the gas gun. Valuable work could be done in re-testing the material with a larger SHPB system, by evaluating ballistic resistance with sharp-tipped projectiles and by doing a series of plate-impact tests with the more massive projectile to determine the threshold for catastrophic damage under shock loads. It is hoped that this characterisation work might be a useful contribution to the literature.

This project has successfully demonstrated that it is possible to manufacture a composite material with promising load-dissipating and ballistic resistance properties using an induction furnace, and demonstrated a novel technique for measuring the damage response of a specimen by mapped micro-hardness measurements.

Acknowledgments

Academically, I must extend thanks to Imperial College's Institute of Shock Physics, to Gareth Tear and to Trevor Stickland of Civil Engineering for use of their equipment and time; to BCAST's technical team for their vast patience with my peculiar requests; and to Dstl and DGA for funding the project.

Personally, I would like to acknowledge and thank my supervisor, Hari Nadendla, for keeping with me through the challenges I've faced; my MSc supervisor Bill Proud for continuing to help a former student far above the requirements of 'networking'; both of my parents for their support; and of course my husband John, without whose unfailing love and great patience none of this would have been possible.

Bibliography

[1] Materion. *SupremEx*. Datasheet, Issued 2012.

[2] I A Ibrahim, F A Mohamed, and E J Lavernia. "Particulate Reinforced Metal Matrix Composites – a Review". In: *Journal of Materials Science* 26 (1991), pp. 1137–1156.

[3] T W Clyne and P J Withers. *An Introduction to Metal Matrix Composites*. Cambridge University Press, 1993.

[4] F Delannay, L Froyen, and A Deruyttere. "Review: The Wetting of Solids by Molten Metals and its Relation to the Preparation of Metal-Matrix Composites". In: *Journal of Materials Science* 22 (1987), pp. 1–16.

[5] Y Sahin and G Sur. "The Effect of Al2O3, TiN and Ti (C,N) Based CVD Coatings on Tool Wear in Machining Metal Matrix Composites". In: *Surface and Coatings Technology* 179 (2004), pp. 349–355.

[6] A Pattnaik and A Lawley. "Effect of Elevated Temperature Exposure on the Structure, Stability, and Mechanical Behaviour of Aluminium-Stainless Steel Composites". In: *Metallurgical and Materials Transactions* 5 (1 1974), pp. 111–122.

[7] D Mandal, B K Dutta, and S C Panigrahi. "Wear and Friction Behavior of Stir Cast Aluminium-Base Short Steel Fiber Reinforced Composites". In: *Wear* 257 (2004), pp. 654–664.

[8] M F Ashby and D R H Jones. *Engineering Materials 2*. Third. Elsevier Butterworth-Heinemann, 2006.

[9] M Aghajanian et al. “Processing of Hybrid Structures Consisting of Al-Based Metal Matrix Composites (MMCs) with Metallic Reinforcement of Steel or Titanium”. In: *TMS 2013 Annual Meeting Supplemental Proceedings* (2013).

[10] S R Pemberton et al. “The Fracture Energy of Metal Fibre Reinforced Ceramic Composites (MFCs)”. In: *Composites Science and Technology* 71 (2011), pp. 266–275.

[11] M Guden and I W Hall. “High Strain-Rate Compression Testing of a Short-Fiber Reinforced Aluminum Composite”. In: *Materials Science and Engineering: A* 232 (1-2 1997), pp. 1–10.

[12] G-Z Quan et al. “A characterization for the flow behavior of as-extruded 7075 aluminum alloy by the improved Arrhenius model with variable parameters”. In: *Materials Research* 16 (Feb. 2013), pp. 19–27.

[13] N Banthia and J-F Trottier. “Deformed Steel Fiber–Cementitious Matrix Bond Under Impact”. In: *Cement and Concrere Research* 21 (1991), pp. 158–168.

[14] Y Sahin. “The Prediction of Wear Resistance Model for the Metal Matrix Composites”. In: *Wear* 258 (2005), pp. 1717–1722.

[15] K Umanatha, K Palanikumar, and S T Selvamanid. “Analysis of dry sliding wear behaviour of Al6061/SiC/Al2O3 hybrid metal matrix composites”. In: *Composites Part B: Engineering* 53 (2013), pp. 159–168.

[16] ASM Handbook Online. *Properties and Selection: Nonferrous Alloys and Special-Purpose Materials*. Vol. 3. 2003.

[17] C S Dunleavy, J A Curran, and T W Clyne. “Plasma Electrolytic Oxidation of Aluminium Networks to Form a Metal-Cored Ceramic Composite Hybrid Material”. In: *Composites Science and Technology* 71 (2011), pp. 908–915.

[18] W Hufenbach et al. “Manufacture Studies and Impact Behaviour of Light Metal Matrix Composites Reinforced by Steel Wires”. In: *Archives of Civil and Mechanical Engineering* 12 (2012), pp. 265–272.

[19] X Yang. *Particle Dispersion in Aluminium and Magnesium Alloys*. PhD Thesis, Brunel University London, 2016.

[20] A Kalkanli and S Ylmaz. “Synthesis and Characterization of Aluminum Alloy 7075 Reinforced with Silicon Carbide Particulates”. In: *Materials and Design* 29 (2008), pp. 775–780.

[21] K L Olney et al. “Role of Material Properties and Mesostructure on Dynamic Deformation and Shear Instability in Al-W Granular Composites”. In: *Journal of applied Physics* 110 (114908 2011).

[22] *Silicon Carbide quotation page*. https://tinyurl.com/y7p2p8og. Accessed: 2018-April-16.

[23] Washington Mills. *Materials Safety Data Sheet: Silicon Carbide powder*. Chemtel Inc., 2015.

[24] NHS UK. *Silicosis - NHS UK*. Accessed 7 August 2018.

[25] T J A Doel, M H Loretto, and P Bowen. “Mechanical Properties of Aluminium-Based Particulate Metal-Matrix Composites”. In: *Composites* 24 (3 1993), pp. 270–275.

[26] M F Ashby and D R H Jones. *Engineering Materials 1*. Third. Elsevier Butterworth-Heinemann, 2005.

[27] Z Zhang and D L Chen. “Consideration of Orowan Strengthening Effect in Particulate-Reinforced Metal Matrix Nanocomposites: A Model for Predicting their Yield Strength”. In: *Scripta Materialia* 54 (2006), pp. 1321–1326.

[28] K Wilson, E V Barrera, and Y Bayazitiglu. “Processing of Titanium Single-Walled Carbon Nanotube Metal-Matrix Composites by the Induction Melting Method”. In: *Journal of Composite Materials* 44 (9 2010), pp. 1037–1048.

[29] B L Dasari et al. “Mechanical properties of graphene oxide reinforced aluminium matrix composites”. In: *Composites Part B-Engineering* 145 (2018), pp. 136–144. DOI: 10.1016/j.compositesb.2018.03.022.

[30] J Jose et al. “Manufacture and characterization of a novel agro-waste based low cost metal matrix composite (MMC) by compocasting”. In: *Mateialsl Research Express* 5 (6 2018). DOI: 10.1088/2053-1591/aac803.

[31] K L Olney. “The Mechanisms of Plastic Strain Accommodation and Post Critical Behavior of Heterogeneous Reactive Composites Subject to Dynamic Loading (Doctoral thesis)”. In: *Retrieved from Electronic Theses and Dissertations library UC San Diego* (2014).

[32] S J S Chelladurai et al. “Effect of Copper Coating and Reinforcement Orientation on Mechanical Properties of LM6 Aluminium Alloy Composites Reinforced with Steel Mesh by Squeeze Casting”. In: *Transactions of the Indian Institiute of Metals* 71 (5 MAY 2018), pp. 1041–1048. DOI: 10.1007/s12666-017-1235-2.

[33] SJS Chelladurai and R Arthanari. “Effect of stir cast process parameters on wear behaviour of copper coated short steel fibers reinforced LM13 aluminium alloy composites”. In: *Materials Research Express* 5 (6 2018). DOI: 10.1088/2053-1591/aacd38.

[34] M R Ghomashchi and A Vikhrov. “Squeeze casting: an overview”. In: *Journal of Materials Processing Technology* 101 (1-3 2000), pp. 1–9.

[35] C Colin et al. “Stainless Steel Fibre Reinforced Aluminium Matrix Composites Processed by Squeeze Casting: Relationship Between Processing Conditions and Interfacial Microstructure”. In: *Journal de Physique IV* 3 (1993).

[36] S Kenningley, S J Barnes, and P J Withers. “Thermal Property Characterisation for a Steel Fibre Reinforced Aluminium Metal Matrix Composite (AlMMC)”. In: *TMS 2013 Annual Meeting Supplemental Proceedings* (2013).

[37] M Mizumoto, T Ohgai, and Akio Kagawa. “Characterization of Fiber-Reinforced Metal Matrix Composites Fabricated by Low-Pressure Infiltration Process”. In: *Materials Science and Engineering A* (2005), pp. 521–526.

[38] F Boland et al. “Tensile Flow Properties of Al-Based Matrix Composites Reinforced With a Random Planar Network of Continuous Metallic Fibres”. In: *Acta Materialia* 46.18 (1998), pp. 6311–6323.

[39] Y-H Hwang et al. “Interface Study for Stainless Steel Fibre-Reinforced Aluminium Matrix Composite”. In: *Journal of Materials Science* 32 (1997), pp. 719–725.

[40] R B Bhagat. “The Effects of Hot Pressing Parameters on the Strength of Aluminum/Stainless Steel Composites”. In: *Metallurgical and Materials Transactions* 16A (1985), p. 623.

[41] B C Pai et al. “Interface Stability in Vacuum Infiltrated Stainless Steel and Nichrome Reinfrced Aluminium Composites”. In: *Journal of Materials Science Letters* 2 (1983), p. 553.

[42] P-H Chiu et al. “Mechanisms of Fragmentation and Microstructure of Debris Generated During Explosive Testing of AL-W GranularComposite Rings”. In: *Journal of Physics: Conferense Series* 500 (112017 2014).

[43] A Mendes et al. “Role of shear in interface formation of aluminium-steel multilayered composite sheets”. In: *Materials Science and Engineering A - Structural Materials Properties Microstructure and Processing* 705 (2017), pp. 142–152. DOI: 10.1016/j.msea.2017.08.025.

[44] N-R Park et al. “Simultaneous Synthesis and Consolidation of a Nanostructured 4Fe-Al2O3 Composite from Mechanically Activated Powders by High Frequency Induction Heated Sintering”. In: *Journal of Ceramic Processing Research* 10 (6 2009), pp. 774–779.

[45] Ch Vives et al. “Fabrication of Metal Matrix Composites using a Helical Induction Stirrer”. In: *Materials Science and Engineering A* 173 (1993), pp. 239–242.

[46] C C Degnan and P H Shipway. “A Comparison of the Reciprocating Sliding Wear Behaviour of Steel Based Metal Matrix Composites Processed from Self-Propagating High-Temperature Synthesised Fe-TiC and Fe-TiB2 Masteralloys”. In: *Wear* 252 (2002), pp. 832–841.

[47] T Z Kattamis and T Suganuma. “Solidification Processing and Tribological Behavior of Particulate TiC-Ferrous Matrix Composites”. In: *Materials Science and Engineering A* 128 (1990), pp. 241–252.

[48] Y P Jeon and C G Kang. “Reheating Process for Thixoforging of Metal Matrix Composites Fabricated by Induction Heating and the Mechanical Stirring Process”. In: *Proceedings of The Institution of Mechanical Engineers Part B-journal of Engineering Manufacture* 217 (), pp. 1383–1391.

[49] R A Varin. “Intermetallic-Reinforced Light-Metal Matrix In-Situ Composites”. In: *Metallurgical and Materials Transactions A* 33A (2002), pp. 193–201.

[50] Y H Song et al. “Effect of Foaming Temperature on Pore Morphology of Al/AlN Composite Foam Fabricated by Melt Foaming Method”. In: *Materials Science Forum* 658 (2010), pp. 198–192.

[51] E Linul, L Marsavina, and J Kovacik. “Collapse mechanisms of metal foam matrix composites under static and dynamic loading conditions”. In: *Materials Science and Engineering A - Structural Materials Properties Microstructure and Processing* 690 (2017), pp. 214–224. DOI: 10.1016/j.msea.2017.03.009.

[52] E Ghasali et al. “Ultra-low temperature fabrication of vanadium carbide reinforced aluminum nano composite through spark plasma sintering”. In: *Journal of Alloys and Compounds* 753 (2018), pp. 433–445. DOI: 10.1016/j.jallcom.2018.04.239.

[53] C Perron, C Arvieu, and E Lacoste. “Evaluation of an original use of spark plasma sintering to laminate carbon fibres reinforced aluminium”. In: *Journal of Composite Materials* 52 (16 2018), pp. 2149–2161. DOI: 10.1177/0021998317740944.

[54] M Dong et al. “Prediction of the Mechanical Behaviour of Short Fiber Reinforced MMCs by Combined Cell Models”. In: *Computational Materials Science* 9 (1997), pp. 121–133.

[55] A F Whitehouse and T W Clyne. “Effects of Reinforcement Content and Shape on Cavitation and Failure in Metal-Matrix Composites”. In: *Composites* 24 (3 1993), pp. 256–261.

[56] S Hwang and M Todo. “Characterization of Compressive Deformation Behavior of Multi-Layer Porous Composite Materials for Articular Tissue Engineering”. In: *Journal of Medical Science and Technology* 26 (7 2012), pp. 1999–2004.

[57] S Yadav, D R Chichili, and K T Ramesh. “The Mechanical Response of a 6061-T6 Al/Al2O3 Metal-Matrix Composite at High Rate of Deformation”. In: *Acta Metallurgica et Materialia* 43 (12 1995), pp. 4453–4464.

[58] D Pavlyuchkov et al. “Al-Cr-Fe phase diagram Isothermal Sections in the region above 50 at% Al”. In: *CALPHAD: Computer Coupling of Phase Diagrams and Thermochemistry* 45 (2014), pp. 194–203.

[59] S K Mannan, V Seetharaman, and V S Raghunathan. In: *Materials Science and Engineering* 60 (1983), p. 79.

[60] I G Zhigun, V A Polyakov, and V V Mikhailov. "Compression Testing of Composites". In: *Mechanics of Composite Materials* 15 (6 1979), pp. 775–781.

[61] Y Q Zhao et al. "In Situ Production of Locally Reinforced Steel-based Composites with TiC Particulates Using High-Frequency Induction Process". In: *ISIJ International* 46 (4 2006), pp. 617–619.

[62] Y H Son and J E Morral. "The Effect of composition on Marker Movement and Kirkendall porosity in Ternary Alloys". In: *Metallurgical Transactions A - Physical Metallurgy and Materials Science* 20 (11 1989), pp. 2299–2303.

[63] J-P Won et al. "Bonding Properties of Amorphous Micro-Steel Fibre-Reinforced cementitious Composites". In: *Composite Structures* 102 (2013), pp. 101–109.

[64] H Lee et al. "Dynamic compressive deformation behavior of SiC-particulate-reinforced A356 Al alloy matrix composites fabricated by liquid pressing process". In: *Materials Science and Engineering A-Structural Materials Properties Microstructure and Processing* 680 (2017), pp. 368–377. DOI: 10.1016/j.msea.2016.10.102.

[65] H Leeand J H Choi M C Jo et al. "Effects of Strain Rate on Compressive Properties in Bimodal 7075 Al-SiCp Composite". In: *Metals and Materials International* 24 (4 2017), pp. 894–903. DOI: 10.1007/s12540-018-0092-9.

[66] N Behm et al. "Quasi-static and high-rate mechanical behavior of aluminum-based MMC reinforced with boron carbide of various length scales". In: *Materials Science and Engineering A - Structural Materials Properties Microstructure and Processing* 650 (2016), pp. 305–316. DOI: 10.1016/j.msea.2015.10.064.

[67] H Lee et al. "Dynamic compressive deformation behavior of SiC-particulate-reinforced A356 Al alloy matrix composites fabricated by liquid pressing process". In: *Materials Science and Engineering A* 680 (2017), pp. 368–377.

[68] H Lee et al. "Effects of Strain Rate on Compressive Properties in Bimodal 7075 Al-SiCp Composite". In: *Metals and Materials International* 24 (2018), pp. 894–903.

[69] V Pare, S Modi, and K N Jonnalagadda. “Thermo-mechanical behavior and bulk texture studies on AA5052-H32 under dynamic compression”. In: *Materials Science and Engineering A - Structural Materials Properties Microstructure and Processing* 668 (2016), pp. 38–49. DOI: 10.1016/j.msea.2016.05.019.

[70] H Kolsky. “An Investigation of the Mechanical Properties of Materials at Very High Rates of Loading”. In: *Proc. Royal Soc, Lond. B* 62 (1949), pp. 676–700.

[71] D J Frew, M J Forrestal and W Chen. “Pulse Shaping Techniques for Testing Brittle Materials with a Split Hopkinson Pressure Bar”. In: *Journal of Experimental Mechanics* 42 (1 2002).

[72] B Song, Y Ge, W W Chen and T Weerasooriya. “Radial Inertia Effects in Kolsky Bar Testing of Extra-soft Specimens”. In: *Journal of Experimental Mechanics* 47 (2007), 659670.

[73] D R Drodge, D M Williamson and W G Proud. “Split Hopkinson Pressure Bar Techniques for the Estimation of a High Strain-rate Elastic Modulus”. In: Society for Experimental Mechanics Inc., 2008.

[74] B Song and W Chen. “Dynamic Stress Equilibration in Split Hopkinson Pressure Bar Tests on Soft Materials”. In: *Journal of Experimental Mechanics* 44 (3 2004).

[75] D M Williamson, D R Drodge and W G Proud. “Two step loading of ABS polymer in a SHPB”. In: *Proceedings of the XIth International Congress and Exposition*. Orlando, Florida USA, 2008.

[76] J M Lefebvre and B Escaig. “Plastic Deformation of Glassy Amorphous Polymers: Influence of Strain Rate”. In: *Journal of Materials Science* (1985), pp. 438–448.

[77] N N Dioh, P S Leevers and J G Williams. “Thickness Effects in Split Hopkinson Pressure Bar Tests”. In: *Polymer* 34 (20 1993).

[78] E D H Davies and S C Hunter. “The Dynamic Compression Testing of the Solids by the Method of the Split Hopkinson Bar.” In: *Jounal of Mechanical and Physical Solids* 11 (3 1963), 155179.

[79] S M Walley and J E Field. “Strain Rate Sensitivity of Polymers in Compression from Low to High Strain Rates”. In: *DYMAT Journal* (1994), pp. 21–227.

[80] R A Davenport. *Stepped Loading in the Split-Hopkinson Pressure Bar (MSc Dissertation)*. Imperial College London, 2013.

[81] W D Callister and D G Rethwisch. *Fundamentals of Materials Science and Engineering*. 4th ed. Wiley, 2013.

[82] A Atmaca et al. "Elasto-Plastic Stress Analysis of Steel Fibre Reinforced Aluminum Metal Matrix Composite Plates". In: *2nd International Conference Manufacturing Engineering and Management* (2012), pp. 49–52.

[83] D Tsarouchas and A E Markaki. "Extraction of Fibre Network Architecture by X-ray Tomography and Prediction of Elastic Properties using an Affine Model". In: *Acta Materialia* 59 (2011), pp. 6989–7002.

[84] L Zhou et al. "Constitutive equation and model validation for a 31 vol.% B4Cp/6061Al composite during hot compression". In: *Journal of Materials Science and Technology* 34 (10 2018), pp. 1730–1738. DOI: 10.1016/j.jmst.2018.02.001.

[85] J P Borg et al. "Computational simulations of the dynamic compaction of porous media". In: *International Journal of Impact Engineering* 33 (1-12 2006), pp. 109–118.

[86] K S Mahon and T W Lee. "Compaction of Granular HMX: P-alpha Porosity model in CTH Hydrocode". In: *AIP Advances* 5 (12 2015). DOI: 10.1063/1.4938524.

[87] J Zhou et al. "The energy-absorbing behaviour of foam cores reinforced with composite rods". In: *Composite Structures* 116 (2014), pp. 346–35.

[88] E G Van Putten et al. "Scattering Lens Resolves Sub-100 nm Structures with Visible Light". In: *Physical Review Letters* 106 (2011), pp. 1–4. DOI: 193905.

[89] C E Hall. *Introduction to Electron Microscopy*. 2nd ed. McGraw-Hill, 1966.

[90] W A Kalender. "Technical foundations of spiral CT". In: *Seminars in Ultrasound, CT and MRI* 15 (), pp. 81–89.

[91] J Schindelin et al. "FIJI: an open-source platform for biological-image analysis". In: *Nature Methods* (2012).

[92] C T Rueden et al. "ImageJ2: ImageJ for the next generation of scientific image data". In: *BMC Bioinformatics* 18 (2017).

[93] R W Thomas. “An Introduction To Quadrat Analysis”. In: *Concepts and Techniques in Modern Geography* (1977).

[94] Aluminium Association. *Workshop on Aluminium Alloys*. Presented Materials, 2010.

[95] British Standards Institution. *BS EN 485-2: Aluminium and Aluminium Alloys – Sheets, Strips and Plates Part 2: Mechanical Properties*. BSI, 2003.

[96] ASM Handbook Online. *Alloy Phase Diagrams*. Vol. 3. 2003.

[97] Q F Li, D G McCartney, and N L Loh. “Measurements on Fibre Distribution in a Fibre-Reinforced A1 Metal-Matrix Composite (MMC) (Matrix Intercept-Length Measurements)”. In: *Journal of Materials Processing Technology* 51 (1995), pp. 244–254.

[98] S G Shabestari. “The Effect of Iron and Manganese on the Formation of Intermetallic Compounds in Aluminum-Silicon Alloys”. In: *Materials Science and Engineering A* 383 (2004), pp. 289–298.

[99] J A Taylor. “The effect of iron in Al-Si casting alloys”. In: *35th Australian Foundry Institute National Conference*. 2004.

[100] ASTM Standard E-399. *Standard Test Method for Plane-strain Frature Toughness of Metallic Materials*. 90th ed. www.astm.org. West Conshohocken, PA: ASTM International, 1997. ISBN: 10.1520/E0399-90R97.

[101] R L Smith and G E Sandland. “An Accurate Method of Determining the Hardness of Metals, with Particular Reference to Those of a High Degree of Hardness”. In: *Proceedings of the Institution of Mechanical Engineers* 1 (1922), pp. 623–641.

[102] International Organization for Standardization. *ISO 6361-2: Wrought Aluminium and Aluminium Alloys – Sheets, Strips and Plates – Part 2: Mechanical Properties*. ISO, 2014.

[103] J W Christian and S Mahajan. “Deformation Twinning”. In: *Progress in Materials Science* 39 (1995), pp. 1–157.

[104] S P Timothy. “The Structure of Adiabatic Shear Bands in Metals: A Critical Review”. In: *Acta Materialia* 35 (2 1987), pp. 301–306.

[105] D Francis et al. “Split Hopkinson Pressure Bar Graphical Analysis Tool”. In: *Experimental Mechanics* 57 (2017), pp. 179–183.

[106] M-C Cai et al. “A Constitutive Description of the Strain Rate and Temperature Effects on the Mechanical Behavior of Materials”. In: *Mechanics of Materials* 42 (2010), 774781.

[107] S Gupta, S Abotula, and A Shulka. “Determination of Johnson-Cook Parameters for Cast Aluminum Alloys”. In: *Journal of Engineering Materials and Technology* 136 (2014), pp. 1–4.

[108] A A Cenna et al. “Single Particle Impact Tests Using Gas Gun and Analysis of High Strain-Rate Impact Events in Ductile Materials”. In: *Wear* 271 (2011), pp. 1497–1503.

[109] B M French. *Traces of Catastrophe: A Handbook of Shock-Metamorphic Effects in Terrestrial Meteorite Impact Structures*. LPI Contribution No. 954. Lunar and Planetary Institute, Houston, 1998.

[110] P Peyre, R Fabbro andP Merrien, and H P Lieurade. “Laser shock processing of aluminium alloys. Application to high cycle fatigue behaviour”. In: *Materials Science and Engineering* A210 (1996), pp. 102–113.

[111] R S Mishra, T R Bieler, and A K Mukherjee. “Mechanism of High Strain Rate Superplasticity in Aluminium Alloy Composites”. In: *Acta Metallurgica* 45 (2 1997), pp. 561–568.

[112] T A Ota. “Numerical study of the effect of normalised window size, sampling frequency, and noise level on short time fourier transform analysis”. In: *Review of Scientific Instruments* 84 (2013).

[113] M Tiryakioglu and N D Alexopolous. “The Effect of Artificial Aging on Tensile Work Hardening Characteristics of a Cast Al-7 Pct Si-0.55 Pct Mg (A357) Alloy”. In: *Metallurgical and Materials Transactions A* 39 (2008), pp. 2772–2780. DOI: 10.1007/s11661-008-9611-5.